Propagation in the Galactic magnetic field

Effects on the spectrum, composition and anisotropy of Galactic and extragalactic cosmic rays

Alex Kääpä

A thesis presented for the degree of
Doktor rer. nat.

BERGISCHE
UNIVERSITÄT
WUPPERTAL

Astroparticle Group
Bergische Universität Wuppertal
Germany

The PhD thesis can be quoted as follows:

urn:nbn:de:hbz:468-20220524-110325-8
[http://nbn-resolving.de/urn/resolver.pl?urn=urn%3Anbn%3Ade%3Ahbz%3A468-20220524-110325-8]

DOI: 10.25926/gyd2-em83
[https://doi.org/10.25926/gyd2-em83]

Propagation in the Galactic magnetic field

Effects on the spectrum, composition and anisotropy Galactic and extragalactic cosmic rays

Alex Kääpä

Abstract

This dissertation treats the propagation effects that the Galactic magnetic field imposes on cosmic rays in the rigidity range matching the transition region from Galactic to extragalactic cosmic rays. Two main topics are covered. The first topic deals with the relation of these propagation effects with the structure of the Galactic magnetic field. The rigidity range matching the transition region also signifies a change in propagation regimes from diffusive to ballistic. We show that changes in the rigidity dependence of key parameters occur at rigidities, where the corresponding gyro radius matches typical length scales of the Galaxy for typical magnetic field strengths. We further lay out how the changes in propagation regimes lead to important rigidity-dependent effects in the trajectories of both Galactic and extragalactic cosmic rays. At the lowest rigidities, Galactic cosmic rays propagate diffusively in the Galactic plane leading to a confinement therein. As rigidity increases, confinement decreases and particles more readily leak out of the Galaxy. Extragalactic cosmic rays at the lowest rigidities are partly shielded by the strong magnetic fields in the Galactic plane region, while those that manage to penetrate into the Galactic plane are confined therein. Both of these effects weaken as rigidity increases.

In the second topic, the modifications that these propagation effects impose on cosmic ray observables are explored. Galactic cosmic rays experience a flux suppression towards higher rigidities due to their decreased confinement (or increased leakage), which naturally also leads to a modification of the composition towards a heavier mean mass. The shielding and confinement of extragalactic cosmic rays counteract exactly, such that the Galactic magnetic field does not create any flux modifications or anisotropies if they are injected isotropically into the Galaxy. In the case of anisotropic injection, extragalactic cosmic rays are strongly isotropised when propagating through the Galactic magnetic field. Anisotropies above the %-level only survive above $\sim 1\,\mathrm{EV}$ in the form of a dipole. However, due to the shift in rigidity of the regions in the sky of highest magnetic transparency, flux modifications can arise, the nature of which depends on the nature of the anisotropy. Injected dipoles lead to more subtle changes in the spectrum in the form of a change in slope, whereas injected point sources can give rise to spectral breaks. These results are finally contextualised in form of their implications on the transition region.

Dedication

To the voiceless. You, too, will be heard.

Declaration of Authorship

English

I hereby declare that the thesis submitted is my own unaided work. All direct or indirect sources used are acknowledged as references.

This thesis was not previously presented to another examination board and has not been published.

Deutsch

Hiermit versichere ich, die vorliegende Arbeit selbstständig und unter ausschließlicher Verwendung der angegebenen Literatur und Hilfsmittel erstellt zu haben.

Die Arbeit wurde bisher in gleicher oder ähnlicher Form keiner anderen Prüfungsbehörde vorgelegt und auch nicht veröffentlicht.

Wuppertal, den _____ _____

(Alex Kääpä)

Acknowledgements

This work is the culmination of more than eight years of research and eleven years of study. There are many people and faces that have come and gone, some have been constant companions throughout this time, most have become friends, and all have shaped the physicist and colleague I am now. Therefore, my upmost gratitude goes to the entirety of the astroparticle group in Wuppertal. Special mentions go to Sven Querchfeld, who mentored me for my Bachelor's thesis and with whom I have shared an office the longest, AOR Dr. Julian Rautenberg, who has guided my physics intuitions most consistently throughout the years, Dr. Eric Mayotte, who has given invaluable input for the research carried out in the context of this thesis, and of course Prof. Karl-Heinz Kampert, who has been the referee for all of my theses and closest thing to a mentor.

I also want to thank my former classmates who first embarked upon this journey with me and are still in my life to this day. They include Mirjam Schöneck, whose steadfastness has always impressed me, Gunnar Jäkel, whose simple grasp of concepts were a big help for my studies, Stepan Nassyr, who accompanied me throughout various long evenings and nights as a lab partner, and Jörg Förtsch, with whom I shared countless conversations and darts sessions as a colleague that were a welcome distraction from the regular work routine.

Outside of my professional life, my friends and family have been an unequalled source of motivation. Particularly my parents, Pia and Olli, my brother, Niko, my decades-old friend Dennis have been irreplaceable pillars of support, reliable sanity checkers, and indispensible leisure providers in my life. I owe to you so much.

Finally, I want to thank Lisa, my companion, my guide, my anchor, my source of inspiration and awe, my baggage drop-off, my love.

Contents

List of Figures

Chapter 1

Introduction

The field of cosmic ray (CR) physics has come a long way since its inception just over 100 years ago. CRs have been measured across a wide energy range, revealing intriguing features in their flux, composition and arrival direction. They have even become useful for constraining various models at highest energies, or probing the validity of fundamental principles in physics. However, given the field's relative youth, many open questions remain about the processes that accelerate particles to the vast energies measured, and the details of their propagation through the cosmos.

One area where these open questions manifest is in the identification of the energy range of, as well as the processes involved in, the transition from CRs of Galactic origin, or Galactic CRs (GCRs) to those of extragalactic origin, or extragalactic CRs (EGCRs). This is appropriately illustrated in a key observable in CR physics, the all-particle energy spectrum. It spans more than 12 orders of magnitude in energy (MeV to several hundred EeV), and 34 orders of magnitude in flux. Above GeV energies, it follows a broken power-law relation with several key features. The resemblance to the structure of a leg gives most of the features the terms with which they are commonly referred to. Starting with the longest-known and most pronounced features, we find the so-called "knee" at around $4 \cdot 10^{15}$ eV, where the spectrum steepens. At around $3 \cdot 10^{18}$ eV, the spectrum flattens again, which is aptly named the "ankle". At the highest energies, beyond around $4 \cdot 10^{19}$ eV, the spectrum exhibits a high-energy cut-off [1][1]. An additional, more subtle feature that was identified is the "second knee" at about 10^{17} eV, where the spectrum further steepens. The transition region is thought to occur between the "knee" and the "ankle" and has thus recently also been referred to as the "shin" region of the CR energy spectrum [3, 4]. All of these features are thought to arise from changes in the propagation of CRs, as well as in the properties of the CR sources.

In conventional models, GCRs are assumed to originate from supernova-remnant (SNR) shocks [1]. SNRs' total energy output and occurrence rate[2] in the Galaxy provide enough power to sustain the observed CR content in the Galaxy. Calculations of diffusive shock acceleration [7] at shock fronts – generally considered to be the mechanism by which CRs are accelerated – place the maximum energy of SNRs at 10^{14-15} eV [8][3]. Calculations in fast and highly magnetised winds even allow acceleration energies up to 100 times higher [1]. Particles are magnetically confined in the shock, making the maximum reachable energy dependent on the particle's rigidity. Galactic sources reaching their maximum rigidity for protons has widely been considered to be the cause for the CR "knee". The position of the "second knee" at around 26 times higher energies [1, 4] was seen as further substantiation of this, as both the "knee" and "second knee" could be interpreted to arise from the same rigidity-dependent process, the former for protons, the latter for iron nuclei.

There are numerous candidates for EGCR sources. Most are considered to be objects with strong shock fronts that span large volumes, where diffusive shock acceleration can occur. Prominent examples are γ-ray bursts (GRBs), active galactic nuclei (AGN), starburst galaxies (SBGs), or even Galaxy clusters [9].

Past models assumed EGCRs to consist mainly of protons that lose energy during propagation by interacting with the cosmic microwave background (CMB) field [1]. At lower energies, protons were thought to interact with the CMB to create electron-positron pairs to cause the spectral hardening at the "ankle" (so-called 'proton-dip models'). Some models even partly described the "second knee" as a consequence of interaction with the CMB [1]. Under the assumption of a dominant proton fraction, the high-energy cut-off stems from the so-called GZK effect, where protons undergo photo-pion production at

[1] The latest measurement by the Pierre Auger Observatory sets the position of the latter two features at $5 \pm 0.1 \pm 0.8 \cdot 10^{18}$ eV and $4.6 \pm 0.3 \pm 0.6 \cdot 10^{19}$ eV, respectively; in addition, they found a further, hitherto unobserved, softening of the spectrum between the "ankle" and cut-off at $1.3 \pm 0.1 \pm 0.2 \cdot 10^{19}$ eV [2].

[2] The rate of supernovae was initially estimated from observations from other Galaxies [5], but more recently also from direct observations of the Milky Way by the INTEGRAL satellite [6]. They occur with a rate in the order of 2–3 per century.

[3] X-ray and γ-ray data also suggest that they accelerate CRs up to energies of at least $\mathcal{O}$(PeV)-scale [1].

highest energies [1, 10, 11]. In this picture, the "ankle" is considered the energy where EGCRs dominate the measured flux.

Challenges to these ideas have arisen with recent observations, particularly of measurements of the composition to energies beyond the "shin" region. The mean mass reaches its maximum just before the "second knee" at around $6 \cdot 10^{16}$ eV. It then becomes gradually lighter towards the "ankle" [1]. This disfavours a dominant contribution of GCRs accelerated in SNRs up to these energies, which would require that the composition becomes successively heavier up at least the "second knee". Beyond the "ankle", the composition becomes heavier again. This suggests that the cut-off does not stem from the photo-pion production of protons, but rather from a combination of photodisintegration of heavier nuclei in the CMB and a maximum energy scenario of extragalactic sources [4].

In addition, models with SNR shocks as the main accelerators of GCRs in combination with a maximum energy scenario fitted to individual particle spectra at energies below the "knee" predict significantly lower fluxes up to the "second knee" than measured [1]. As for EGCRs, models that include maximum source energies and consider all known interaction and energy-loss processes are fitted to composition and spectrum data only at "post"-ankle energies. While they are in good agreement with data at these energies, they fail to give insight into the EGCR flux at energies below the "ankle" [12].

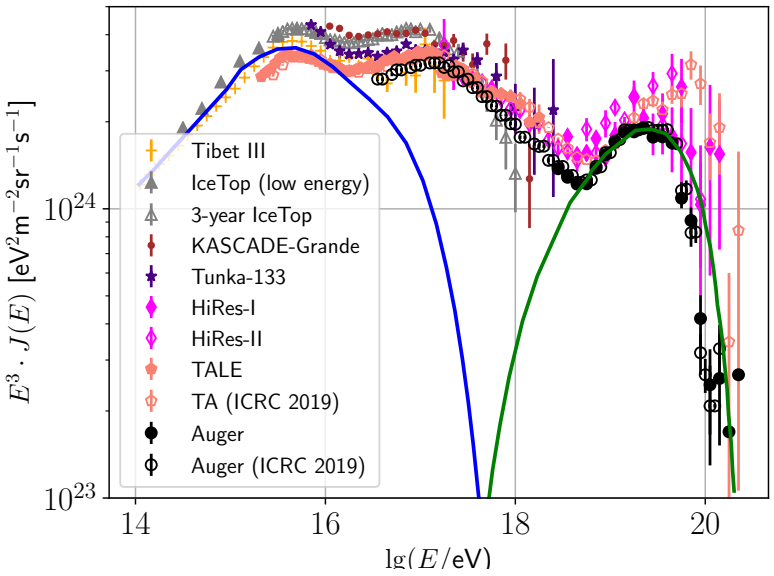

Figure 1.1: Measured energy spectrum combined from various experiments (indicated in legend) [13–21], and conventional models for the expected GCR (blue) and EGCR (green) fluxes (adapted from [1]).

There are extensions to models that increase the maximum energy of GCR sources, and decrease the minimum energy of EGCRs [1, 3, 22–24]. A major challenge in closing in on this gap, however, arises from the fact that there are only few hard observational constraints on the relative contributions of GCRs and EGCRs, and a wide range of models with their own unique assumptions to explain observed features. Generally, past approaches have mostly treated GCRs and EGCRs separately. In understanding the transition region, both components must be accounted for.

A promising avenue to gain insight into the transition region, especially pertaining to effects on observables, such as flux, composition and arrival direction, may be found in studying the effects of the Galactic magnetic field (GMF) itself. This is not only motivated by the fact that CRs of both Galactic and extragalactic origin propagate through the GMF in the final part of their voyage to Earth. In fact, the "shin" region signifies the rigidity range, where CR gyro radii match important length scales of the Galaxy, i.e. the width and radius of the Galactic plane (GP), and even the coherence length of the random component of the GMF. This energy range, therefore, also constitutes a change in propagation regimes from diffusive to ballistic. More concretely, at the lowest rigidities, near the end of the diffusive regime, GCRs are confined in the Galaxy, while EGCRs are effectively shielded from it. Up to intermediate rigidities, the EGCRs that reach the Galaxy are concentrated in the GP, while GCRs more readily escape the GP. At highest rigidities, propagation is ballistic and the deflection of particles by the GMF becomes increasingly negligible. In this thesis, we employ Monte-Carlo-based simulations of CR propagation to identify and quantify these propagation effects, particularly the confinement of CRs in the GP, as well as the shielding of EGCRs from the GP. We additionally attribute these propagation effects to the strength and structure

of the GMF. Finally, we investigate how propagation in the GMF modifies CR observables, such as flux, composition and arrival direction.

The thesis is structured as follows: For the sake of appropriately contextualising the research, we begin with an overview of the relevant physics in chapter 2. This chapter includes the discussion of our current understanding of CRs, in particular their propagation, as well as the structure and topology of the GMF. Next, we present the methodology, as well as the employed simulation software in chapter 3. We turn to the analysis of the propagation effects in chapter 4, where we qualitatively and quantitatively identify propagation features with the help of various key parameters. In addition to that, we investigate large-scale effects resulting from said features. Based on these results, in chapter 5, we identify possible observable effects on the flux, composition and arrival direction of CRs. In chapter 6, these will be contextualised with respect to their implications on the transition region. Finally, the research is summarised and discussed in chapter 7.

Chapter 2

Theoretical Background

This chapter functions as an overview of the relevant physics for this thesis. Many of the subjects covered here will be expounded on in later chapters whenever needed, but a summary and context of what will be discussed is still reasonable, so that the reader may have a sufficiently complete basis to build on without the need to refer to further literature to understand the work discussed in this thesis. Although one can go arbitrarily far backwards in the goal to gain a complete picture of all the concepts described in this thesis, the "return on investment" diminishes drastically the further back one goes.

A suitable starting point is the physics of CRs, beginning with a historical overview and summary of the current knowledge in the field, especially in the context of the transition from GCRs to EGCRs. This includes a summary of current data, the physics of extensive air showers (EASs), as well as ground-based CR detectors, in particular the Pierre Auger Observatory[1]. In addition, an overview of our understanding of the GMF in the context of CR propagation is useful, as this is central to the topic of this thesis. Some theory on relevant mathematical formalisms, such as Liouville's theorem, and the transport equation are also relevant to the reader, as they provide the framework for our current understanding of the propagation of CRs from their sources to the observer.

2.1 Cosmic rays

This section covers a wide range of topics in CR physics. Starting diachronically, we provide a historical overview of the development of the CR physics all the way to our current understanding of properties of CRs. We will further discuss CR observables and CR data, particularly related to the transition from GCRs to EGCRs. Finally, briefly describe CR propagation, the equation of motion and the transport equation, which are relevant to understanding the simulation software used for the studies in this thesis.

2.1.1 Historical overview

The birth of CR physics is directly intertwined with the discovery of radiation itself. Around the turn of the twentieth century, several observations and discoveries of different types of radiation had been made. They include the discovery of electromagnetic radiation by Heinrich Hertz in the 1880s [25], of X-rays by Wilhelm Conrad Röntgen in 1885 (for which he was awarded the first ever Nobel prize in physics in 1901) [26], and of radioactivity by Henri Becquerel in 1896 (which was further studied and elucidated by Pierre and Marie Curie, and was later classified into three different types, namely alpha- (consisting of ionised helium-4 nuclei), beta- (consisting of electrons) and neutral gamma-rays (which are high-energy electromagnetic radiation); all three shared a joint Nobel prize in 1903). With these discoveries, large interest in and further investigation of their sources had been sparked [27].

Early underground measurements of ionising radiation led to the preliminary conclusion that it is likely mainly terrestrial in origin. However, there were sceptical voices, such as Domenico Pacini. He found that the intensity of the ionising radiation decreases with depth under water, concluding that a non-negligible contribution must come from the atmosphere via penetrating radiation [28]. The decisive evidence for this view came from balloon flights performed by Victor Hess in 1912 (see figure 2.1). He found − after an initial drop-off − an increase of the intensity of the radiation with altitude. He interpreted this as a contribution of so-called "Höhenstrahlung" (German for 'altitude radiation') most likely of extra-terrestrial origin (this was later confirmed by Werner Kolhörster in balloon ascensions to even higher altitudes) [29]. These experiments are considered the birth of CR physics, and Hess was awarded the Nobel Prize in 1936 for this work [30].

[1] The special mention of the Pierre Auger Observatory is based on the author's affiliation with it.

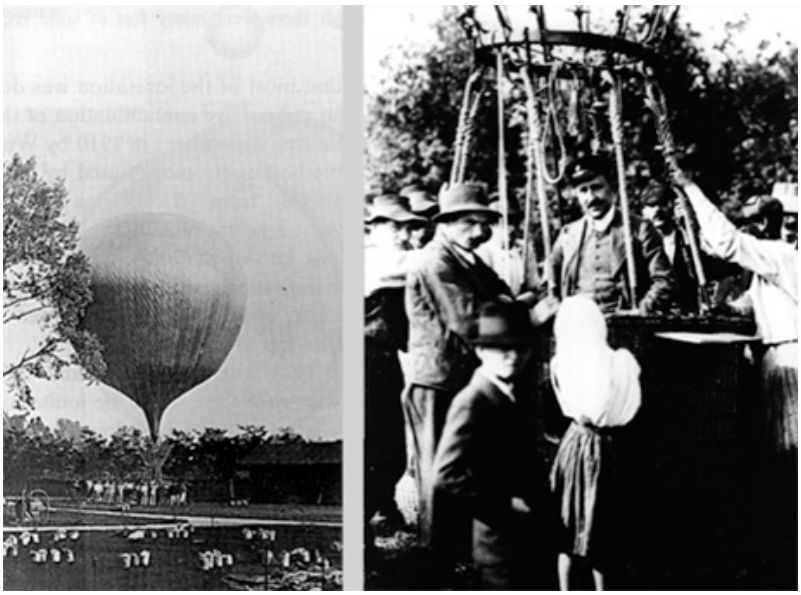

Figure 2.1: Historic photographs of one of Victor Hess's balloon flights (from [31]).

The term "cosmic rays" was coined in the 1920s by Robert Andrews Millikan, believing them to consist of gamma rays produced by the fusion of hydrogen nuclei in interstellar space [32, 33]. However, this conclusion soon came into question. In 1927, Skoblezyn observed groups of highly-energetic particles via their curved tracks through a cloud chamber experiment [34]. In 1929, experiments by Walther Bothe and Werner Kolhörster with gold enclosed by two Geiger-Müller counters employing the newly developed coincidence method[2], showed that penetrating CRs behaved more like charged particles [35]. Finally, the discovery of the east-west effect and the so-called "transition curve" describing the penetrating power of CRs by Bruno Rossi, where CRs were shown to be bent by Earth's magnetic field [36], led to the unambiguous conclusion that they consist mainly of positively charged particles [37]. In addition, Rossi's, Schmeiser's and Kolhörster's work, as well as that of Pierre Auger and his collaborators, showed − using substantially separated Geiger counters − that CRs produce a cascade of secondaries as they penetrate the atmosphere. These would later be named "extensive air showers" (EASs). Auger is largely credited for the discovery of EASs as he additionally made energy estimations of the primary particles, that reached hitherto unseen magnitudes of 10^{15} eV [38]. In the following years, Marcel Schein used isolated lead detectors to show that CRs consist mainly of protons at highest energies [39]. The measurement of CRs also led to the discovery of new elementary particles, such as the muon [40] and the positron [41, 42].

With the help of the theory of electromagnetic cascades which was developed by 1937 [43–45], more information about the primary CRs could be inferred. It was found that CRs span a vast energy range and that the flux decreased significantly with energy, following an inverse power law relation. Enrico Fermi proposed a non-thermal acceleration mechanism in 1949, nowadays referred to as "2^{nd} order Fermi acceleration", which could reproduce such a relation [7]. The first feature in the energy spectrum was identified in 1959 at approximately 10^{16} eV, where it becomes steeper [46, 47]. This feature was called the "knee" due to its resemblance to the anatomy of a human leg.

With the discovery of the cosmic microwave background by Arno Penzias and Robert Wilson in the 1960s [48], Kenneth Greisen, Vadem Kuzmin and Georgi Zatsepin predicted an energy-loss process of CR protons at energies above $\sim 10^{19}$ eV via interaction with this background field, called the GZK effect [10, 11], setting a maximum distance of their sources. However, such ultra-high energy events with values exceeding 10^{20} eV were already observed in 1962 by the Volcano Ranch experiment [49]. This was later confirmed by the Haverah Park experiment in 1973 [50]. In addition, they measured indications of a second feature in the spectrum at around $10^{18–19}$ eV, beyond where it flattens, the so-called "ankle" [51, 52]. These two findings were unambiguously established in the 1990s by, i.a., Fly's Eye experiment and AGASA [53, 54]. However, the origin of these particles could not be identified within the horizon set by the GZK effect. This led to the conception of the Pierre Auger project [55], with the goal to measure CRs at the highest energies and elucidate their origins, culminating in the Pierre Auger Observatory inaugurated in 2008 [56].

[2] Bothe developed the coincidence technique in 1929, for which he was awarded the Nobel Prize in 1954, whereas Rossi improved upon it to allow for larger than twofold coincidences. The latter laid the foundation of "rare event triggering".

2.1.2 General properties of cosmic rays

CRs mainly consist of charged particles. About 99 % of the total CR flux is comprised of atomic nuclei, of which about 90 % being protons, $\sim$ 9 % helium nuclei and around 1 % neutrons or heavier elements [57]. The remaining 1 % consists of electrons and photons. The flux of neutrinos may be comparable to that of photons, except at lowest energies, where processes in the Sun lead to a high neutrino flux [4]. Unsurprisingly, the composition changes as a function of energy, due to source properties and propagation effects.

Due to their charge, tracing CR to their sources and understanding their propagation is not straightforward, as CRs are significantly deflected in Galactic and/or extragalactic magnetic fields of strengths of a few μG or fG–nG, respectively. Therefore, many questions about their sources remain unanswered to this day. Neutral particles, such as photons and neutrinos, do not experience any deflection and point in the direction of their origin. Of these, gamma rays are most ubiquitously measured, but have a plethora of production sites, and, therefore, do not necessarily indicate the direction of CR sources.

Up to around 10^{15} eV, CRs are believed to by or Galactic origin. Their most likely sources are termination shocks of SNRs [58]. CRs above around 10^{18} eV, are most probably extragalactic in origin [59]. Their most likely sources include GRBs, Galaxy clusters, AGN, or SBGs [9]. The latter two are currently most popular candidates [60].

The detection techniques used differ with CR energy: GCRs are directly measurable at the edge of or above the atmosphere via high-altitude balloon and space-based experiments, mainly owed to their large flux. CRs at higher energies, however, are only detectable indirectly via EASs, and their properties can only be inferred therefrom, which leads to systematic uncertainties in this regime [4].

2.1.3 Cosmic ray observables

There are several observables in cosmic ray physics that are used to gain insight into the origins. Those most relevant to the transition from GCRs to EGCRs will be discussed in the following.

The energy spectrum

One of the central and best measured quantities in CR physics is the CR energy spectrum. It spans a vast range of more than twelve orders of magnitude in energy and more than 30 orders of magnitude in flux (see figure 2.2). It is typically depicted in units of the flux, sometimes with an addition energy weight (to better visualise features; see equation 2.1 [4]):

$$[\phi \cdot E^b] = \text{number of particles} \cdot \text{area}^{-1} \cdot \text{time}^{-1} \text{ solid angle}^{-1} \cdot \text{energy}^{\text{b}-1}. \tag{2.1}$$

Apart from energies below 10^{10} eV, the spectrum roughly follows a power law distribution $E^{-\gamma}$, with $\gamma \approx 3$ on average [57]. In concrete numbers, the flux is on the order of hundreds of particles per second per square meter at lowest energies, and drops off to around one particles per square kilometer per century at the highest energies of around 10^{20} eV. The i.e. ness of the spectrum across such a vast range of energies lends itself to the conclusion that CRs are accelerated by only a small number of sources, or by similar mechanisms found in various sources. The theory of diffusive shock acceleration is considered to be the most likely acceleration mechanism for most CR sources. A combination of both explanations is likely to be true [4].

The energy spectrum also contains several features. At around $3 \cdot 10^{15}$ eV, we find the "knee", where the spectral index softens from $\gamma \approx 2.6$ to $\gamma \approx 3.1$ [57]. At around $3 \cdot 10^{18}$ eV, we have the "ankle", where the spectrum hardens again to $\gamma \approx 2.5$ [2]. In this energy range, sometimes also referred to as the "shin" region, the transition from GCRs to EGCRs is thought to occur. This is also the region where measurement techniques shift from direct to indirect, decreasing composition information and introducing uncertainty in the energy estimation. This is part of the reason why the nature of the transition is still not well understood. The "knee" is understood as being caused by either a maximum rigidity of CR accelerators being reached for protons, a rigidity-dependent escape of GCRs from the GP, or a combination of both. The "ankle" is thought to represent the energy beyond which EGCRs dominate the flux. At highest energies, around $5 \cdot 10^{19}$ eV, a flux suppression occurs [2]. It is not clear whether this is a consequence of the aforementioned GZK effect, or of a combination of photo-disintegration and maximum energy scenarios of extragalactic sources, though analyses by the Pierre Auger Observatory favour the latter [61].

For completeness, we allude to an additional feature, the "hip", that occurs at energies below the "knee". It is a hardening of the cosmic-ray spectrum at a rigidity of a few hundred GV for various elements ranging from proton to iron. It has been measured by several experiments in the last decade [62–67]. Though differences exist between the experiments, and statistics are low for the heaviest elements, the reduction in the spectral index is found to be larger than 0.1 for all nuclear species, with a significant deviation for protons as compared to the other elements. The origin of the hardening is attributed to either a change in the energy dependence of the propagation, a change of source properties, or an effect of local sources [4].

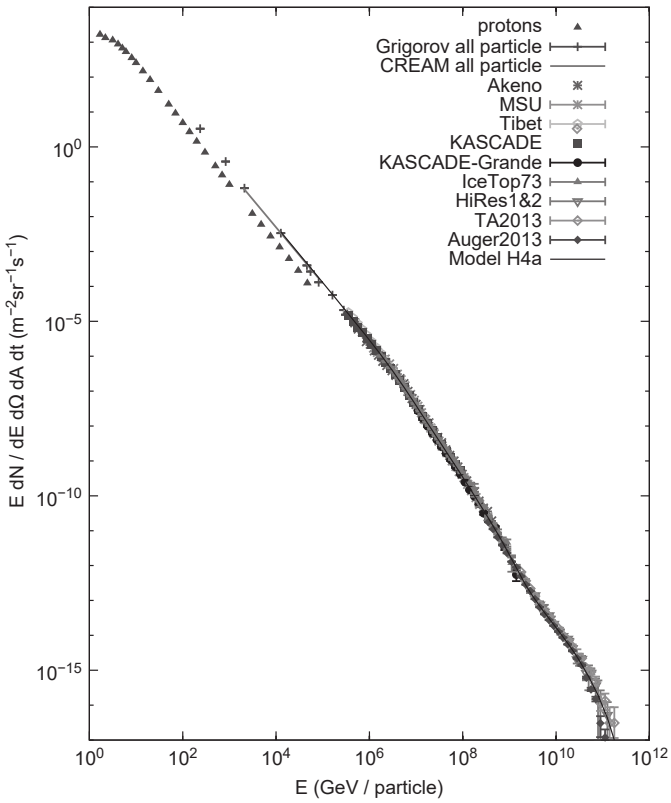

Figure 2.2: Measured energy spectrum combined from various experiments, indicated in legend. The red left-filled data points signify the proton spectrum, which makes up the bulk of the flux at these energies, while the blue filled data points signify the all-particle spectrum (adopted from [57]; references to individual experiments found therein).

Increased statistics of the experiments in recent years, have led to the observation of further, but more subtle, features in the "shin" region. Several experiments, like the Telescope Array low-energy extension (TALE), IceTop and Tunka-133, have observed a spectral hardening at around $2 \cdot 10^{16}$ eV [16, 18, 68].

Kascade-Grande has observed a spectral softening in the all-particle spectrum stemming from the heavy component of the flux. It is positioned at almost precisely 26 times the energy of the position of the "knee", namely $8 \cdot 10^{16}$ eV, and aptly dubbed the "iron knee" [69]. It has been interpreted as the onset of the same charge- or rigidity-dependent process that gives rise to the "knee" feature [70]. Other experiments have also seen a softening of the spectrum at around $2\text{–}5 \cdot 10^{17}$ eV, the so-called "second knee" [16, 68, 71, 72]. This term is also often given to the "iron knee", as all of these features are situated rather close to each other. The "second knee" may in fact be the same feature and as the "iron knee", implying a systematic shift in energy scales between the experiments [18]. If they are distinct features, it seems unlikely that the "second knee" stems the same rigidity-dependent process that causes the other "knee"-like features, as this would imply significant contributions of very heavy nuclei ($Z > 50$) [4]. Another explanation may be the existence of different source classes with different rigidity-dependent maximum energies [4]. The all-particle energy spectrum as measured by several experiments, where the aforementioned features (excluding the "hip") are visible, is depicted in figure 1.1. Measuring other observables, such as the composition and arrival direction, plays a vital role in elucidating the nature of these features.

Cosmic ray composition

Given that CR sources inject a mixed composition of nuclei, all experiments will naturally measure a mixture of nuclear species. Interactions during propagation create secondaries and enhance the contribution of certain lighter elements. In addition, acceleration and propagation effects are all energy-dependent. We thus expect the measured composition to change with energy. Figure 2.3 depicts the energy spectrum for different nuclear species measured with various experiments. Up to about 10^{11} eV, protons dominate the flux, followed by helium, intermediate-mass elements such as carbon, nitrogen and oxygen (also called the "CNO group"), and finally iron. At around 10^{12} eV, the composition becomes heavier and helium dominates. Just below the "knee" energy, the CNO group makes up the bulk of the flux, which is finally surpassed by iron above the "knee".

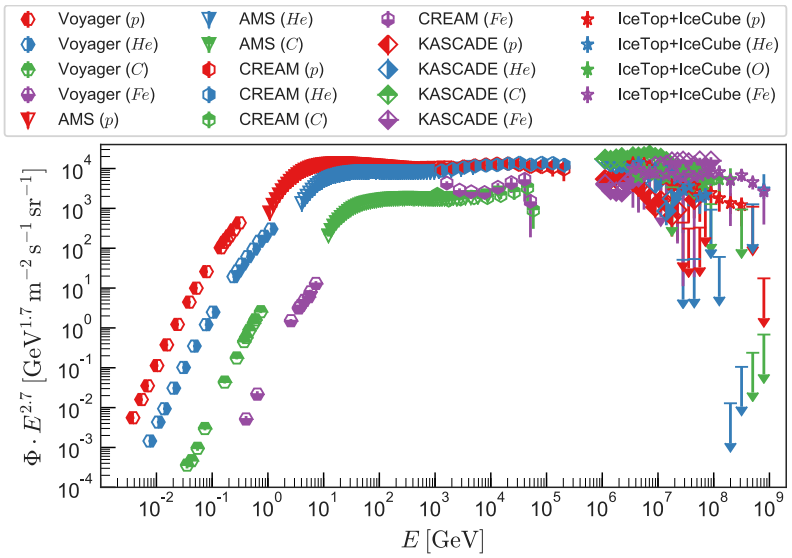

Figure 2.3: Measured energy spectrum for various nuclear species. Different experiments are shown. Both the nuclear species and experiments are signified in the legend (adopted from [4]; references to individual experiments found therein).

At the highest energies, many experiments, such as KASCADE(-Grande), only separate their data into a light and heavy component, due to the indirect detection method of the experiments at these energies[3]. Still, a trend is visible with the composition becoming lighter between 10^{17} eV up to the below the "ankle" [57]. After this, the composition becomes heavier, as observed by the Pierre Auger Observatory using the mean logarithm of the mass number $\langle \ln A \rangle$ up to very highest energies for different hadronic interaction models (see figure 2.4, and [74]). Particularly at the Pierre Auger Observatory, composition and spectral data are combined systematically to constrain various source scenarios [61][4].

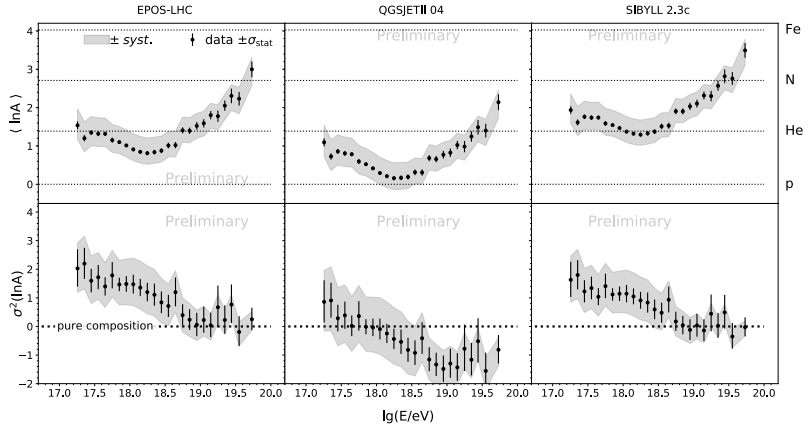

Figure 2.4: First and second mean of logarithm of the mass number $\ln(A)$ above $E = 10^{17.3}$ eV measured by the Pierre Auger Observatory for three different hadronic interaction models, indicated in legend (adopted from [74]).

(An-)isotropies

A measurement of anisotropies or lack thereof in the arrival direction of CRs provides additional information on their origin as well as on propagation effects. They are often measured with multipole analyses, dipoles being the most common and easily detectable. A general challenge of discerning anisotropies lies in their separability from the isotropic background that is significantly larger, particularly for GCRs, where the arrival direction is highly isotropic [75]. This requires a good understanding of systematics of the detector response.

[3] The Pierre Auger Observatory is sensitive to individual nuclei [73], but these data have larger uncertainties, as they are indirectly inferred.

[4] In most current analyses, all three observables, i.e. spectrum, composition, and arrival direction, are combined.

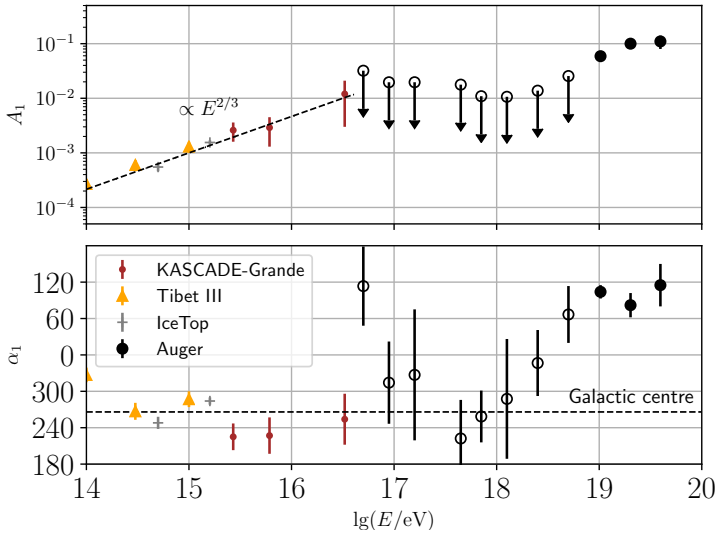

Figure 2.5: Amplitude (upper panel) and phase (lower panel) as a function of energy of the measured CR dipole anisotropy by various experiments, where unfilled markers indicate signficances below $5\,\sigma$ (adopted from [4]; data from [59, 76–80]).

In figure 2.5, the amplitude and the phase of the dipole measured by various experiments at energies between 100TeV and 100EeV is shown. We generally see rising trend for the amplitude, starting from a few 10^{-4} at 10 TeV to 10^{-2} at ≈ 40 PeV. We added a trend line to the data in this energy range of $E^{2/3}$ to illustrate the rough energy dependence. In this energy range, the phase points roughly aligns with the direction of the Galactic centre (GC). This signals an increasing source density in this direction [4]. Above 8 EeV, a dipole in the 10-level has been observed by the Pierre Auger Collaboration pointing away from the GC again, indicating that the extragalactic contribution begins to dominate at energies beyond the "ankle" [59]. Between ≈ 40 PeV and 8 EeV, no significant anisotropies have been measured to date. The amplitude of the best fits as measured by the Pierre Auger Observatory indicate that the amplitude ceases to increase until around 1 EeV, beyond which it begins increasing to match the trend above 8 EeV [80]. Similarly, the phase fluctuates strongly around the GC until the same energy and then starts moving towards the direction of the dipole measured by the Pierre Auger Collaboration.

2.1.4 Cosmic ray transport

On the way from the source to the observer, CRs propagate diffusively through magnetic fields, and through various media, such as gas clouds and nebulae, and undergo interactions, where they may lose energy, as well as create, or decay into, new particles. All of this alters their spectrum, composition and arrival direction. Typically, the transport of CRs is described stochastically as an ensemble of (classical) particles via the Fokker-Planck equation [4]:

$$\frac{\partial f(\vec{x},\vec{p},t)}{\partial t} = -\sum_{i=1}^{6} \frac{\partial}{\partial y_i} \left(A_i(\vec{x},\vec{p},t) \cdot f(\vec{x},\vec{p},t)\right) + \frac{1}{2} \cdot \sum_{i,j=1}^{6} \frac{\partial^2}{\partial y_i\, \partial\, y_j} \left(B_{ij}(\vec{x},\vec{p},t) \cdot f(\vec{x},\vec{p},t)\right), \tag{2.2}$$

where $f(\vec{x},\vec{p},t)$ is the distribution function, $\vec{y} = (\vec{x},\vec{p})$ the phase space, A_i a drift tensor, and B_{ij} the diffusion tensor. In the case of Galactic transport, which is most relevant in the scope of this thesis, we use the differential intensity $n_l = p^2 \cdot f(\vec{x},\vec{p},t)$ and assume isotropy in momentum phase space yielding the following differential equation:

$$\begin{aligned}\frac{\partial n_l}{\partial t} = &\sum_{j=1}^{3} \frac{\partial}{\partial x_j}\left[\left(D_{jk} \cdot \frac{\partial}{\partial x_k}\right) n_l\right] - \frac{\partial}{\partial x_j}\left[u_j \cdot n_l\right] + \frac{\partial}{\partial p}\left[p^2 D_{pp} \frac{\partial}{\partial p}\left(\frac{n_l}{p^2}\right)\right] \\ &- \frac{\partial}{\partial p}\left[\dot{p}\, n_l - \frac{p}{3}\left(\nabla \cdot \vec{u}\right) \cdot n_l\right] + \sum_{j>l} \frac{v_l}{c}\, n_0 \int dp' \sigma_{j\to l}(p,p')\, n_j(p') - \frac{n_l}{\tau} + Q_l(p).\end{aligned} \tag{2.3}$$

The individual terms will be explained in the following (see also [4]).

- Spatial diffusion:

$$\sum_{j=1}^{3} \frac{\partial}{\partial x_j} \left[\left(D_{jk} \cdot \frac{\partial}{\partial x_k} \right) n_l \right] \tag{2.4}$$

D_{jk} depicts the spatial diffusion tensor that is given by the magnetic field properties. Often, it is approximated as independent of $\vec{x}$: $D_{ij} = D \cdot \delta_{ij}$, yielding:

$$-\sum_{j=1}^{3} \frac{\partial}{\partial x_j} \left[\left(D_{jk} \cdot \frac{\partial}{\partial x_k} \right) n_l \right] = D\Delta\, n_l. \tag{2.5}$$

The diffusion coefficient has observationally been shown to exhibit a power law relation with energy $D \propto E^{\kappa}$, where $\kappa \approx 0.3 - 0.5$. This parameter will be discussed in more detail later on.

- Momentum diffusion:

$$\frac{\partial}{\partial p} \left[p^2 D_{pp} \frac{\partial}{\partial p} \left(\frac{n_l}{p^2} \right) \right]. \tag{2.6}$$

This term describes the diffusive change in momentum $\frac{\Delta p}{\Delta t}$, and is closely related to the second order Fermi process.

- Spatial advection:

$$-\frac{\partial}{\partial x_j} \left[u_j \cdot n_l \right]. \tag{2.7}$$

Spatial advection describes the divergence of the flow velocity of the ambient plasma $\vec{u}$, such as Galactic winds. For ultra-high energy CR (UHECR) transport, this term is negligible, as the plasma flow is not relevant.

- Momentum advection:

$$-\frac{\partial}{\partial p} \left(-\frac{p}{3} \left(\nabla \cdot \vec{u} \right) \cdot n_l \right) \tag{2.8}$$

Similarly, this term is described via the divergence of $\vec{u}$, and is a source of energy gain or loss whenever the plasma is compressed. For UHECR transport, this term, too, is negligible.

- Continuous energy loss:

$$-\frac{\partial}{\partial p} \left(\dot{p}\, n_l \right) \tag{2.9}$$

Other continuous changes in energy are included in this term, where $\dot{p}$ determines gain or loss. In the case of nuclei, the types of energy loss are photo-hadronic interactions, ionisation (hadron-hadron) and Coulomb-collisions (the latter two only below GeV-energies), sometimes also adiabatic processes, which more commonly included as an explicit term.

- Catastrophic energy loss:

$$-\frac{n_l}{\tau} \tag{2.10}$$

When nuclei are lost or gained, this is described via the parameter τ, which describes the characteristic loss (or gain) time scale. This term is particularly important in describing the production of photons (γ-rays) and neutrinos, or in the loss of particles in gasses, but also radioactive decay or spallation. Spallation and particle loss are captured by:

$$\sum_{j>l} \frac{v_l}{c}\, n_0 \int dp' \sigma_{j\to l}(p, p')\, n_j(p'), \tag{2.11}$$

where $\tau = (\frac{v_l}{c} \cdot n_0 \cdot \sigma(p)$, with v_l ($\approx c$ in the energy range relevant for this thesis) being the cosmic ray velocity, n_0 the gas density and σ the cross section for the relevant interaction(s).

- Source term:

$$Q_l(p) \tag{2.12}$$

All acceleration processes are summarised in this term. Explicit formulations are not included in the transport equation and are approached separately.

With the transport equation in the Galaxy formulated, it is time to discuss the most important term in the analysis of propagation effects by the GMF, i.e. the spatial diffusion term. The turbulent nature of the magnetic field is the determining factor in the behaviour of diffusion. In quasi-linear theory, and using a homogeneous field with turbulence, the degree of displacement of a particle from a straight line due to diffusion can be described via the following relation [4]:

$$\langle (\Delta x_i)^2 \rangle = 2\,t D_{x_i\,x_i}(t) \propto t^{\sigma}, \tag{2.13}$$

where $D_{x_1,x_1} = D_{\parallel}$ and $D_{x_2,x_2} = D_{x_3,x_3} = D_{\perp}$, and t is the propagation time. The choice of σ describes the type of propagation.

1. Ballistic regime ($\sigma \geq 2$), e.g. for short propagation times, where the diffusive limit of a particle has not yet been reached.
2. Super-diffusive regime ($1 < \sigma < 2$), where propagation behaves anomalously and diffusion occurs faster than Gaussian diffusion (see also [81]).
3. Diffusive regime ($\sigma = 1$), where propagation is stochastic, as for Gaussian turbulence, typically reached after long propagation times.
4. Sub-diffusive regime ($\sigma < 1$), e.g. when displacement does not change with time.

2.2 Cosmic ray detection via extensive air showers and the Pierre Auger Observatory

At energies beyond the "knee" of the CR energy spectrum, and hence in the energy range of the "shin" region, CRs are primarily detected indirectly via EASs. While EASs are otherwise not relevant for this thesis, an overview of properties and physics, as well as the detection of EASs is in order, as it provides a better understanding of the CR data discussed previously. In this context, the Pierre Auger Observatory will be especially highlighted, as it is the one of the central detectors of CRs via EASs that provides the highest-quality CR data at highest energies, and the author is affiliated with it.

2.2.1 Extensive air showers

EASs are cascades of billions to trillions of highly-energetic particles that result from (multiple) collisions (and interactions) of primary[5] or parent CR particles (mainly protons or heavier atomic nuclei), their fragments, as well as energetic secondaries with atmospheric nuclei (predominantly nitrogen, oxygen, and argon). EASs propagate longitudinally with essentially the speed of light in the direction of the incoming primary [82].

Typically, one differentiates between hadronic showers, muonic and electromagnetic showers [57]. In general, the hadronic shower — typically being the parent process — determines the energy transport of the air shower. In most interactions, charged or neutral pions, and sometimes kaons are created. The charged pions have lifetimes in the order of 10^{-8} s. Therefore, they, on average, manage to interact before they decay into muons and neutrinos if their energies exceed a critical value of 30 GeV[6]. Neutral pions, however, have lifetimes more than eight orders of magnitude shorter and, therefore, decay directly into two photons. The electromagnetic cascade is mainly initiated by the photons from the neutral pion decay, which create a successive chain of electron-positron pairs. These, in turn, create more photons via bremsstrahlung. Very rarely do photons create muon-antimuon pairs or hadrons via photoproduction, thus their contribution to hadronic cascade is marginal. However, photon pairs are constantly created via the decay of neutral hadrons, successively shifting the energy to the collection of superimposed cascades that make up the electromagnetic shower. Especially for high primary particle energies, the electromagnetic shower can make up the majority of the shower [83]. Therefore, the energy eventually dissipates due to ionsation loss of electrons and positrons [57]. Secondaries with large transverse momentum $p_{\perp}$ are created in the collisions of hadrons, as well as in the pair-production processes. As a result, the cascade has a lateral spread of up to several kilometers, hence the term "extensive air shower" [82].

[5] The term "primary" is used in two different contexts in CR physics, and can therefore be misleading. In general in this thesis, primaries refer to the CR particles that are ejected from a source; with respect to these particles, secondaries are particles that are created in decays or interactions in the course of CR propagation. In the context of air shower physics, primaries are the CR particles that cause the first interaction in the atmosphere to create the cascade. Therefore, they can be both primaries and secondaries in the "general" senses. Secondaries in the context of EASs refer to any particle created as a result of the first interaction.

[6] The same applies to charged kaons but for slightly larger energies due to their shorter lifetime.

EAS detection and observables

The longitudinal development and lateral extent of the shower depend strongly on the primary energy. At low energies, the cascade development reaches its maximum in the upper atmosphere. The electromagnetic cascade dies out with increasing atmospheric depth, and only muons, with a relatively long lifetime of $\approx 2\,\mu$s, as well as neutrinos reach the ground. At intermediate energies, lower energy parts of the electromagnetic cascade are absorbed by the dense lower atmosphere or by Earth's surface. Muons can propagate underground into greater depths. Extremely high energetic cascades will reach their maximum around sea level and penetrate further into the ground.

As the cascade propagates through the atmosphere, a part of its energy is also deposited in the atmosphere via air Cherenkov, air fluorescence and radio emission. With designated instruments, this allows for the measurement of the longitudinal shower development [82]. The depth of the cascade is expressed in terms of the atmospheric depth $X = \int \rho(l) \cdot l$ to account for the changing density of the atmosphere with altitude. Here, $\rho(l)$ is the density of air along the trajectory of the shower l, which is in units of $\left[\mathrm{g\,cm^{-2}}\right]$. The total number of particles that are produced in an air shower at a certain depth X is referred to as the shower size $N(X)$. In most cases, this does not include neutral particles like photons or neutrinos, as they are usually not detected with current experiments. Sometimes it only includes electrons and positrons as they make up the bulk of charged particles in a (lower energetic) shower that has had more to time to develop. The shower size is mainly dependent on the primary energy. It also depends on the height of the first interaction of the primary, and to a lesser extent on the mass of the nuclear species (or mass number A). Generally, the shower development also has a zenith angle dependence, as inclined showers penetrate larger atmospheric depths before they reach the ground [82]. The average lateral and longitudinal distribution of different components of a proton-induced vertical shower at 10^{19} eV is depicted in figure 2.6.

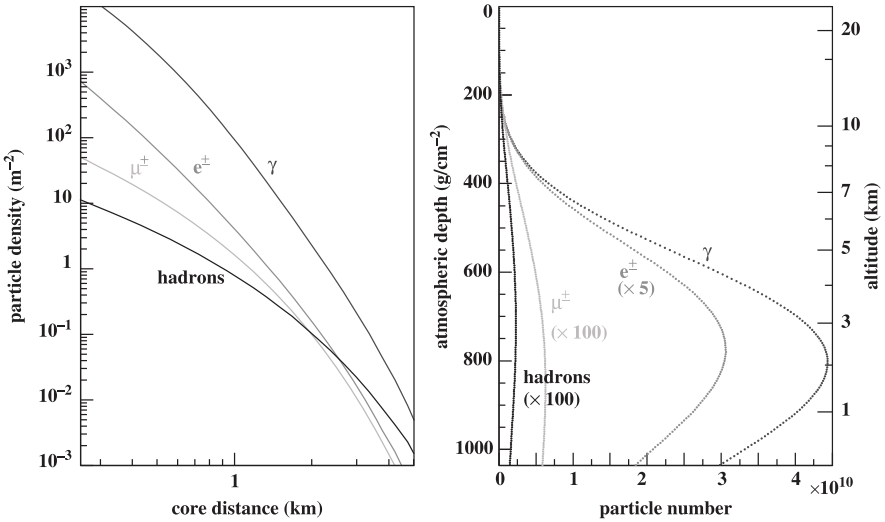

Figure 2.6: Simulation of the average lateral (left) and longitudinal distribution (right) of different components of a proton-induced vertical shower at 10^{19} eV. The former is calculated at 870 g cm^{-2} [57].

An important observable derived from the shower size is the location of the shower maximum, or the (atmospheric) depth of maximum development, $X_{\max}$. By tracking the longitudinal profile of the air shower using detectors sensitive to Cherenkov or fluorescence light, one is able to directly measure this quantity [82, 83]. In figure 2.7, the mean and second moment of the depth of the shower maximum as measured by the Pierre Auger Observatory is depicted.

EASs can also be detected with surface detectors that measure the particle disk, also called the "shower front", arriving at ground. The bulk of the detectable parts of the cascade are the electromagnetic and muonic components. Neutrinos remain undetectable with regular air shower experiments. Due to their large lateral spread, the shower front can only be sampled via a (mostly regularly spaced) surface detector array [82]. The time delay of the signal at each detector station provides information on the arrival direction of the shower [57]. The energy of the shower is not directly measurable, but must be reconstructed via a ground parameter that is calculated from the measured signal. This parameter is compared with shower simulations or cross-calibrated with other calorimetric measurements [57]. If the surface detectors can measure the electrons and muons making up the shower separately, one is sensitive to the nature of the parent particle [83]. The correlation between the number of muons N_μ and the number of electrons N_e of different types of primaries is illustrated in figure 2.8.

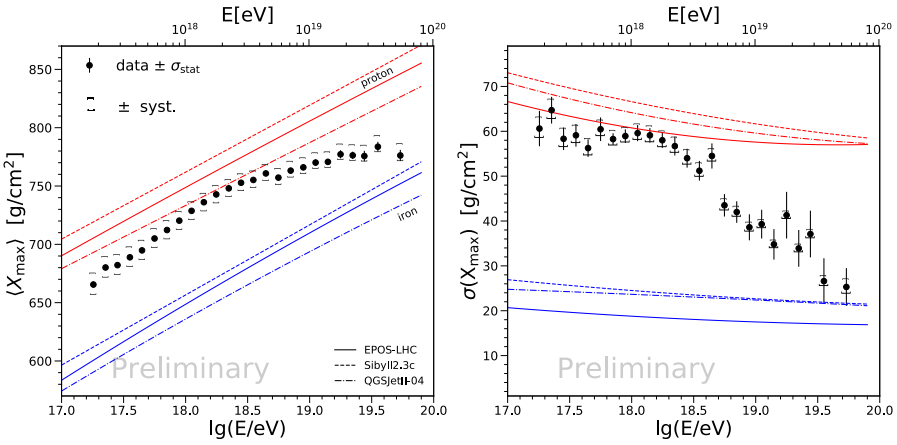

Figure 2.7: First two moments of the maximum shower depth $X_{\max}$ (left: first moment, right: second moment) above $E = 10^{17.3}\,\mathrm{eV}$ measured by the Pierre Auger Observatory [74].

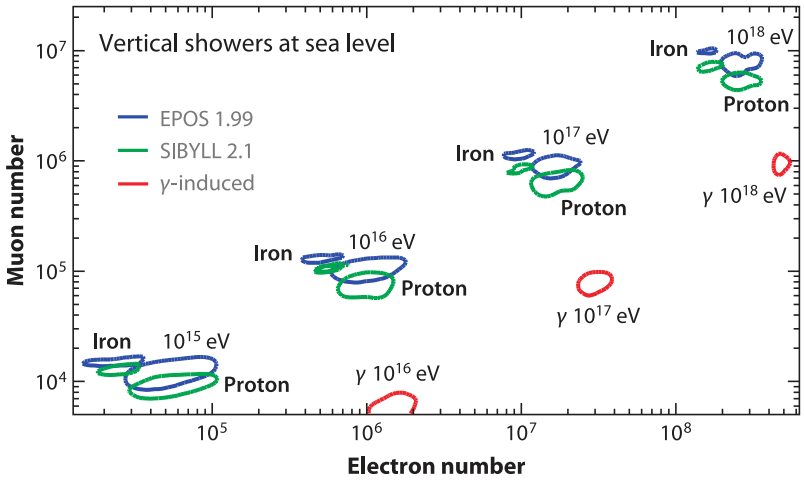

Figure 2.8: Prediction of the correlation between the number of electrons and of muons at sea level for protons, iron and photons from CORSIKA simulations of vertical showers; the proton- and iron-induced showers are simulated using two different hadronic interaction models, signified in legend [83].

The cascade equation

The cascade equation decribes the physics of EASs, where the atmosphere is treated as a calorimeter, although the details differ for the hadronic and electromagnetic parts of the shower. They are particularly useful to understanding the evolution of EASs, and particularly the sensitivity of $X_{\max}$, N_μ and N_e to energy and type of the primary in more detail [83].

The electromagnetic cascade undergoes a particle-multiplication process via the production of electron-positron pairs and subsequent emission of photons via bremstrahlung. Electrons also lose energy via ionisation processes. The energy loss per unit optical depth of an electron can be written in the form:

$$\frac{dE}{dX} = -\alpha(E) - \frac{E}{X_0}, \tag{2.14}$$

where $\alpha(E)$ is the ionisation energy loss and $-E/X_0$ describes the radiative loss with $X_0 \approx 37\,\mathrm{g\,cm^{-2}}$ being the radiation length in air. Particle multiplication continues until a critical energy $E_\mathrm{c} = 86\,\mathrm{MeV}$ is reached, where the energy deposited via ionisation equals that via bremsstrahlung. The basic structure of the electromagnetic cascade is well-described with the Heitler model, where one considers a particle (photon or electron) of energy E_0 which interacts after having traversed a depth of λ and splits into two particles[7], each carrying half the energy. The number of particles at depth X with energy $E \cdot 2^{-X/\lambda}$ is thereby $2^{X/\lambda}$ [83]. The maximum number of particles of the cascade occurs when $E_0 = E_\mathrm{c}$, at a depth that scales with $\ln(E_0/E_\mathrm{c})$ (see figure 2.9(a) and also [83]).

Describing hadronic showers is significantly more challenging as they cannot be analytically expressed,

[7] Photons create an electron-positron pair and electrons emit a photon.

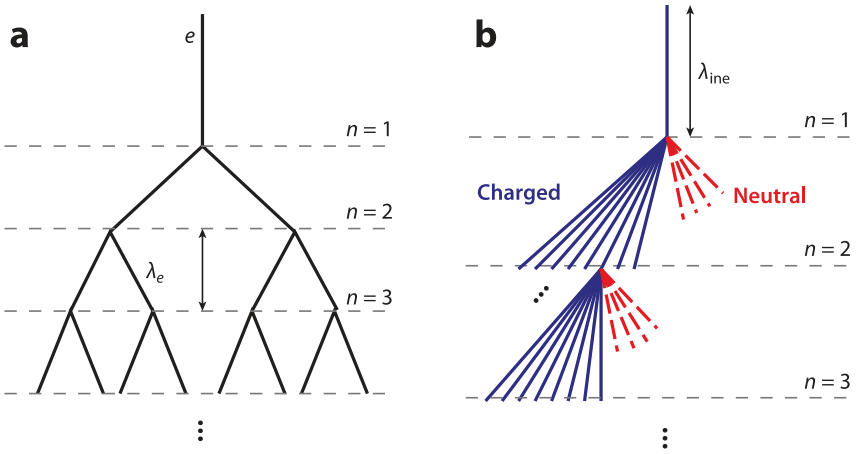

Figure 2.9: Schematic of the simplified cascade model (Heiler model) for an electromagnetic shower (a), as well as the hadronic component of a hadron-induced shower (b); dashed lines represent neutral particles (π^0), and solid lines represent charged particles ($\pi^{\pm}$) [83].

owed to the fact that particle multiplication is vastly more complex and decays need to be accounted for. Numerical calculations have become feasible with the currently available computing power. A generalised Heitler model for hadronic showers does provide insight into some features of hadronic showers (see figure 2.9 (b)). In this model, a hadron produces n_{tot} particles with energy E_0/n_{tot}, two thirds of which are charged and the rest neutral. The latter set immediately decays into two photons, each prompting their own electromagnetic showers, whereas the charged particles that make up the remaining hadronic component interact again to produce a new set of charged and neutral particles in the same ratio as in the previous generation, after a mean interaction distance λ_{int} if their energies are greater than some decay energy E_{dec}. Charged particles whose energy is below E_{dec} decay into one muon. The hadronic component carries only two thirds of the remaining energy with each generation [83].

Already after six generations roughly 90 % of the initial energy is carried by the electromagnetic component of the shower. In fact, the depth of the maximum energy deposit scales with depth of the shower maximum of the electromagnetic shower started by the first generation of the hadronic shower $X_{\text{max}} \sim \lambda_{\text{int}} + \ln\left(E_0/2\, n_{\text{tot}}\, E_c\right)$. The number of electrons at the shower maximum is equal to that of an electromagnetic shower, but with the energy reduced by the factor $\left[1 - (2/3)^2\right]$, which is the fraction of energy in the electromagnetic component of the shower. The number of muons is n_{ch}^n, where n_{ch} is number of charged particles produced per generation and n is the number of generations until the energy shared among the hadrons has fallen to $E_0/(n_{\text{tot}})^n = E_{\text{dec}}$. Eliminating n yields: $N_\mu = \left(E_0/E_{\text{dec}}\right)^{\ln n_{\text{ch}}/\ln n_{\text{tot}}}$. It is worth noting that E_{dec}, n_{ch} and n_{tot} are only the effective parameters of this model and are determined via simulation. However, the model shows that the number of muons depends on the primary energy, as well as the density of the air traversed, and the number of particles, both charged and total, created in interactions [83].

Secondary hadrons are typically produced with transverse momenta on the order of $350 - 400\,\text{MeV}$. Due to this, there is a larger lateral spread in hadronic showers compared as to electromagnetic ones, as the lateral distribution of electromagnetic showers only results from Coulomb scattering on air. Being primarily created via the decay of low-energy pions, the lateral spread of muons is especially wider than that of electrons. Low-energy hadronic interactions also largely determine the muon count at ground [57].

Since atomic nuclei have binding energies significantly smaller than typical shower interaction energies, they are often treated as superpositions of A independent nucleons with energy E_0/A in cascade equations. The number of charged particles of an EM shower is hardly affected by this superposition principle, since the Heitler model does not differentiate between A particles of energy E_0/A and one particle of energy E_0 (the energy dependence lies in the fraction of the energy that the EM component receives). The depth of the shower maximum and the number of muons, however, do depend on the mass of the primary particle [83].

$$\begin{aligned} N_{\text{EM,max}}^{(A)}(E_0) &= A \cdot N_{\text{EM,max}}^{(p)}\left(\frac{E_0}{A}\right) \approx N_{\text{EM,max}}^{(p)}(E_0) \\ X_{\text{max}}^{(A)}(E_0) &= X_{\text{max}}^{(p)}\left(\frac{E_0}{A}\right) \\ N_\mu^{(A)}(E_0) &= A^{1-\alpha} \cdot N_\mu^{(p)}(E_0) \end{aligned} \tag{2.15}$$

More precisely, heavier primaries are expected to initiate showers that produce more muons (for ex-

ample, the number of muons for iron-initiated showers is $\approx 40\,\%$ higher than for protons and their shower maximum is 80–100 $\mathrm{g\,cm^{-2}}$ deeper). The superposition principle can be viewed as an average over several showers of more sophisticated models that take into account nucleus-nucleus interactions and the splitting of nuclei, which explains why it provides a good description of features pertaining to inclusive observables, such as N_μ and the mean of $X_{\max}$. Other observables that relate to correlations or higher-order moments are not well-described [83]. For more a detailed description of hadronic showers, phenomenological models have to be developed that can be extrapolated to higher energies or phases spaces that have not been probed in human-made accelerators [83].

2.2.2 The Pierre Auger Observatory

The Pierre Auger Observatory was conceived in 1992 by Jim Cronin and Alan Watson, and is designed to (indirectly) detect CRs at the highest energies (around 10^{18} eV and above, also called ultra-high energy cosmic rays) by measuring EASs. It is situated in the plains of Pampa Amarilla near Malargüe, Mendoza Province, Argentina [84]. Given the low flux of CRs at these energies, the experiment spans a vast area of $3000\,\mathrm{km^2}$, making it the largest experiment worldwide by area. Its design, as well as its analysis methods are based on knowledge and techniques gathered from predecessors, such as ground detectors first used at the Haverah Park experiment [85], fluorescence detectors employed at (HiRes) Fly's Eye [86], and understanding of air showers developed at KASCADE(-Grande) [69]. It employs a hybrid detection method, where both the particles of the air shower arriving at the ground, and the longitudinal profile of the air shower as it travels through the atmosphere are measured [55][8]. It was founded in 1999, with first measurements being made in 2001 with the engineering array prototype consisting of 40 ground detectors and one fluorescence telescope. The observatory was finally completed and inaugurated in 2008. In the twenty years since foundation, several extensions and upgrades of the experiment have been begun and undertaken. After detailing the general detection method of the experiment, including its limitations, these will be summarised. Unless otherwise specified, all information is gathered from [84].

Hybrid Detection Method

Before the conception of the Pierre Auger Observatory, two main types of detection methods to measure air showers originating from CRs had been in use. One method measures the particles that arrive at ground. The other tracks the shower development via its emission of fluorescence light as the particles in the shower interact with the atmospheric nuclei. The Pierre Auger Observatory combines these two independent techniques with a surface detector (SD), consisting of an array of 1,660 water-Cherenkov stations placed at a hexagonal grid of 1.5 km spacing covering an area of $3,000\,\mathrm{km^2}$, and four fluorescence detector (FD) stations, each consisting of six telescopes that oversee the array to measure the ultraviolet light emitted by these showers in the atmosphere. In figure 2.10, several images showing the distribution of detectors, as well as the individual detectors are shown.

Each SD station is equipped with a solar panel, which powers the entire station, including data processing electronics that process the PMT signal and transmit it to a central server, as well as a GPS device that enables accurate timing measurements. Each station contains 12,000 liters of de-ionised water. High-energy particles of an air shower travel at velocities exceeding the speed of light in water. As they pass through it, they create electromagnetic shock waves that produce Cherenkov light. These are reflected by the lining of walls in the tank and ultimately measured by photomultiplier tubes mounted at the top of the tanks. Containing billions of secondary particles created in the cascade, EASs can cover an area of several tens of square kilometers when they reach the ground and can thereby trigger several SD stations at once. With the amount of light the FD stations detect, the energy of the primary CR particles that initiated the air shower, and from the time signature of the triggered stations the direction whence the particle originated, can be determined.

The FD consists of a grid of focusing mirrors which collect the UV fluorescence light emitted from atmospheric nitrogen nuclei excited by the high-energy air shower particles traveling through the atmosphere. They guide this light to a camera of PMTs, which is sensitive enough to measure air showers at distances up to 15 km. The intensity and timing information of the tracks measured by the FD provides very precise calorimetric information with which the primary particle's energy can be measured. On occasion, an air shower profile is visible in two telescopes. These are so-called "stereo" events and provide the most precise directional reconstruction of the CR primary.

Combining the SD and FD allows very high accuracy reconstruction of shower geometry, as well as the calorimetric energy, which is used as proxy for the CR primary energy. In addition, by comparing the signals of both methods, the SD can be cross-calibrated with the FD to provide a model-independent energy reconstruction by the SD. This is especially useful as the FD can only be operated on clear, moonless nights, giving them a duty cycle of about 14 %, while the SD are constantly taking data.

[8] Another such hybrid observatory measuring UHECRs, about one quarter the size of the Pierre Auger Observatory ($762\,\mathrm{km^2}$), observing the northern sky is located in the high desert of Millard County, Utah, at the former site of the Fly's Eye experiment, called the Telescope Array [87].

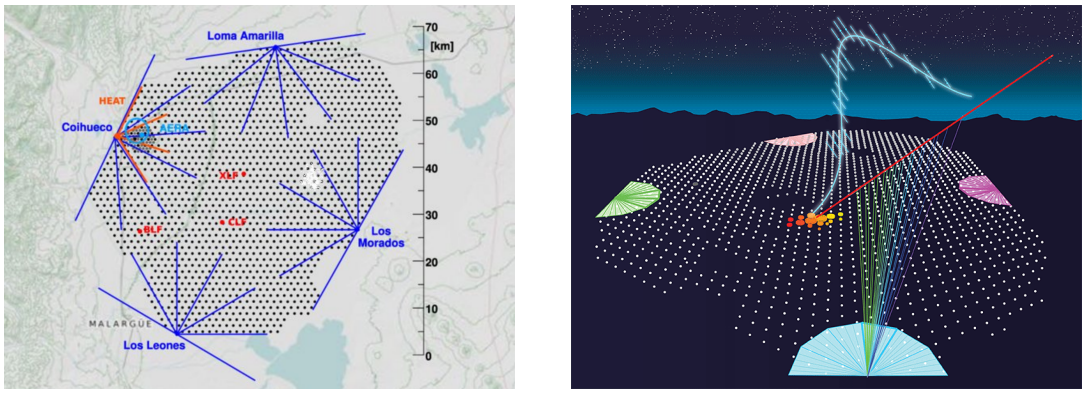

Schematic map of the Pierre Auger Observatory; left: bird's eye view of the area, with black dots indicating position of SD stations, and the four sets of six blue concentric lines indicating the position and rough field of view of the FD stations (from [13]), right: side view with an EAS and its longitudinal profile illustrating the hyrid detection method of the Observatory (from [88]).

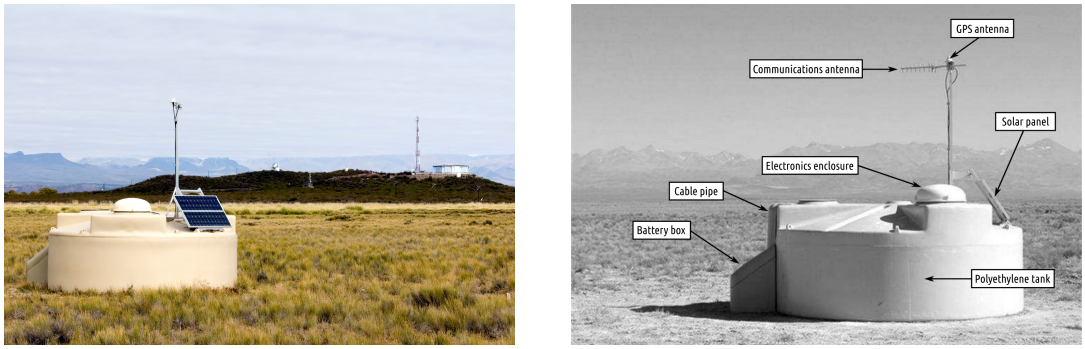

Surface detector (from [89]); left: photograph of an SD station with one of the FD stations in the background, right: photograph of SD with components described.

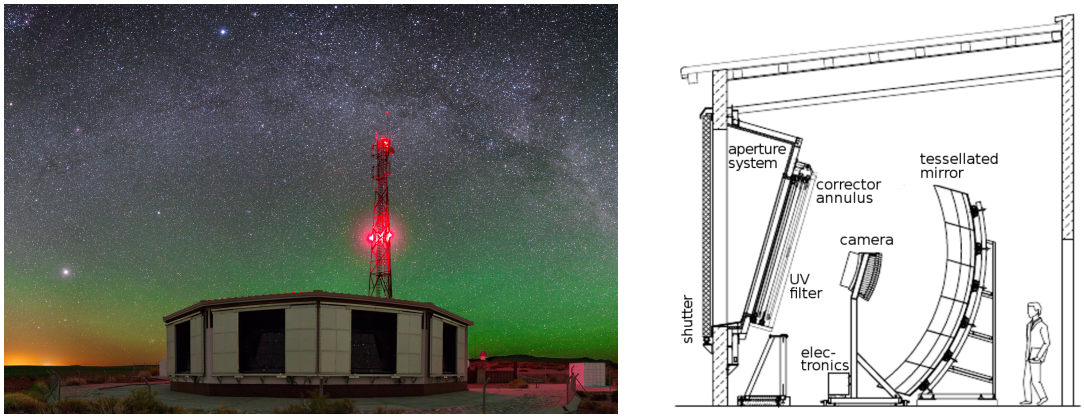

Fluorescence detector; left: photograph of a FD station at night (from [89]), right: schematic of setup of a telescope of the FD (from [90]).

Figure 2.10: The Pierre Auger Observatory and the two components of its hybrid detection method.

Auger Engineering Radio Array (AERA)

Another method of detecting air showers is via their radio emission. To this end, the Pierre Auger Observatory developed the Auger Engineering Radio Array (AERA), an antenna array which measures the short radio pulses emitted by CR air showers. It consists of 149 radio antennae covering an area of 17 km^2 [13] which are sensitive in the frequency range of 30 to 80 MHz (the top left image in figure 2.10 of the map of the Pierre Auger Observatory indicates in cyan the position of AERA). They are made up of two types of antennae, namely ten logarithmic-periodic dipole antennae (LPDA) with 175 m spacing, and 100 so-called "butterfly antennae" that are spaced 250 m, 375 m or 750 m apart from one other. Additional prototype stations with the ability to measure the electric field vector in 3D and at lower frequencies have also been installed. The two individual antenna types are shown in figure 2.11.

AERA is particularly well-equipped to measure horizontal air showers, that are purely electromagnetic. It regularly detects CRs in coincidence with the SD and FD, and has proved a successful complementary detection technique for measuring air showers, particularly the energy of CRs, with the added benefit that it can be operated at all times, like the SD array.

(a) The LPDA antenna.

(b) The butterfly antenna.

Figure 2.11: Photographs of the two antenna types employed in AERA (from [89]).

Auger Muons and Infill for the Ground Array (AMIGA)

With the current spacing of surface detectors, the minimal energy of CRs measurable by the Pierre Auger Observatory is in the order of 10^{18} eV. With the Auger Muons and Infill for the Ground Array (AMIGA) project, the goal is to extend the range to below 10^{17} eV, with which the transition from GCRs to EGCRs may be studied.

AMIGA consists of a denser "infill" array of 61 surface detectors of half the regular spacing of 750 m covering an area of 23.5 km^2[9], each equipped with an underground muon detector (UMD), consisting of 61 plastic scintillators that are buried 2.5 m in the ground underneath the detectors to detect only the muon component of the showers [13]. With this, composition information on an event-by-event basis is possible, as the muon component of an air shower depends strongly on the nuclear species of the primary CR particle. Figure 2.12 shows a schematic, as well as a photograph of such detector module.

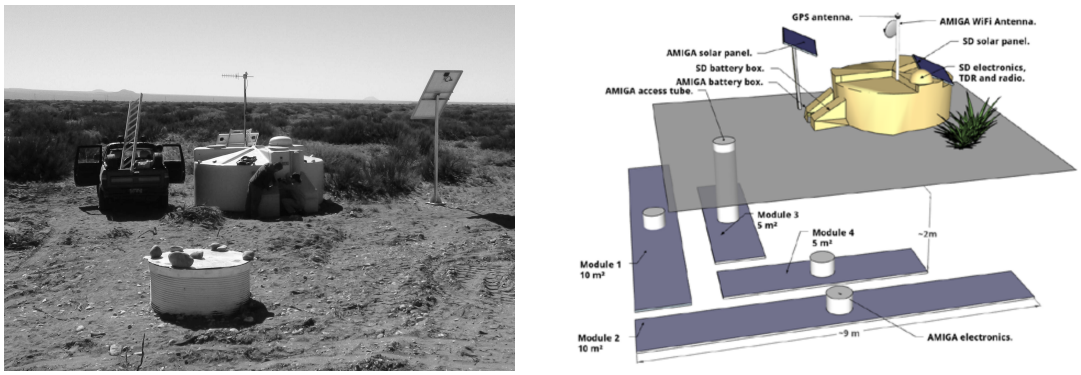

(a) Photograph of one AMIGA detector component (UMD and WCD).

(b) Schematic of one AMIGA detector component (UMD and WCD).

Figure 2.12: One of the individual AMIGA detector components (muon detector forming the UMD and the WCD station; from [89]).

High Elevation Auger Telescopes (HEAT)

As low-energy CRs particle produce air showers that penetrate less deeply into the atmosphere, the regular fluorescence telescopes are not able to measure the important parts of the shower, making profile reconstruction very difficult. Therefore, High Elevation Auger Telescopes (HEAT), telescopes that observe the atmosphere at greater heights, were installed at the Coihueco site (the top left image in figure 2.10 of the map of the Pierre Auger Observatory indicates in red the position of HEAT). HEAT consists of three

[9] The infill extends the trigger threshold of the SD array downward by one decade in energy. Detectors have additionally been added at the central point of the 750 m-triangles to access even lower energies.

fluorescence telescopes, mounted in separate containers that can be inclined at an angle of up to 60 degrees (see figure 2.13). This enables the detection of the longitudinal profile of EASs initiated by lower energy CRs.

Figure 2.13: Photograph of HEAT (from [89]).

AugerPrime

The composition data collected by the Pierre Auger Observatory indicate a mixed composition that becomes heavier towards highest energies, which lends itself to the interpretation that the high-energy cut-off in the CR energy spectrum results from the cosmic accelerators having their maximum rigidity, rather than being caused by the GZK effect. Superficially, this appears to be in conflict with TA data, which is consistent with a pure proton composition up to highest energies [91]; this inconsistency has been found to disappear in joint analyses of TA and Pierre Auger Collaboration working groups, given the current statistics of both experiments [92]. In addition, a mixed composition would also imply stronger deflections in magnetic fields during propagation and thus make source identification more difficult.

Currently, composition information is acquired using the depth of the maximum air shower development X_{max}. Its distribution in logarithmic energy bins is compared to predictions from hadronic interaction models (see figure 2.7). The composition information drawn from this is only statistical in nature. Therefore, improving composition inferences at highest energies to an event-by-event level, where measuring composition-dependent spectra and anisotropies, as well as gathering more statistics in a shorter time are the main objectives of the AugerPrime upgrade [13].

These goals are to be achieved via an instrumentation upgrade of all detector components. First, each surface detector station will be equipped with a plastic scintillator to better discriminate the hadronic/-muonic and electromagnetic components of the air showers. Furthermore, the SD station will receive an additional PMT, the electronics will be improved, and the dynamic range of the surface detectors will be widened. This will enable measurements of showers closer to the core, allow backwards-compatibility with pre-upgrade data, and increase the timing accuracy of the SD. The AMIGA project is also part of the AugerPrime upgrade. In addition, thanks to the success of AERA, each surface detector station will be equipped with an antenna to measure the radio pulses of the air showers as part of the full array radio upgrade. This will provide an excellent complementary measurement technique, especially of particle type (see figure 2.14). Lastly, efforts are made to increase the duty cycle of the FD by reducing the high voltage of the PMTs of the cameras during times when the Moon is closer to the horizon and its elumination is more than 70 % [13].

2.3 The Galactic magnetic field

The GMF constitutes one of the big “known unknowns” in Galactic astrophysics, but − more relevantly − in CR propagation. While the magnitude of its contribution and its vast importance is acknowledged, it still remains a largely neglected and poorly understood entity. This comes as no surprise when one considers that it stems from a complex array of phenomena of varying scale in length and energy, and itself interacts with those very phenomena. Therefore, attempting to characterise it is a very non-trivial task. In this section, an overview of the current understanding of the origin and structure of the GMF will be given, and its effects on CR propagation. It will include a description of the available observables used to model the GMF, and the connected challenges, but also current opportunities and progress will

Figure 2.14: Photograph of the upgraded SD station equipped with a scintillator as well as an antenna on top of the tank (from [89]).

be outlined. We will be drawing a bulk of the information presented here from [93] and [94], the former of which gives a review of the observational studies employed to determined the GMF at all scales, and the latter presenting the to-date most current status of the large-scale magnetic field (which is most relevant for the propagation of EGCRs). In addition, a description of the state-of-the-art GMF models is given in [95]. All three give excellent overviews deserve a read of their own, but the aspects relevant for CR propagation are worth detailing separately, which will be done in the following. Starting with an overview of the relevant terminology that may be necessary due to slightly inconsistent use thereof (see section 2.3.1), we will continue with an overview of the available observables, and their limitations (see section 2.3.2). This will be followed by a discussion of the existing GMF models (see section 2.3.3). Lastly, conclusions on CR propagation will be presented in section 2.3.4.

2.3.1 Terminology

This section deals with the terminology relevant for describing the GMF in order to provide a clear description thereof. Some terms require some accompanying insight into the structure of the magnetic field, that will be included when relevant, but will be elaborated on in later sections.

Large- and small-scale fields

The most basic description of the GMF pertains to the length scales that are relevant. The distinction between different length scales is motivated by the fact that different phenomena, that act on different scales, give rise to and interact with magnetic fields. While, traditionally, the differentiation included a turbulent small- and an ordered or coherent large-scale field, more recently, a three-component distinction has gained traction. Here, in addition to the two components described above, a third component is included, where the direction of the field lines varies on small scales but the orientation does not. It is hence referred to as an anisotropic random, ordered random or striated field. In contrast, the small-scale isotropic random component is assumed to be a Kolmogorov-type field. It follows a power law containing an outer energy injection scale, in which energy cascades all the way down to a dissipation scale, where the energy dissipates. The large-scale field (roughly) follows the spiral arms of the Galaxy or is ring-shaped. Its configuration is often described in terms of symmetries with respect to the GC and GP, and sometimes consists of further components, namely a Galactic disk and halo that follow different symmetries with

respect to the symmetry axis, or plane, respectively.

For spiral fields, the definition of the pitch angle p is useful, which depends on the ratio between the radial and azimuthal component of the magnetic field B_r and B_φ (see equation 2.16):

$$p = \arctan \frac{B_r}{B_\varphi}. \tag{2.16}$$

If the two components have opposite signs, we speak of a trailing spiral.

The three field components vary in their morphology, which can be distinguished in the tracers or observables typically used to describe them. Therefore, it is sensible to list these tracers and how they manifest for the different components.

2.3.2 Observables

All observables described in the following only provide an indirect way of determining the GMF. In this section, we separate the different tracers by the direction with respect to the line of sight and the orientation of the field that they probe.

Faraday rotation measures

Faraday rotation measures use polarised light emissions at various frequency bands to determine the line-of-sight component of the magnetic field $B_\parallel$. It makes use of the fact that linearly polarised light in a magnetised plasma with thermal electron density n_e experiences frequency-dependent Faraday rotation. The rotation measure is defined as the product of $B_\parallel$ and n_e integrated along the distance between the source of the light and the observer s (see equation 2.17 [96]):

$$\left(\frac{\mathrm{RM}}{\mathrm{rad\,m^2}}\right) = 0.812 \int_{\mathrm{source}}^{\mathrm{observer}} \left(\frac{n_e}{\mathrm{cm^{-3}}}\right) \left(\frac{B_\parallel \cdot ds}{\mu\mathrm{G} \cdot \mathrm{pc}}\right). \tag{2.17}$$

If RM is positive, the field is pointed towards the observer, for a negative RM, away from the observer. With light from extragalactic sources (usually via radio emission), 3D information is lost and only the projected field may be determined. Pulsars, however, provide 3D information if the distance to the pulsar is known. For mixed emitting and rotating media, it is more useful to derive a Faraday spectrum, which gives us the polarised intensity with Faraday depth ϕ. In this case, equation 2.17 is modified such that the rotation measure is determined for different integration boundaries along the line of sight.

Equation 2.17 assumes that $B_\parallel$ and n_e are uncorrelated which is not a valid assumption for fields strong enough to affect their surrounding media. In addition, estimates of the electron density are needed, but these are not always precise. In general, the relationship between $B_\parallel$ and n_e is still in need of a more detailed understanding. In figure 2.15, the all-sky Faraday rotation map from extragalactic radio sources measured by [97] (adopted from [96]) is shown.

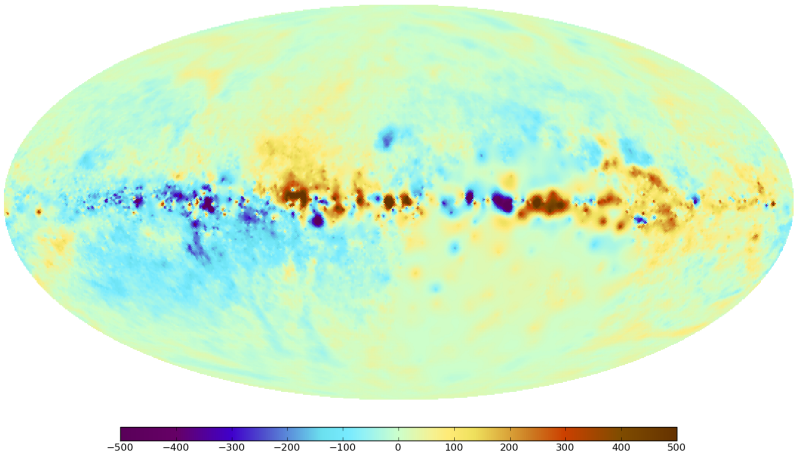

Figure 2.15: All-sky map of Faraday rotation [$\mathrm{rad\,m^{-2}}$] from extragalactic radio sources (from [96, 97]). For a positive RM, the field is pointed towards the observer, for a negative RM, away from it.

Diffuse synchrotron emission

Synchrotron radiation that is emitted as CR electrons are deflected by the GMF is a dominant source of radio to microwave signals across the sky. It is a tracer of the magnetic field component perpendicular to the line of sight $B_\perp$ via the following relation (see equation 2.18):

$$I(\nu) \propto \int n_{\mathrm{CR}}(\nu,\, s)\, B_\perp\, \nu^{-\alpha}\, ds, \tag{2.18}$$

where $n_{\mathrm{CR}}(\nu,\, s)$ is the CR electron density, ν the frequency of the photon and s is the path length that the photon travels on the way ot to the observer [96]. Measuring the magnetic field component perpendicular to $B_\parallel$, serves as a complementary tracer to the Faraday rotation measure.

n_{CR} is the parameter that is subject to the largest uncertainty. In most cases, based on ideas of energy equipartition between CRs and the magnetic field, n_{CR} and the magnitude of the magnetic field squared $|\vec{B}|^2$ are assumed to be completely correlated. However, particularly at turbulent scales, i.e. above certain field strengths, this correlation does not hold. The left sky map in figure 2.16 depicts the synchrotron emission at 30 GHz measured by the Planck Collaboration [98], (adopted from [96]).

Synchrotron radiation is highly linearly polarised, which additionally serves as a tracer of the magnetic field morphology. During propagation, it suffers wave-length dependent depolarisation due to magnetic field effects, such as magnetic field tangling. This is most prominent at radio frequencies, where ground-based detectors measure and most of the available data stems from. Space-based experiments that measure in the microwave band, where many of the effects that lead to depolarisation are not present, are more suitable to measure the polarisation. However, due to the fact that the signal at microwave frequencies is contaminated by emissions other than synchrotron emission, and most individual data sets are not absolutely calibrated and thus shifted by an unknown offset with respect to one another, determining the degree of polarisation remains a challenge to-date. This could be overcome if n_{CR} was better understood, enabling a combination of the radio band, where the total intensity is dominated by synchrotron radiation, with the microwave band, where polarisation is largest.

Thermal dust emissions and polarised starlight

Non-spherical dust grains tend to align with the magnetic field lines along their long axes, perpendicular to which they have their spin axes. Emissions from such dust grains are thus polarised perpendicularly to the local magnetic field, and can be used to probe the component perpendicular to the line-of-sight $B_\perp$. The alignment is thought to depend strongly on the strength of the magnetic field, but also on grain properties and the environment, of which the latter two are not well understood. Though similar to synchrotron emission, dust emissions stem from different regions in the interstellar medium close to the GP, and are thus complementary to it. With an understanding of the thermal dust emission in three dimensions, a distinction between local and kpc-distance sources of synchrotron emission may be possible. The right sky map in figure 2.16 depicts the dust emission at 353 GHz measured by the Planck Collaboration [98], (adopted from [96]).

In addition, the alignment of the dust grains leads to linear polarisation of starlight parallel to $B_\perp$. Given that the distance to the stars is often known, starlight provides information on the magnetic field in three dimensions. This is especially useful to probe the local (large-scale) magnetic field. However, due to low sampling of far-away stars in- and outside of the GP (as well as low accuracy distance determination of the former), its determinability is limited.

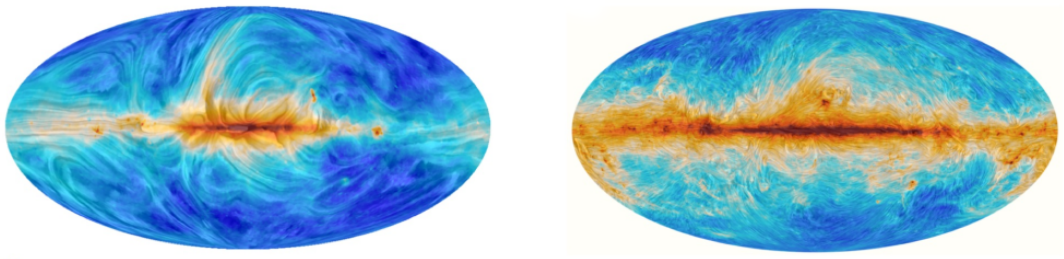

Figure 2.16: Sky maps of the angle of polarisation due to synchrotron emission at 30 GHz (left) and due to dust emission at 353 GHz (right); the colour depicts the intensity (where blue depicts low values, and brown high values), and the applied texture indicates the inferred plane-of-sky magnetic field direction, meaning the polarisation direction rotated by 90° (from [96, 98]).

Further challenges

Since all components of the energy density of the Milky Way, such as CRs, radiation, turbulent gas and magnetic fields are of comparable magnitude, and thus all provide feedback to the entire system, all observables are interconnected with others. As alluded to when introducing the observables above, they all depend on other components of the interstellar medium other than the magnetic field, such as the CR electron density, dust grain properties, and hot ionised gas densities.

The understanding of the CR electron density is already limited in its sources and propagation, especially in terms of anistropic diffusion. Models that seek to estimate the density often use fixed magnetic field models, though joint modelling of both would provide a better understanding. Dust grain distributions are modelled on the basis of the same observables used to determine the magnetic field, namely thermal emissions and starlight polarisation. The main challenge in making any inferences is the fact that the properties of the grain and the environment differ for different regions of the Galaxy and are thus poorly constrained. The hot ionised gas medium is determined via various observables. For instance, they emit bremsstrahlung in the micro wave bands, the spectrum of which is very similar to that of synchrotron emission, such that they are hard to separate especially in the GP. Another observable is the dispersion measure of the pulsars, which is most widely used in current models. The largest uncertainty of all of these models is how to deal with the clumping of the medium, and how they depend on small-scale fluctuations of the GMF.

All observables used to determine the GMF are themselves based on observables that depend on the magnetic field at various scales, which constitutes the main challenge in all modelling attempts. Therefore, approaches that employ robust statistical analyses that are able to combine various observational data, theoretical insights and simulation studies to create more comprehensive and self-consistent models seem indispensible, and are becoming increasingly feasible.

2.3.3 GMF models

The most generic model to describe the Galatic magnetic field is a vector field with an infinite number of degrees of freedom, where each point in space is ascribed an amplitude and direction. In principle, any description of the magnetic field that seeks to simplify this model relies on some assumption about its structure, in order to significantly reduce the number of degrees of freedom, while simultaneously being able to describe most, if not all relevant features. Given the indirect nature with which one is able to determine the GMF via observables, additional assumptions particularly about the structure of the Milky Way itself must be made. Herein lie the limitations of all inferences of the GMF. A number of models with varying complexity (i.e. degrees of freedom) – and thereby also plausibility – are used to describe the GMF. They are mostly based on either ad hoc constructions to fit observations or on theoretical considerations, such as dynamo theories and magneto-hydrodynamics [94]. They all have certain morphological features in common, which will be discussed in the following, such as spiral disc region and a halo field. Some of these were discussed in the terminology section (see section 2.3.1). Most employ an axis-symmetric spiral approach and a constant pitch angle of $-11.5\,^\circ$ for the disc region. Uncertainties from particle distributions lead to low constraints on details of the field, however, such as the scale height and strength of the coherent magnetic field, and the exact spiral structure (e.g. the extent to which the field follows the material distribution). Though some models provide statistical error bars in their parameters, the systematic uncertainties call into question the extent to which they are in fact constrained. Projections of the regular components of a selection of GMF models from the last two decades are shown in figure 2.17, from the GP (i.e. x-y plot at $z = 0$), as well as a vertical cut (i.e. x-z plot at $y = 0$).

Reversals in the field along the disk region are one key observation that have come up recently. Their exact location is still not well constrained, however, due to poor distance measurements of the associated observables (mainly consisting of pulsars or extragalactic rotation measures). Another morphological feature considered in recent models are the vertical field components that are based on edge-on observations of magnetic fields of different galaxies. They are expected from a Galactic dynamo, as well as from Galactic winds. However, due to uncertainties in the associated parameters, such as particle distributions, it still remains an open question, whether such components exist (to a significant degree) in our Galaxy.

The turbulent component is subject to uncertainties from local structures that take up large angular scales, which may affect modelling if not treated carefully. A further source of uncertainties are poorly understood correlations on small scales that affect larger-scale structures. Furthermore, this component is often modelled assuming a Gaussian distribution where the turbulence has equal power in all directions, which is not in line with observations. Improvements in the modelling of the turbulence may be achieved via more sophisticated magneto-hydrodynamical simulations that tie manifestations of turbulence at various scales to observables and thus allow better constraints from data.

Throughout all analyses performed in the scope of this thesis, the JF12 model [100, 102] (see also the centre plots in figure 2.17), that is a default GMF model implemented in the CR propagation software CRPropa [103], will be employed for the simulations (see also chapter 3). It is therefore sensible to describe and discuss the features and limitations of this model. It is based on synchrotron intensity (both

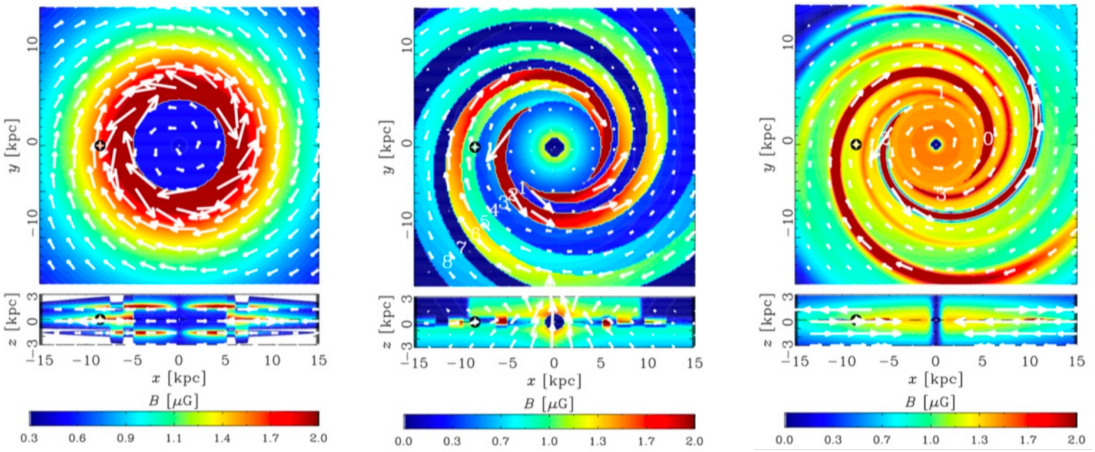

(a) GMF model by [99]. **(b)** GMF model by [100]. **(c)** GMF model by [101].

Figure 2.17: Projections of the regular/coherent component of three different GMF models; top panel: the GP (i.e. x-y plot at $z = 0$), bottom panel: a vertical cut (i.e. x-z plot at $y = 0$) (from [96]).

total and polarised), as well as extragalactic rotation measures as their data input. It was created via a Markov-Chain-Monte-Carlo likelihood analysis of a three-dimensional model that includes a thin and a thick disc component, eight spiral arm (including inter-arm) segments and a halo field that is x-shaped [96]. It uses the NE2001 thermal electron density model, a CR electron model based on "71Xvarh7S" from Galprop [104]. Random components are bootstrapped statistically using an analytical model to represent the spatial variance of the field applied to the WMAP synchrotron emission. One drawback of this is that the synchrotron data is contaminated by other sources of radiation and thus produces a bias in the random field component estimate. This has been attempted to be remedied by Unger & Farrar by using modified data sets for synchrotron emission from Planck and WMAP [105]. In it, they additionally included alternative thermal electron models and CR distributions. They also substituted the ad hoc x-shaped halo field with models based more on first principles and constrained by other observables. This was done in order to reproduce the data on the rotation measures from extragalactic radio sources and the synchrotron emission in the microwave band, and to estimate the uncertainty of the knowledge of the GMF [105].

The spiral structure is based on the large-scale reversals in the magnetic field. However, it does not use any distance information from Galactic pulsars for the locations. Rather, it is assumed that the field along magnetic arm has the same orientation.

2.3.4 Conclusions on cosmic ray propagation

CRs as charged particles are deflected in the presence of magnetic fields, thus particles observed at Earth will never exactly point to the their sources, except for rigidities beyond $\sim 10\,\mathrm{EV}$, where the gyro radius of the CR particle becomes larger than the extent of the Galaxy (assuming that they are not significantly deflected in extragalactic fields during propagation).

For lower rigidities, particle trajectories can be modified in various ways, illustrated in figure 2.18. Diagrams (a) and (b) indicate helical motion in a constant, uniform magnetic field, and a non-uniform field, respectively. For even lowest rigidities, particle trajectories are affected by irregularities in the field. Diagram (c) depicts the scenario where the scale irregularity is significantly larger than the particle's gyro radius. In such a case, the particle may drift away from the field line at the deviation. The lack of impact for a high-rigidity particle where the irregularity is significantly smaller than the particle's gyro radius is shown in diagram (d). When the particles gyro radius is of similar scale as the irregularity, then the nature of the irregularity determines the effect on the particle. They include "scattering" in forward (e) and backward direction (f), "trapping" (g), or resonant scattering onto another field line (h) [57].

Unsurprisingly, a proper understanding of the morphology and strength of the magnetic field becomes increasingly indispensible, if source information is hoped to be retrieved. In addition, given that the CR energy density is of the same scale as the dust, gas and magnetic field energy density in the Milky Way, CRs themselves interact with the entire Galactic system, including the magnetic field, which complicates matters further. Although the number density of $>$ PV-rigidity particles, which are the object of study in this thesis, is too low to play a role in these feedback mechanisms shaping the structure of GMF, deflections by the GMF are still large enough that a proper understanding of the GMF is vital. As a consequence, this inter-dependency of all parts of the Galactic system, including the contribution of CRs at lower rigidities, affects our interpretation of the GMF. In the end, our measurements of ultra-high energy CRs play an important role in constraining our magnetic field models, and combined analyses of all relevant parameters

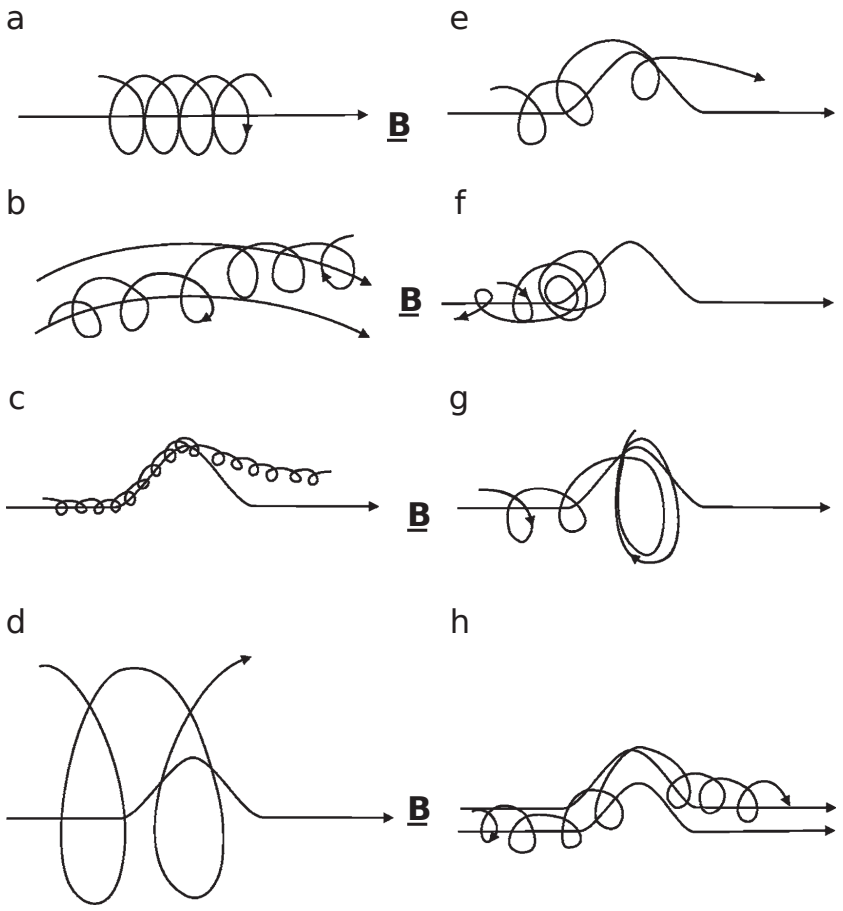

Figure 2.18: Illustration of different types of particle trajectories for various rigidity scales and magnetic field configurations [57].

seem to be the best way to gain a complete understanding the very same parameters [95, 96].

Mostly, however, UHECR astronomy profits more from a complete understanding of the GMF than vice versa, as information of the structure of extragalactic magnetic fields (through which particles with energies above 1 EeV are expected to traverse as they are most likely dominantly of extragalactic origin [59]), are more generally affected by the magneto-hydrodynamics of cosmological scales [96].

In the energy range of particles studied in the scope of this thesis, the large-scale component of the GMF plays the most important role in the deflection of CRs, though the turbulent components do affect the particles to significant degrees at lowest energies (or more precisely, rigidities). Especially the (local) strength of the turbulent fields will affect the motion of the particles at lowest rigidities, the scale at which turbulence takes over.

2.4 Liouville's Theorem

Liouville's theorem is commonly invoked in astroparticle physics to make inferences about the spectrum of CRs, more concretely, that the EGCR spectrum is conserved when traversing the GMF. The underlying assumption herein is that the GMF being static represents a conservative field. Liouville's theorem is typically employed in EGCR propagation in the GMF, to invoke the time reversibility of CR trajectories. This enables the quantification of EGCR deflection in the GMF via the Galactic lensing scheme (for more details, see chapter 5). However, there are caveats which involve collisions and scattering that may call the applicability of Liouville's theorem into question, particularly for small rigidities. In this section, we seek to give an overview of the relevant aspects, including a short derivation of Liouville's theorem, associated invariants, and conditions, under which these are broken, along with their implications. With this, we can more easily assess in later chapters whether we can invoke Liouville's theorem for EGCR propgation in the GMF across the entire rigidity range pertaining to the transition from GCRs to EGCRs.

2.4.1 Derivation of Liouville's Theorem

Liouville's theorem describes a continuity relation of the phase space density $f(\vec{x},\vec{p})$ of a system. In understanding the message of Liouville's theorem, it is useful to derive it in the classical case, before generalising it to the relativistic case.

Classical case

In classical physics, the phase space density is defined as the derivative of the phase space − the set of all possible positions and momenta[10] of a system − with respect to momentum and position, i.e. the density of points in phase space. Since the spectrum, the flux as a function of energy, is the observable we are dealing with in this context, we shall define our system as N independent particles each with their own positions and momenta. The phase space density becomes (see 2.19)

$$f(\vec{x},\vec{p}) = \frac{d^3n(\vec{x})}{d^3p} = \frac{d^6N}{d^3p\,d^3x} = \frac{dN}{dV}, \tag{2.19}$$

where $dV = d^3p\,d^3x$ is the volume element in phase space. The number of particles entering the projection of this volume in the k^{th} dimension $V_k = \prod_{i\neq k}^{3} dx_i\,dp_i$ equals (see equations 2.20 and 2.21)

$$\dot{N_k}^{in,x_k} = f(\vec{x},\vec{p})\,\dot{x_k}\,dp_k\,V_k, \tag{2.20}$$

in x_k direction and

$$\dot{N_k}^{in,p_k} = f(\vec{x},\vec{p})\,\dot{p_k}\,dx_k\,V_k, \tag{2.21}$$

in the p_k direction. Via Taylor expansion to the first order, the particles leaving V_k can be written as (see equation 2.22):

$$\begin{aligned}
\dot{N_k}^{out,p_k} &= \left(f(\vec{x},\vec{p})\,\dot{p_k} + \frac{\partial}{\partial p_k}(f(\vec{x},\vec{p})\,\dot{p_k})\right) dx_k\,V_k,\\
\dot{N_k}^{out,x_k} &= \left(f(\vec{x},\vec{p})\,\dot{x_k} + \frac{\partial}{\partial x_k}(f(\vec{x},\vec{p})\,\dot{x_k})\right) dp_k\,V_k.
\end{aligned} \tag{2.22}$$

Applying the same considerations to the other projections, we can write the partial derivative of the phase space density as a function of time as (see equation 2.23):

$$\begin{aligned}
\frac{\partial f(\vec{x},\vec{p})}{\partial t} &= \sum_{c=p,x}\sum_{i=1}^{3} \frac{d\left(\dot{N_k}^{in,c_k} - \dot{N_k}^{out,c_k}\right)}{dV}\\
&= -\sum_{i=1}^{3}\left(\frac{\partial}{\partial p_k}(f(\vec{x},\vec{p})\,\dot{p_k}) + \frac{\partial}{\partial x_k}(f(\vec{x},\vec{p})\,\dot{x_k})\right)\\
&= \nabla f(\vec{x},\vec{p}),
\end{aligned} \tag{2.23}$$

which has the form of a continuity equation. With the Hamilton equations, we have $\frac{\partial \dot{x_k}}{\partial x_k} = \frac{\partial^2 H}{\partial x_k\,\partial p_k} = -\frac{\partial \dot{p_k}}{\partial p_k}$, if the second partial derivatives are continuous, and we get (see equation 2.24):

$$\frac{d}{dt}f(\vec{x},\vec{p}) = \frac{\partial f(\vec{x},\vec{p})}{\partial t} + \sum_{i=1}^{3}\left(\frac{\partial f(\vec{x},\vec{p})}{\partial p_k} + \frac{\partial f(\vec{x},\vec{p})}{\partial x_k}\right) = 0. \tag{2.24}$$

The density of points remains constant; it is worth reiterating that the assumptions made here are that the change in flux is slow, such that we can approximate the flux of the outgoing particles via a Taylor expansion in the first order, and that the second partial derivatives are continuous so that we can exchange their order. In other words, Liouville's theorem describes a consequence of continuous motion of particles of a system, namely that the phase space density is conserved. The consequences when these conditions are not met, i.e. in the case of discontinuities, such as collisions and scattering, will be discussed later in chapter 4 for the explicit case of UHECR transport in the GMF.

[10] More generally, we speak of an f-dimensional (number of degrees of freedom) system with f generalised coordinates $q_1,...,q_f$, called configuration space, and momenta $p_1,...,p_f$, called momentum space, spanning a $2f$-dimensional carthesian space. In our case, $f = 3$ is sufficient, where $q_i \to x_i$ are the three spatial coordinates.

Relativistic case

In the case of UHECRs, particle velocities are ultra-relativistic, implying that one needs a generalised formulation of Liouville's theorem. The reformulation of Liouville's theorem is done via a generalisation of the phase space density as a Lorentz scalar. This is non-trivial since all particles are traveling in their respective proper frames with proper velocities, momenta and positions, each in different directions. In fact, one cannot even guarantee that the system is stationary, most straightforwardly due to the fact that assigning initial conditions to the entire system is not possible in relativity, or rather only for a small collection of particles or for sufficiently small volumes.

Instead, one has to explicitly require stationarity, i.e. assume that the momenta of the particles are statistically distributed. In such a case, we can define a common proper frame. This is achieved by smoothing out the phase space volume to a finite volume, in which an initial state can be defined. The volume can then be Lorentz transformed from the particle's proper frame to the observer frame yielding the following transformation (see equation 2.25)

$$d^3x' = \gamma\, d^3x, \tag{2.25}$$

where the primed frame is that of the particle. For the momentum transformation, the relation between the energy of a particle and its momentum $E = pc = \gamma\, m\, c^2$, where m is the particle's mass, and c is the speed of light, is utilised, revealing the transformation (see equation 2.26):

$$\frac{d^3p'}{\gamma'\, m\, c} = \frac{d^3p}{\gamma\, m\, c}. \tag{2.26}$$

Since $\gamma' = 1$ in the proper frame, the transformation of the phase space volume becomes (see equation 2.27)

$$d^3x\, d^3p = \frac{d^3x'}{\gamma} \cdot d^3p\, \gamma = d^3x'\, d^3p', \tag{2.27}$$

making it Lorentz invariant. This fact holds for each particle separately, and the single-particle distribution can be expressed (see equation 2.28):

$$f(\vec{x}, \vec{p})\, d^3x\, d^3p = f(\vec{x'}, \vec{p'})\, d^3x'\, d^3p'. \tag{2.28}$$

When adding up all particle distributions, the fact that the frames are not aligned, as was assumed in the case of a single particle, requires the introduction of a solid angle and its distribution for each particle. Since we assume collisionless motion, the phase space volumes do not overlap, and the individual distributions can be added up to define the total distribution. The angular distribution must be introduced ad hoc, which can mostly only be guessed. In our case, where we assume isotropic angular distributions, integration over the phase space just yields a factor of $4\,\pi$.

2.4.2 Adiabatic invariants

Adiabatic invariants are one-dimensional quantities that are conserved under slow motions, i.e. when Liouville's theorem holds. In such a case, the integral

$$I = \oint p\, dq$$

is conserved. When considering the motion of a particle in a weakly inhomogeneous magnetic field $\vec{B}$, the change in motion only occurs in the plane perpendicular to the magnetic field, the Larmor orbit (see equation 2.29):

$$I = \int \vec{P_\perp}\, d\vec{q}, \tag{2.29}$$

where $\vec{q} = \vec{r_\mathrm{L}}$ defines the coordinates in the plane of the Larmor orbit, $r_\mathrm{L} = |\vec{r_\mathrm{L}}|$ being the Larmor radius, and $\vec{P} = \vec{p} + {}^{e}/_{c}\,\vec{A}$ the generalised momentum in an electromagnetic field with the vector potential A such that $\vec{B} = \nabla \times \vec{A}$. Using Stokes' theorem and the relation $r_\mathrm{L} = {}^{c\,p_\perp}/_{e\,B}$, the integral yields (see equation 2.30):

$$\begin{aligned} I &= \frac{\pi\, c\, p_\perp^2}{e\, B} \\ \Rightarrow \frac{p_\perp^2}{B} &= \text{const.} \end{aligned} \tag{2.30}$$

The fraction $p_\perp^2/B$ is called the first adiabatic invariant. The interpretation of this quantity differs for the classical and relativistic case. In classical motion, it is most useful to consider the magnetic moment of the particle $\mu = K_\perp/B = p_\perp^2/2m\,B$. If the dynamics are relativistic, the magnetic moment is not conserved. Instead, it is the flux the surface enclosed by the Larmor orbit $\Phi = B \cdot \pi\, r_\mathrm{L}^2 = \pi\, c^2\, p_\perp^2/e^2\, B$ that is conserved.

2.4.3 Implications on the cosmic ray flux

Before we discuss associated invariants of Liouville's theorem, we can first write down its implications on the propagation of CRs, namely for the particle flux ϕ at any point $\vec{x}$:

$$f(\vec{x},\vec{p}) = \frac{d^3n(\vec{x})}{d^3p} = \frac{d^6N}{d^3p\,d^3x} = \frac{d^6N(\vec{x})}{p^2dp\,d\Omega\,dl\,dA} = \frac{1}{p^2}\frac{d^6N(\vec{x})}{dE\,d\Omega\,dt\,dA} = \frac{1}{p^2}\,\phi(\vec{x}), \tag{2.31}$$

where the following relations were utilised: $d^3p = p^2dp\,d\Omega = p^2 dE/\beta\,c\,d\Omega$, where Ω is the solid angle around $\vec{x}$, and $d^3x = dl\,dA = \beta\,c\,dt\,dA$, where $dl = \beta\,c\,dt$ is the path element along the CRs trajectory and dA is the unit area perpendicular to the trajectory. The flux is also conserved during continuous motion.

Chapter 3

Simulation tool – CRPropa 3

The analysis of the propagation effects is carried out via simulation with the help of the Monte Carlo-based cosmic ray propagation software CRPropa 3 [103]. Monte Carlo-based numerical studies can be viewed as complementary to analytical studies which are typically employed in the context of GCRs. The central enhancement to its predecessor, CRPropa 2 [106], is its modular structure, i.e. various parts of the simulation each have their separate modules, which can be combined to suit the user's needs. The modules operate by modifying so-called objects of the main cosmic ray *candidate* class, which contains all the information about the particle state or properties, as well as about the simulation itself (e.g. whether it is active). The different modules include (see also figure 3.1):

- *boundary modules*; they deactivate the candidate (i.e. stop the simulation) if a boundary condition is met,
- *source modules*; they create new candidates and inject them into the simulation,
- *interaction modules*; they take care of interactions (e.g. photo-nuclear interactions or radioactive decay),
- *deflection modules*; alter the candidate's position (according to the equation of motion or transport equation),
- *observer modules*; they are responsible for particle detection if a certain condition is met (e.g. crossing some boundary or shell).
- *output modules*; they store the simulation results to a (text- or hdf-)file.

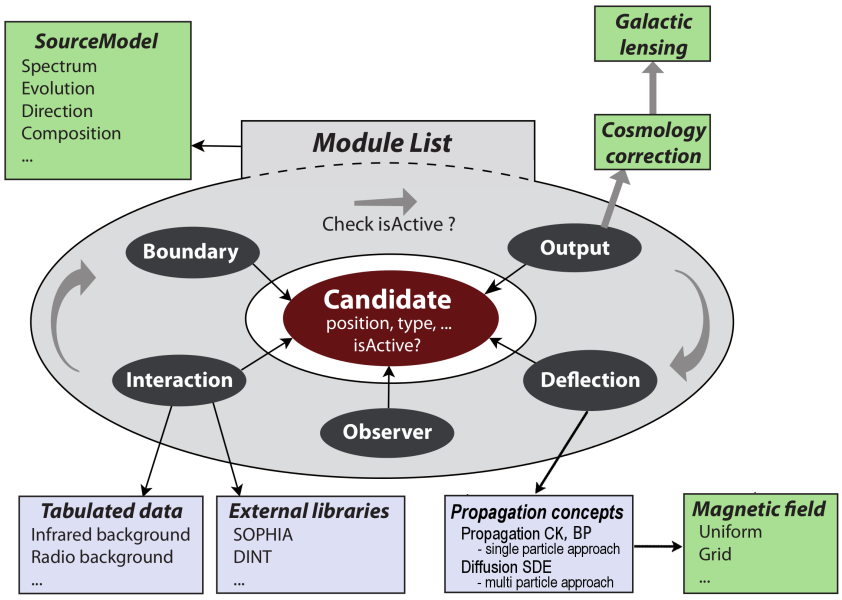

Figure 3.1: Modular structure of CRPropa 3 (adapted from [107]).

In principle, additional modules can be included to customise the simulation further. To elaborate on the aforementioned list, the simulation runs via updating the candidate's properties in each step of the propagation by the so-called `ModuleList` until breaking conditions set by the user in the boundary module are met (such as the trajectory length having surpassed a maximum value, or a particle leaving a specified propagation volume). The results are then saved via the observer module to a file, typically text or hdf. Candidates are either created by the user independently, or via the source module class which contains information on the source properties, such as particle types, spectrum, composition. The different modules each contain a multitude of possibilities for simulating cosmic rays, including the entire set of atomic nuclei up to (anti-)iron in the source modules, (photonuclear) interaction models in background fields in the interaction modules (that are not relevant for this research), and several magnetic field models in the deflection modules. There are also possibilities to construct and include custom models. Further details on the implemented modules are found in [108].

While CRPropa 3 is written in C++, it is interfaced to Python with the help of SWIG. With the help the SWIG interface, extensions to CRPropa 3, such as custom simulation modules, can be implemented directly from the Python script [103]. Example codes in a Python shell will be provided in this chapter to show the relevant modules utilised for the simulation studies described in this thesis. They will be introduced in the order a script is recommended to run by CRPropa 3 developers: Propagator → Interactions → Break conditions → Observer / Output [109].

Since the release of CRPropa 3.1 [107], both ballistic and diffusive propagation algorithms are available for the deflection modules. In ballistic propagation algorithms, the equation of motion of a charged particle in a magnetic field is solved (see equation 3.1).

$$\ddot{\vec{r}} = \frac{q}{E/c^2}\left(\vec{v} \times \vec{B}\right), \tag{3.1}$$

where $\vec{r}$ is the particle's position, q its charge, E its energy $\vec{v}$ its velocity, and $\vec{B}$ the local magnetic flux density [4]. They classify as single-particle approaches as trajectories of individual particles are calculated. This allows for the study of small-scale effects, such as anisotropy studies. No assumptions about the diffusion tensors of the magnetic fields have to be made and arbitrary field configurations can be chosen, which makes them more fundamental [107]. Ballistic propagation is particularly well suited for high rigidities, where the particle's gyro radius is large compared to the length scale of its environment (further details on the gyro radius can be found in section 3.2). However, as the gyro radius decreases, computation time becomes exceedingly high. In addition, for the description of diffusive propagation, the accuracy of ballistic approach is limited by the size of the propagation grid, that is set by the spacing of the grid of the turbulent magnetic field. For cases where the turbulent component of the magnetic field is dominant, or when the gyro radius is small, diffusive propagation algorithms that solve the transport equation (see 2.1.4) are better suited. They are useful to derive global aspects of CR propagation, such as leakage or steepening of CR spectra [110]. Especially noteworthy about the diffusive propagation algorithm implemented in CRPropa 3 is the differing approach to solving the transport equation compared to other codes used in the field. Instead of discretising the transport equation, it is transformed into a set of stochastic differential equations (SDEs). This is possible as the transport equation is special form of a Fokker-Planck partial differential equations to which SDEs are equivalent [111]. Further details on the implementation may be found in [107].

In the context of this thesis, it is worth noting that the "shin" region of the CR energy spectrum constitutes the energy range where propagation regime changes from diffusive to ballistic. With CRPropa uniquely having implemented both approaches, the treatment of the "shin" region as a combination of Galactic and extragalactic contributions is possible for the first time. For this purpose, both propagation algorithms need to be applied to this energy range. Especially for rigidities below $\approx 10^{17}$ V, where computation time starts to become an issue for ballistic propagation, a comparison between types of propagation algorithms is in order. Not only can the consistency between the two approaches be checked, but the rigidity, at which either approach is most suitable can be identified.

3.1 Relevant modules for Galactic propagation

The modular structure of CRPropa 3 allows for a customisation of simulations to many different use cases. In the following, the ones that are relevant for the studies in this thesis will be discussed further. There a wide variety magnetic field models implemented, including GMF models. They include the JF12 [100, 102][1], Pshirkov11 [112], and the TF17 [113] models. The JF12 field will be used for all simulation studies as it is still one of the currently most widely used. It is defined within a 20 kpc sphere around the GC (with the Earth located at $x = -8.5$ kpc[2]), which will also define the extent of the Galaxy, and henceforth referred to as the Galactic volume. This part as well as the very beginning of the basic simulation setup is shown in listing 3.1.

[1] There are additional implementations of this field with specific modifications.
[2] In Galactic coordinates, the x-axis represents the line connecting the GC with Earth.

```
from crpropa import *

sim = ModuleList() # Create simulation as a sequence of modules

B = JF12Field() # Define magnetic field: JF12 field
seed = 7 # Define random seed for the striated and turbulent components of the JF12
     field; in our studies, seed is actually rethrown for each particle
B.randomStriated(seed) # Include striated component of JF12 field
B.randomTurbulent(seed) # Include turbulent component of JF12 field

...
```

Listing 3.1: Simulation setup 1: The `ModuleList` and magnetic field

Since we are also propagating CRs up to post-"ankle" energies, and want to identify modifications of observables such as anisotropy, ballistic propagation best suits our needs. CRPropa hast two algorithms implemented that solved the equation of motion. The first and longest implemented is the Cash-Karp method [114], a Runge-Kutta type algorithm that solves ordinary differential equations (ODEs). Its accuracy is high when the gyro radius is large, such has highest-energy EGCRs. This algorithm does not automatically conserve momentum (and energy) during propagation. Rather, CRPropa explicitly enforces it. For this reason and due to numerical deviations of the direction of the momentum, an alternative algorithm was added to CRPropa 3.2 [115] that does so globally per construction, the Boris Push algorithm [116]. It is widely employed in plasma physics due to its speed and accuracy [115]. It is particularly well suited for longer simulations and phase-averaged approaches[3]. Despite it being the preferable choice for the studying particularly the low- to intermediate-energy part of the "shin" region, its implementation into CRPropa 3 occurred at a time when a significant portion of the simulations had been carried out already, that were performed with the Cash-Karp algorithm. Therefore the remainder of the simulation were done with the same algorithm. A detailed comparison of these two algorithms may be found in [117]. The implementation of the propagator into the simulation script is found in listing 3.2 (for the discussion of the choice of minStep, see section 3.2).

```
...

sim.add(PropagationCK(B, double tolerance = 1e-5, minStep = 0.01 * pc, maxStep = 1.
     * kpc)) # Define the propagator

sim.add(SphericalBoundary(Vector3d(0., 0., 0.), 20. * kpc)) # Break condition 1:
    Particle leaves Galactic sphere/shell
sim.add(MaximumTrajectoryLength(1000 * Mpc)) # Break condition 2: Particle
    trajectory length exceeds 1 Gpc

...
```

Listing 3.2: Simulation setup 2: The propagator and the break conditions

In the context of ballistic propagation, one challenge is worth mentioning. Due to the small actual observer size with respect to the distance of the observer to the source, particularly for EGCRs, tracking a particle from the source to the observer is very inefficient, i.e. a large number of particles have to be simulate to gain acceptable statistics. For context, one typically quoted number is 10^{-33}, which is efficiency with which particles that are emitted at a distance of 1 Mpc to hit an observer the size of Earth. Increasing the observer size to improve statistics can quickly give rise to artefacts that stem from its finite extent. In the context of the propagation of EGCRs in the GMF, an alternative approach is often utilised. Instead of propagating particles from their source to an observer (forward tracking), anti-particles are *backward tracked* from the observer position to the source and subsequently inverting the directions. Backward tracking relies on the time-reversibility of trajectories. CRPropa 3 even includes a Galactic lensing scheme adopted from the PARSEC software [118] that calculates the deflections in the GMF with the help of a matrix connecting injection directions of EGCRs to arrival directions at Earth acquired via backward tracking numerous particles from Earth's position to the edge of the Galaxy.

3.2 Simulation setup

All analyses have common setups that are best summarised before discussing them in any detail.

General considerations

Since the propagation effects we wish to investigate are consequences of deflections in the GMF, all arising effects are only rigidity-dependent. This allows for the use of a single nuclear species for our analysis, in

[3] The latter caveat addresses the fact that the Push Boris algorithm does not conserve the phase of gyration.

our case hydrogen nuclei, or protons[4]. Therefore, energy and rigidity may be used interchangeably in the course of this thesis, though we will attempt to stick to referring to rigidities. Another simplification made in this thesis, is to include no interactions. On the one hand, this is owed to the fact that CRPropa 3 does not contain any gas distribution models in the Galaxy, nor nuclear-nuclear interaction models; on the other hand, the lack of interactions is a valid assumption for most particle rigidities that we study[5], and thus focusing on the effects due to deflection alone is sufficient as a first step. Other sources of energy loss, such as synchrotron radiation, that may accumulate after large trajectory lengths, are also omitted for the sake of simplicity. They are also expected to be of negligible contribution, especially for high particle rigidities, where deflections and propagation times are small.

The main objective of this work is to identify and quantify propagation effects of GCRs and EGCRs in the GMF and to investigate how they modify observables, such as flux, composition and arrival direction. For this purpose, the forward tracking approach is best suited despite being computationally expensive compared to backward tracking. For one, backward-tracking studies cannot be employed for GCRs. This is because their sources are located in the GP, which GCRs will cross numerous times during propagation, and hence sources cannot be disentagled from mere crossings of the GP. In addition, forward-tracking studies are necessary for investigating the change of EGCR densities in the Galaxy. They also serve to confirm whether Liouville's theorem can be invoked across the entire rigidity range. On the one hand, the applicability of Liouville's theorem has implications on the relative relation between certain propagation effects that the GMF imposes on EGCRs, namely that their shielding from and confinement in the GP exactly cancel, which is worth confirming in its own right. On the other hand, Liouville's theorem predicts time-reversibility of CR trajectories, which is a requirement for later studies of anisotropic injection of EGCRs via the Galactic lensing scheme.

For the forward-tracking studies, the choice of source distributions is to be subject to the least assumptions. Therefore, for EGCRs, we mimic an isotropic flux via a uniform source distribution along the shell centered at the GC with a Lambertian injection direction. For GCRs, we opted for a homogeneous distribution in the GP, which is parameterised via a disk with a radius of 20 kpc centered at the GC. We remove sources are all located at a distance closer than 0.5 kpc from Earth's position. This is done to avoid the creation of GCRs inside the observer sphere, and to avoid artefacts arising from nearby sources. Via reweighting, alternative (continuous) source distributions can easily be studied with the results found herein. The effect of discrete source distributions, especially in the context of GCRs, would have to be studied with new dedicated simulations.

We use two types of observers for our studies. The most intuitive choice of the observer is Earth, with which we seek to investigate the modifications of CR observable due to propagation in the GMF. Earth is parameterised via an observer sphere centered at Earth's location in the Galaxy. Particles are collected that cross the shell of the observer sphere. The radius of the sphere is varied between $5, 10, 50, 100, 500, 1000$ pc in order to identify artefacts stemming from the nonzero observer size. For the identification and quantification of the propagation effects, we use the GP as an observer. For this purpose, the spatial extent of the GP is that of a cylinder centered at the GC with a height of 100 pc. For GCRs, the radius of the GP is the same as for the source, 20 kpc. In the case of EGCRs, a variable radius is chosen. The choice of a variable cylinder radius is relevant for EGCRs rays due to the discontinuous drop-off of the GMF at the edge of the Galaxy. This discontinuity hardly affects the particle trajectories for large particle rigidities or at higher Galactic latitudes, where the field is already so weak that the discontinuity becomes negligible. At low Galactic latitudes, particles of lower rigidity penetrate further into the Galaxy than they would if there was a continuous drop-off of the field beyond the edge of the Galaxy. This introduces a source of systematic bias if the GP observer reached to the edge of the Galaxy. The surplus particles are eventually reflected back outside the Galaxy as the field strength increases. By varying the radius, we effectively perform a fiducial cut to recover the behaviour which would occur for a continuous drop-off of the GMF. To illustrate the aforementioned effect, we calculate the effective number of particles (i.e. total number divided by the area of the disk, which is conserved in case of no deflection, let alone shielding) within the disk. Since the effect we wish to minimise is most pronounced for lowest rigidities, we split the data up into multiple rigidity sections of equal size. Figure 3.2 depicts the effective number of particles reaching the GP as a function of cylinder radius.

We see that, for the lowest rigidity bin (red line), the weighted number of particles drops steeply as we go below a cylinder radius of 20 kpc, such that for a radius of ≈ 19 kpc, the effect already vanishes. The minimal value across all rigidity bands is roughly at the distance of Earth to the GC. For lower radii, it appears as though there is a slight increase in the weighted number of particles towards small radii, which is more pronounced the smaller the rigidity. This may be an indication of a concentration towards the GC.

For all cases where multiple rigidities are investigated, an R^{-1} power law spectrum is used[6]. The rigidity

[4] The effects of the GMF on heavier nuclei can be ascertained by scaling the energy by the charge number Z of the nucleus.

[5] A back-of-the-envelope estimate of the mean free path of a CR proton with an energy of 1 PeV, is $\lambda = {}^1\!/_{n \cdot \sigma} \approx {}^1\!/_{1\, cm^{-3} \cdot 10^{-25}\, cm^2} \approx$ a few Mpc, which correspond to a propagation time of ≈ 10 Myr.

[6] It is commonplace to employ logarithmic energy binning in the analysis of CR data; in such a binning, an R^{-1} spectrum appears flat, i.e. all rigidity bins have the same number of entries, which makes possible modifications in

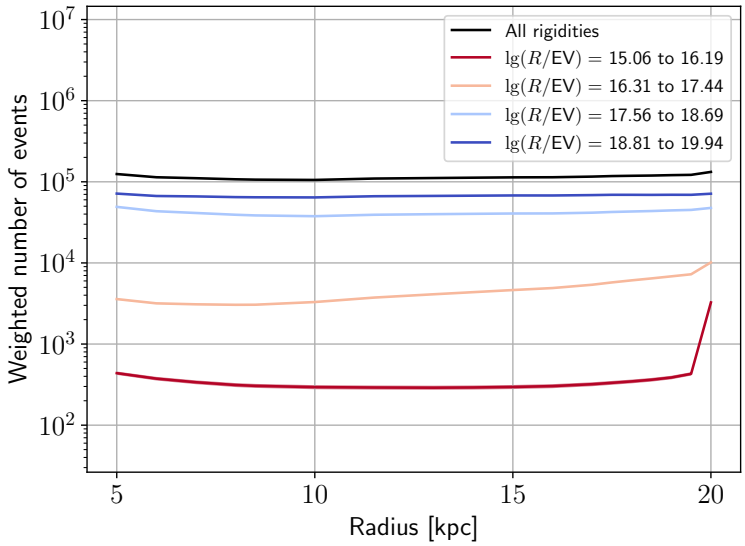

Figure 3.2: The weighted number of particles reaching the GP (i.e. w.r.t. the expected number from geometric considerations) as a function of GP cylinder radius for four equidistant rigidity bins (in logarithmic binning) signified in the legend.

range spans from 10^{16} V to 10^{20} V, as this was the widest rigidity range that was still computationally feasible with available resources. In some cases, the minimum rigidity is decreased to 10^{15} V whenever the studies allowed for it. The manual definition of each source and observers, as well as the output, is found in listings 3.3 to 3.6.

```
...

## If the observer is Earth, output file and the observer are defined via existing modules
out = TextOutput('example.txt')
out.disableAll() # Clear all information that may be added to output file and explicitly name desired information
out.enable(Output.TrajectoryLengthColumn)
out.enable(Output.CreatedPositionColumn)
out.enable(Output.CreatedDirectionColumn)
out.enable(Output.CurrentPositionColumn)
out.enable(Output.CurrentDirectionColumn)
out.enable(Output.CurrentEnergyColumn)

obs = Observer()
obs.add(ObserverLargeSphere(Vector3d(-8.5, 0., 0.) * kpc, 1. * kpc)) # Define Earth as a shell of radius 1 kpc centered at the position (-8.5,0,0) in Galactic coordinates
obs.onDetection(out) # Pass particle information on to output if detected
obs.setDeactivateOnDetection(False) # Don't stop simulation once observed (this way, smaller observer spheres can be included in the same simulation)
sim.add(obs)

...
```

Listing 3.3: Simulation setup 3a: observer and output for Earth

```
...

class MyTrajectoryOutput(Module): # For studies where the GP is the observer, observer and output modules are combined in one custom module. For each particle, it is checked whether its z-coordinate lies between -50 pc and 50 pc (= width of GP). The last instance that this is fulfilled is stored to the output file. The particle information that is stored is energy, trajectory length, and minimum distance from GP
  def __init__(self, fname):
```

the spectrum visually discernible.

```
    Module.__init__(self)
    self.fout = open(fname, 'w')
    self.fout.write('Energy\tTrajectory length\tMinimum dist to GC\n')
    self.RMin = 20. # Define auxiliary variable to retrieve minimum distance
    self.BoolInPlane = 0 # Define auxiliary variable to flag particles that cross
    GP
  def process(self, c):
    v = c.current.getPosition()
    ev = c.current.getEnergy()
    e = ev / EeV
    r = c.getTrajectoryLength() / kpc
    x = v.x / kpc
    y = v.y / kpc
    z = v.z / kpc
    R = np.sqrt(x**2. + y**2.) # Distance to GC
    if c.isActive():
      self.step += 1
      if abs(z) < 0.05:
        self.BoolInPlane = 1
        if (x**2. + y**2.) <= self.RMin**2.:
          self.RMin = R
    if not(c.isActive()):
      if self.BoolInPlane == 1:
        self.fout.write('%.6E\t%.4E\t%.3E\n'%(e, r, self.RMin))
      ## Reset auxiliary variables
      self.BoolInPlane = 0
      self.RMin = 20.
  def close(self):
    self.fout.close()
```

Listing 3.4: Simulation setup 3b: observer and output for GP

```
...
def PowerLawSpectrum(x,y,z,index): # Transforms uniform distribution between 0 and
    1 into a power law distribution
  Emin = 10**y
  Emax = 10**z
  if index == -1.:
    f = Emin * (Emax / Emin) ** x
  else:
    f = (x * (Emax**(index+1)-Emin**(index+1))+Emin**(index+1))**(1/(index+1))
  return f

Nsim = ... # Number of simulated particles
for k in range(Nsim):
  ## Define particle energy according to power law distribution
  ene = np.random.uniform(low=0., high=1.)
  energy = PowerLawSpectrum(ene,16.,20., -1.) * eV
  ## Define injection position via uniform distribution along 20 kpc disk centered
    at the GC
  While True: # While loop to ensure that GCRs are create outside the 0.5 kpc
    circle around Earth
    rSqPos = rnd.uniform(0.,400.)
    rPos = np.sqrt(rSqpos)
    lonPos = rnd.uniform(-math.pi,math.pi)
    xPos = rPos * np.cos(lonPos)
    yPos = rPos * np.sin(lonPos)
    if np.sqrt(xPos+8.5)**2.+yPos**2.) > 0.5:
      break
  zPos = 0.
  position = Vector3d(xPos, yPos, zPos) * kpc
  ## Define injection direction
  muDir = rnd.uniform(-1,1)
  latDir = np.arccos(-muDir)
  lonDir = rnd.uniform(-np.pi,np.pi)
  direction = Vector3d()
  direction.setRThetaPhi(1, latDir, lonDir)
  pid = nucleusId(1,1)  # Nucleus ID of proton
  p = ParticleState(pid, energy, position, direction, ) # Define particle state
  c = Candidate(p) # Define candidate
  sim.run(c) # Run simulation of candidate
```

Listing 3.5: Simulation setup 4a: the GP source

```
...
## For isotropically injected EGCRs, we use an implemented source distribution,
    namely SourceLambertDistributionOnSphere
center, radius, inward = Vector3d(0., 0., 0.), 20 * kpc, True # Define the central
    point and radius of the injection sphere, and the injection direction range (
    inward or outward)
source.add(SourceLambertDistributionOnSphere(center, radius, inward))
source.add(SourceParticleType(nucleusId(1, 1)))
source.add(SourcePowerLawSpectrum(10.**16. * eV, 10.**20. * eV, -1.))
sim.run(source, Nsim) # run simulation
output.close()
```

Listing 3.6: Simulation setup 4b: the isotropic EGCR source

Technical considerations

When performing simulations, it is important to ensure that any effects that one infers are not artefacts of a poor choice of technical parameters. One obvious potential pitfall is the choice of the simulation step sizes, as step sizes exceeding the length scales of the deflection distort the particle's trajectory and lead to systematic bias.

However, decreasing the step sizes comes at the cost of simulation speed. While the Cash-Karp algorithm allows for a range of step sizes depending on the length scale of deflection, the minimal step size has to be chosen optimally as to minimise simulation time. A suitable conception of the length scale of the deflection is the gyro radius r_g of the particle of rigidity R in the magnetic field of $\vec{B}$:

$$r_{\mathrm{g}} = \frac{R\, v_\perp}{c^2\, B} \tag{3.2}$$

$$r_{\mathrm{g}}[\mathrm{pc}] \approx 11 \cdot \frac{R\,[\mathrm{PV}] \cdot v_\perp/c}{B\,[\mu\mathrm{G}]}, \tag{3.3}$$

where $B = |\vec{B}|$ is the magnitude of the magnetic field, and $v_\perp = c \cdot \sin \sphericalangle(\vec{v}, \vec{B})$, is the perpendicular component of the particle's velocity $\vec{v} = c\vec{e_v}$ with respect to the magnetic field at its current location. The minimal step size is chosen to be smaller than a tenth of the minimum gyro radius $r_{\mathrm{g,min}} = r_{\mathrm{g}}(R = R_{\mathrm{min}}, v_\perp = c, B = B_{\mathrm{max}})$ with B_{max} signifying the maximum magnitude of the magnetic field in the Galactic volume[7]. $r_{\mathrm{g,min}}$ is estimated using the x-z cross section at $y = 0$ in Galactic coordinates of the gyro radius for $v_\perp = c$ of a PV-rigidity particle in the GMF, which is depicted in figure 3.3 for several length scales. The corresponding cross section of the magnitude GMF flux density is depicted in figure A1.

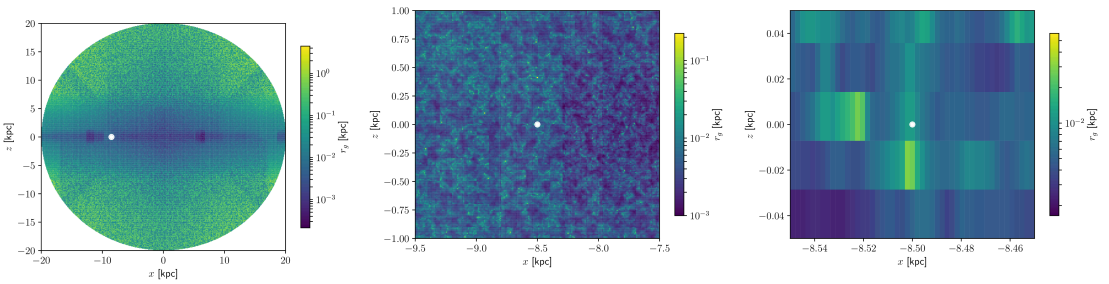

(a) Entire Galactic extent in x and z. **(b)** ± 1 kpc section in x and z around Earth. **(c)** ± 50 pc section in x and z around Earth.

Figure 3.3: Sections of the x-z cross section at $y = 0$ in Galactic coordinates of the minimum gyro radius (i.e. for $v_\perp = c$) of a 1 PV particle in the Galaxy; white dot signifies location of Earth. The spiral arm structure of the JF12 field is visible in the dark blue areas in the GP of the left map.

Assuming that this cross section is typical for the entire Galaxy, we can infer from it that the minimum gyro radius does not go below 10^{-4} kpc $= 0.1$ pc. Hence, a sensible minimum step size of a simulation can be set to 0.01 pc, such that the distance between two steps is always smaller than any gyration. We further scrutinise this choice by explicitly testing the effect of the step size on the precision. This we do

[7] At first glance, the choice of $v_\perp = c$ to calculate the smallest value of the gyro radius seems counterintuitive, as any value $v_\perp < c$ would yield a smaller value for r_{g}; however, a particle experiences the largest deflection when it is fully perpendicular to the magnetic field. Therefore, the minimum gyro radius is to be viewed as an estimate of the length scale of the strongest deflection of a particle with rigidity R_{min} and B_{max}.

by backward tracking 10^4 anti-protons injected isotropically from Earth's position with an R^{-1} spectrum in the rigidity range of $\left[10^{16}\,\mathrm{V}, 10^{20}\,\mathrm{V}\right)$ to the Galactic shell, i.e. the edge of the Galactic volume. For each simulation where we vary d_{min}, we simulate the same set of rigidities and injection directions. To parameterise the precision, we measure the difference in the exit angle and in the trajectory length at the Galactic shell with respect to the smallest tested step size of $d_{\mathrm{min}} = 10^{-7}\,\mathrm{pc}$, as well as the simulation time per particle and for all 10^4 particles. The median values of each quantity as a function of rigidity are depicted in figure 3.4. We find that the distribution of the angular deviation of the exit directions does not depend on the choice of d_{min} (see figure 3.4a). We generally find an increasing trend as rigidity decreases. Below $\sim 10^{18}\,\mathrm{V}$, the curve flattens off, approaching but not reaching $\pi/2$. This suggests that the exit directions become increasingly unrelated. This lack of dependence on the choice of d_{min} indicates that small deviations in the trajectories diverge as propagation continues, and the degree of this divergence depends primarily on the rigidity of the particle.

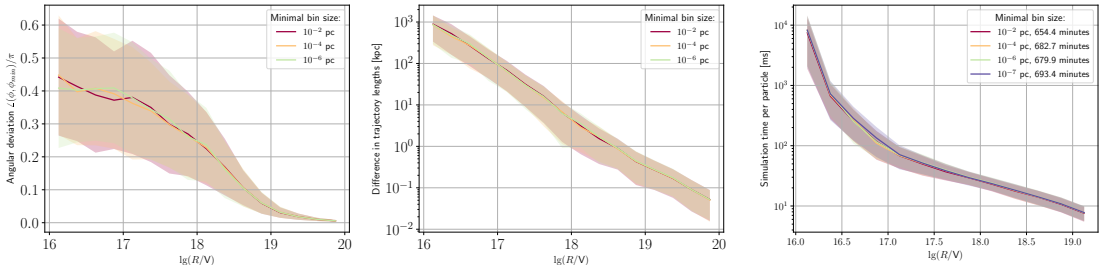

(a) Angle between exit directions from the Galactic volume w.r.t. $d_{\mathrm{min}} = 10^{-7}\,\mathrm{pc}$ for various values of d_{min} signified in legend.

(b) Absolute difference in trajectory lengths w.r.t. $d_{\mathrm{min}} = 10^{-7}\,\mathrm{pc}$ for various values of d_{min} signified in legend.

(c) Simulation time per particle for various values of d_{min}, which are signified in legend along with their total simulation times.

Figure 3.4: Effect of minimal step size d_{min} on precision. Three quantities are used to parameterise the change in precision (see captions of subfigures). All quantities are depicted as function of rigidity via their median values (with the spread quantified via the median absolute difference).

The difference in trajectory lengths also appears to lack any dependence on the choice of d_{min}, and also exhibits an increasing trend as rigidity decreases (see figure 3.4b). The median difference in trajectory lengths approaches 1 Mpc at the lowest rigidities, with no sign of convergence. This, too, suggests that the particles' trajectories are effectively unrelated at these rigidities.

Figure 3.4c shows that reductions of the minimal step size do not have a noticeable effect on the median simulation time per particle, with the trends following the same decreasing trend with rigidity for all choices of d_{min}. The total simulation time (indicated in the legend) does appear to increase slightly with decreasing step size. This is most likely due to the existence of a small number of outlier events among the simulated particles that increased the total simulation time. They consist of trapped particles that propagate in (quasi-)periodic trajectories within the Galactic volume. Such events are expected to occur more frequently for smaller simulation steps. Thus, if d_{min} is reduced further than necessary, such outliers can extend the total simulation time drastically, especially for the simulation of a very large number of events. As they affect only a small fraction of particle trajectories, avoiding their occurrence by fixing the choice of d_{min} will only have a negligible effect on the overall results of the simulation. In light of these results, our choice of $d_{\mathrm{min}} = 0.01\,\mathrm{pc}$ for all our simulations does not appear to lead to any noticeable systematic biases in our results, while, at the same time, reducing the occurrence of trapped particles.

A further way to avoid an increased total simulation time due to trapped particles is to terminate a particle's simulation when a maximal trajectory length of 1 Gpc is exceeded. In addition, the simulation of a particle is terminated if it leaves the Galactic volume, as such particles are not expected to return. Deflections outside the Galaxy in the significantly weaker intergalactic magnetic fields are expected to occur at significantly larger length scales than the extent of the Galactic volume.

A final consideration pertains to the increasing simulation time with decreasing particle energy. In some analyses, the simulations are carried out in multiple overlapping rigidity bands. This way, more particles can be simulated for higher energy bands with shorter simulations times per particle. The energy bands used are $I_{R,1} = \left[10^{15}\,\mathrm{eV}, 10^{16.5}\,\mathrm{eV}\right)$, $I_{R,2} = \left[10^{16}\,\mathrm{eV}, 10^{18.5}\,\mathrm{eV}\right)$ and $I_{R,3} = \left[10^{18}\,\mathrm{eV}, 10^{20}\,\mathrm{eV}\right)$.

Chapter 4

Investigation of Galactic propagation effects

As pointed out in chapter 2, the energy range of the "shin" region of the CR energy spectrum corresponds to a range of gyro radii that intersects typical length scales of the Galaxy (i.e. height and radius of the GP). The propagation regime transitions from ballistic (with small deflections) to diffusive (with large deflections and random motion) in the corresponding rigidity range. This set of facts is encapsulated in figure 4.1, which depicts the gyro radius as a function of rigidity around the "shin" region for different typical magnetic field strengths.

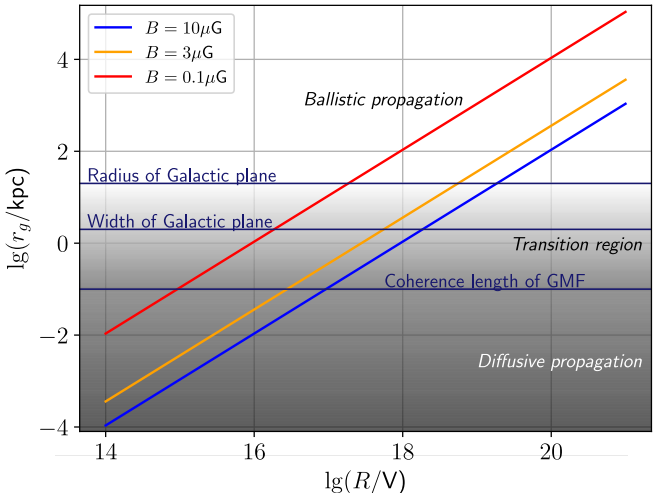

Figure 4.1: Dependence of the gyro radius on rigidity for typical GMF strengths, as signified in the legend; the horizontal lines indicate characteristic length scales of the Galaxy, i.e. the radius and width of the GP, as well as the approximate coherence length of the turbulent component of the GMF [102].

This chapter will outline how the change in propagation regimes in the "shin" region can plausibly lead to a range of rigidity-dependent propagation effects. We begin with establishing the change in propagation regimes via the distribution of deflection angles and trajectory lengths of GCRs and EGCRs that arrive at Earth (see section 4.1). Following this, we highlight one consequence of this change of propagation regimes that is relevant for the subsequent discussion of the expected propagation effects, namely the covered volume fraction (see section 4.2). We then discuss large-scale phenomenological features of both GCRs and EGCRs as a function of rigidity, and relate them to the change in propagation regimes. We attempt to combine these for GCRs and EGCRs individually via a "steady-state" approach (see section 4.3). In addition, we present one test of Liouville's theorem, namely the rigidity dependence of the first adiabatic invariant for EGCRs that reach the GP (see section 4.4). This last aspect serves to argue for the necessity to perform forward-tracking studies for the analysis of flux modifications of isotropically injected EGCRs due to propagation in the GMF. Only if time-reversibility is explicitly shown, can one apply the Galactic lensing approach[1] to the subsequent analysis of anisotropically injected EGCRs.

[1] In principle, a lens can also be constructed via forward tracking (see the procedure for lens creation in section 5.3.2 or [118]). However, the efficiency of forward tracking is so low, that such lenses typically have very high uncertainties.

4.1 Deflection angle and trajectory length distribution

The most pertinent propagation-related feature of the transition region is the shift in the propagation regimes from ballistic to diffusive as rigidity decreases. This we attempt to show via the strength of deflection of CRs propagating in the GMF as a function of rigidity. The quantities used to parameterise the deflection are the deflection angle, i.e. the difference between the injection direction at the source and the arrival direction at the observer, and the trajectory length from source to observer. The observer is chosen to be Earth. The radius of the corresponding observer sphere is chosen to be $r_{\text{obs}} = 0.05\,\text{kpc}$ — sufficiently small to minimise artefacts and sufficiently large to have enough statistics. We propagate $N = 3 \cdot 10^8$ GCR and $N = 5 \cdot 10^9$ EGCR protons. The injection spectrum follows an R^{-1} rigidity distribution in the from $10^{16}\,\text{eV}$ to $10^{20}\,\text{eV}$. In addition to the forward tracked EGCRs, we calculate the deflection angles for $N = 10^6$ anti-protons injected isotropically from the position of Earth and backward tracked to the edge of the Galaxy. This is done as check for artefacts due to the finite observer sphere size, on the one hand, and to test the time-reversibility of EGCR trajectories.

For EGCRs, we split the arrival directions at Earth into three arrival direction bands, roughly indicating whether they arrived from the north, south, or the GP, and plot the corresponding measured deflection angles for each band separately. This allows for some insight into the topology of the GMF, more accurately the "column density" of the magnetic field in each direction of the sky, assuming that most of the particles were injected from the same direction band as the one they arrived at the observer from.

The median deflection angle of GCRs as a function of rigidity is depicted in figure 4.2. For EGCRs, the median deflection angle of both forward tracked protons and backward tracked anti-protons are depicted in figure 4.3.

Two main features are visible in the (all-sky) deflection angle distribution as a function of rigidity:

- Up to a rigidity of $\gtrsim 1\,\text{EV}$, the median deflection angles is roughly constant at around $\pi/2$, characteristic of diffusive propagation.
- Above $\gtrsim 1\,\text{EV}$, the median deflection angle drops off rapidly to almost 0, indicating a transition to ballistic propagation.

The inflection point of $\gtrsim 1\,\text{EV}$ can be understood in the context of the corresponding gyro radius with respect to the size of the Galactic volume. Using equation 3.3, we get $r_{g,max}(\langle B\rangle = 3\,\mu\text{G}) \approx 10\,\text{kpc} = \mathcal{O}(r_{\text{gal}})$, where r_{gal} is the radius of the Galactic volume.

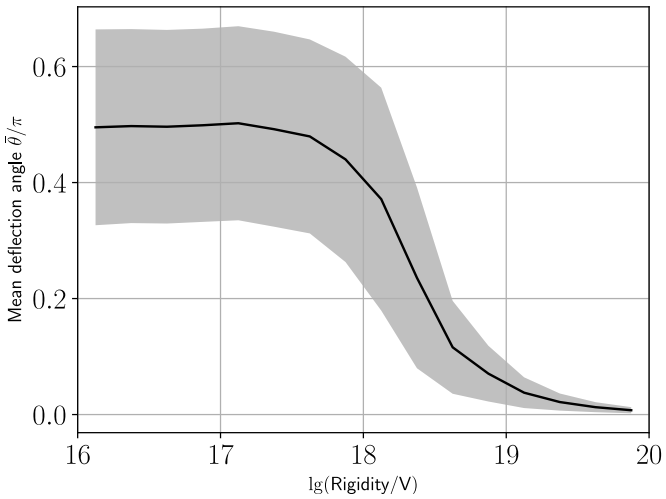

Figure 4.2: Median deflection angle of GCRs as a function rigidity. The spread is quantified via the median absolute difference.

When closing in on the arrival direction bands for EGCRs, further features are discernible. A clear north-south asymmetry in the deflection strength is visible in the case of forward tracked protons, as evidenced by larger deflections in intermediate rigidity ranges for particles arriving from the south, compared to the north. Strikingly, this gap seems to be closed at the lowest rigidities, indicating that the transitions of the propagation regimes with rigidity occurs more slowly for particles arriving from the north, or generally at different rates depending on the arrival direction. This feature is not visible in the backward tracked case, and should therefore be taken only tentatively[2].

[2] It is entirely plausible that there is an injection direction dependence on the median deflection of a particle, as

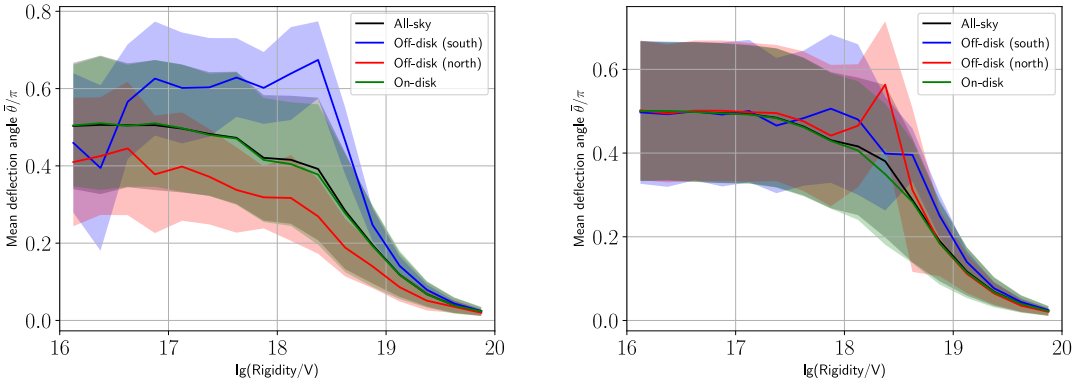

(a) Forward tracked protons from Galactic shell to observer sphere of $r_{\text{obs}} = 0.05\,\text{kpc}$.

(b) Backward tracked anti-protons from Earth's position to the the Galactic shell.

Figure 4.3: Median deflection angle of EGCRs as a function of rigidity. The spread is quantified via the median absolute difference. Furthermore, the deflection angle is depicted for different arrival direction bands, indicating whether the EGCRs arrived from the north (red line, $\theta = [20°, 90°]$), south (blue line, $\theta = [-90°, -20°]$), or the GP (green line, $\theta = [-20°, 20°]$), on top of the all-sky distribution (black line).

A further way to illustrate the change in propagation regimes is via the rigidity dependence of the trajectory length d_{traj}, which is proportional to the propagation time t_{prop} ($d_{\text{traj}} = t_{\text{prop}} \cdot c$, where c is the speed of light, the velocity with which CRs essentially propagate at these ultra-relativistic energies). As for the distribution of deflection angles, the trajectory length is measured for $N = 3 \cdot 10^8$ GCRs and $N = 5 \cdot 10^9$ EGCRs in the rigidity range of $\left[10^{16}\,\text{V}, 10^{20}\,\text{V}\right)$ with an R^{-1} spectrum that cross an observer sphere shell of radius $r_{\text{obs}} = 0.05\,\text{kpc}$. The distribution of d_{traj} is plotted in a 2D histogram, with the rigidity on the x-axis and d_{traj} on the y-axis. The trajectory length is also measured for backward tracked anti-protons injected isotropically at Earth's position that propagate to the edge of the Galaxy. The distribution of d_{traj} as a function of rigidity of GCRs is depicted in figure 4.4, and of forward as well as backward tracked EGCRs in figure 4.5.

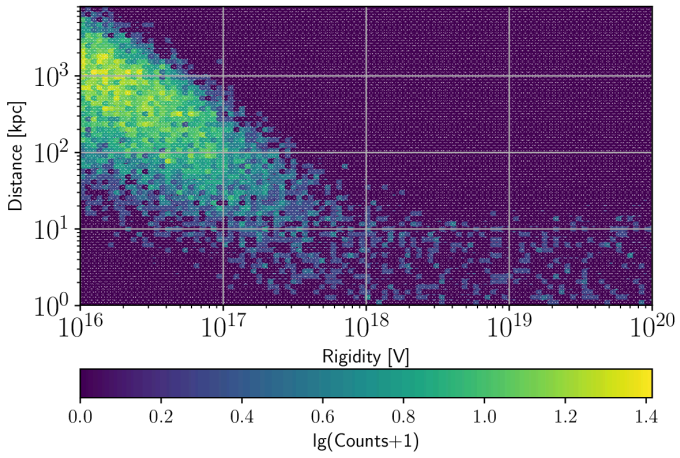

Figure 4.4: Trajectory length distribution as a 2D histogram of GCRs as a function of rigidity.

The trends for GCRs and EGCRs are very similar. The distribution can be split into two regimes in rigidity: At the highest rigidities, we see a flat trajectory length distribution with a small spread in the order

the cumulative field strength traversed during propagation depends on the injection direction, being strongest for injections from low Galactic latitiudes, closer to the GP. The difference in the angularly resolved deflection angle distributions between forward and backward tracked EGCRs may therefore reflect the finite size of the observer sphere which extends outside of the GP enough to capture the differing degrees of deflection angles depending on the injection direction. The correlation between the injection and arrival direction distributions may disappear as the observer approaches a point, as evidenced by the backward tracked deflection angle distribution.

of the spread from geometric considerations alone ($> 0.5\,\mathrm{kpc}$ for GCRs and $> (20 - 8.5)\,\mathrm{kpc} = 11.5\,\mathrm{kpc}$ for EGCRs) down to the inflection point $\gtrsim 1\,\mathrm{EV}$. Below this rigidity, the trajectory length increases. For both regimes, the relative spread − while larger for regime below the inflection point − scales with rigidity, such that it appears fairly constant. One discernible difference between GCRs and EGCRs is that the band of trajectory lengths is wider towards shorter values for GCRs across the entire lower rigidity regime, where the trajectory length decreases with rigidity. This is not surprising, as a bulk of GCR sources are closer to Earth than the edge of the Galactic volume. The minimum trajectory length per rigidity band nevertheless increases as rigidity decreases, because the particles are still significantly deflected during propagation to Earth even for close sources. This is mainly owed to the fact that they are injected into the GP where the field strength is largest and diffusive propagation sets in for higher rigidities than anywhere else in the Galaxy.

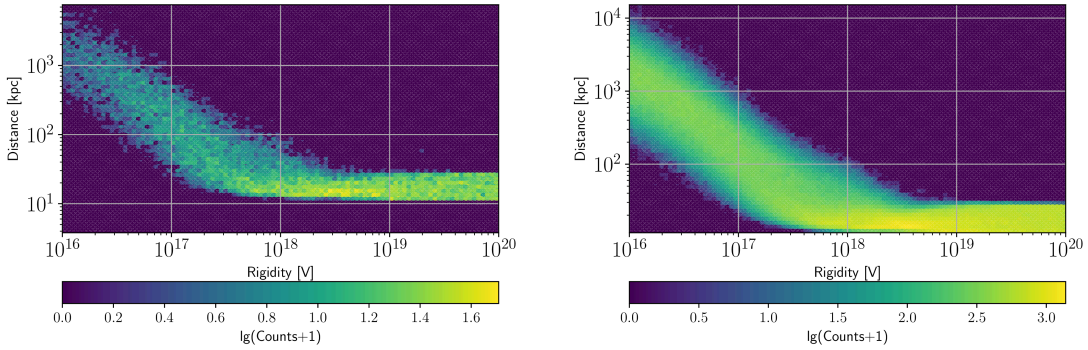

(a) Forward tracked protons from the Galactic shell to an observer sphere of radius 0.05 kpc around Earth.

(b) Backward tracked anti-protons from Earth's location to the edge of the Galactic volume.

Figure 4.5: Trajectory length distributions as 2D histograms of EGCRs as a function of rigidity.

4.2 Covered volume fraction

Having shown that the change in propagation regimes does indeed occur, the consequences of this are in need of discussion. One quantity, the covered volume fraction of a particle propagating within a given volume inside the Galaxy, is especially useful. This is because it illustrates one key difference between diffusive propagation has compared to ballistic propagation, namely the random motion, which is relevant for predicting the effects that propagation in the GMF imposes on CR observables. If particles begin to propagate diffusively, and do not merely gyrate around field lines anymore, the covered volume fraction should begin increase as rigidity decreases. Its dependence on rigidity should be similar to that of the trajectory length.

To quantify the covered volume fraction, the volume of a 1 kpc sphere around Earth is binned into $1\,\mathrm{pc}^3$ cubes, resulting in $n_V \approx {}^4\pi/_3\,1000^3 \approx 4.189 \cdot 10^9$. $N = 10^6$ anti-protons are injected from Earth to the edge of the sphere in the rigidity range of $\left[10^{16}\,\mathrm{V}, 10^{20}\,\mathrm{V}\right)$ with an R^{-1} spectrum, and the number of traversed cubes n_C is counted for each particle. The resulting volume fraction is then parameterised via the ratio $f_C = {}^{n_C}/_{n_V}$. The distribution of the covered volume fraction is depicted in figure 4.6 as a 2D histogram, with the rigidity on the x-axis and f_C on the y-axis. As expected, the trend of the covered volume fraction has a very similar trend to the trajectory length distribution in figure 4.5. Below an inflection point, the covered volume fraction increases with decreasing rigidity. Above it, the fraction is constant. This trend supports the notion that lower-rigidity particles do not merely gyrate around field lines as they are more strongly deflected by the GMF, but also traverse increasingly random trajectories. This implies that a decrease in rigidity increases the likelihood of a particle of reaching any given region within the GP, once it propagates therein.

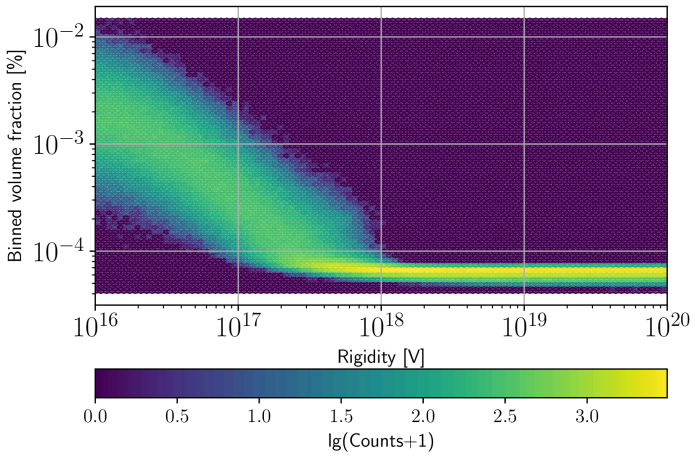

Figure 4.6: 2D histogram of volume fraction distribution of paths from Earth to the edge of 1 kpc sphere around Earth as a function of rigidity.

Unsurprisingly, the position of the inflection point is at a slightly smaller rigidity of $\sim$ 1EV compared to the trajectory length distribution. This is owed to the fact that the propagation takes place in a 1 kpc sphere, which is 20 times smaller than the radius of the Galactic volume. At the same time, the mean magnetic field strength in this volume, which is situated in the GP, is larger than for the rest of the Galaxy (at the scale of several or tens of μG as compared to 10–100nG; see also figure A1). The rigidity at which a particle has a gyro radius in the order of 1 kpc in a 10 μG field is 1 EV, consistent with the observed position of the inflection point.

For all observed quantities, we find an inflection rigidity of a few EV in their rigidity dependence. This corresponds to a gyro radius smaller than the radius of the Galaxy for μG field strengths, and even approaching the width of the GP for 10μG. Given that this value arises both for GCRs and EGCRs, we can reasonably infer that the rigidity dependence of the propagation features stem from the GMF topology in general. This is partly encapsulated in figure 4.1, where the relationship between rigidity and gyro radius, as well as typical Galactic length scales and propagation regimes, are depicted. How these features affect the propagation on large scales will be discussed in the following.

4.3 Large-scale propagation effects

The analysis of the rigidity dependence of deflection angles, trajectory lengths for both GCRs and EGCRs, as well as the covered volume fraction, reveal an inflection rigidity of $\gtrsim$ 1 EV, at which the most noticable change in propagation regimes occurs. Below this rigidity, the diffusive regime starts taking effect, where the median deflection angle is $\pi/2$, and the trajectory length and covered volume fraction both increase. How this change in propagation regimes affect the large-scale propagation of both GCRs and EGCRs will be discussed in this section.

The most important feature of the large-scale structure of the GMF are larger field strength in GP and halo region. This means that for certain rigidities, the nature of propagation of CRs alters from diffusive to ballistic depending on their location in the GMF (i.e. on- or off-plane). This is particularly relevant for EGCRs that originate from outside of the Galaxy and can propagate through all regions before reaching Earth. As they approach the GP, the increasingly strong fields deflect them ever more strongly, whereas EGCRs that propagate away from the GP experience increasingly weaker deflection. Therefore, if they are deflected such that they propagate away from the GP, they are less likely to be deflected back, effectively leading to a reflection by the GP. This is the so-called *shielding* effect. The increase of both the propagation time and covered volume fraction in the GP as rigidity decreases below a few EV indicates that diffusively propagating GCRs and EGCRs are increasingly *confined* in the GP (and probably even the halo region at the lowest rigidities). Both these effects can be qualitatively discerned by tracking the particles' trajectories during propagation in the Galaxy.

4.3.1 Particle trajectories

The particle trajectories will be shown individually for GCRs and EGCRs, as the large-scale effects that emerge are different for the two. For GCRs, we expect a confinement in the GP at the lowest rigidi-

ties, which gradually weakens as rigidity increases and is negligible above $R \sim 1\text{EV}$. For EGCRs, the confinement in the GP towards lower rigidities is counteracted by shielding from the GP.

We track the trajectories of 100 GCRs, as well as 100 EGCRs, in the rigidity range $\left[10^{15}\,\text{V}, 10^{20}\,\text{V}\right)$ with an R^{-1} spectrum and plot them in 3D maps (projected onto the x-z plane). To better illustrate the predicted shielding and confinement effects, the maps are created for the rigidity bands described in section 3.2, with the particles' rigidities consistently colour-coded across the full rigidity range. They are depicted in figures 4.7 to 4.9. At the lowest rigidities, the shielding of the majority of EGCRs is visible. They do not reach the GP, but are reflected back outside of the Galaxy. In fact, their paths appear to reverse on large scales at larger Galactic latitudes, indicating that they mainly gyrate around field lines – characteristic of ballistic propagation – in the weaker fields outside the plane. The EGCRs that reach the GP have random trajectories and are effectively confined therein (and even appear to be pulled towards the GC where the field strength is largest; see also figure 3.2). GCRs, on the other hand, are confined in the GP and propagate diffusively therein until they eventually escape and travel ballistically to the edge of the Galactic volume. At intermediate rigidities, a larger number of EGCRs manage to penetrate into the GP. The confinement in the GP is still visible, even more so the concentration effect towards the GC. GCRs are still confined in the GP, but escape more quickly. The trajectories outside the plane are indicative of those from ballistic propagation (with particles experiencing only large-scale deflections). Those in the plane are still fairly random, though some begin to resemble gyrations along field lines, similar to the trajectories of low-rigidity particles outside the plane, especially for EGCRs. At the highest rigidities, the particle deflections become increasingly negligible; both GCRs and EGCRs only experience mild deflections by the GMF and traverse the Galaxy in similar timescales as particles unaffected by it. Their propagation becomes completely ballistic.

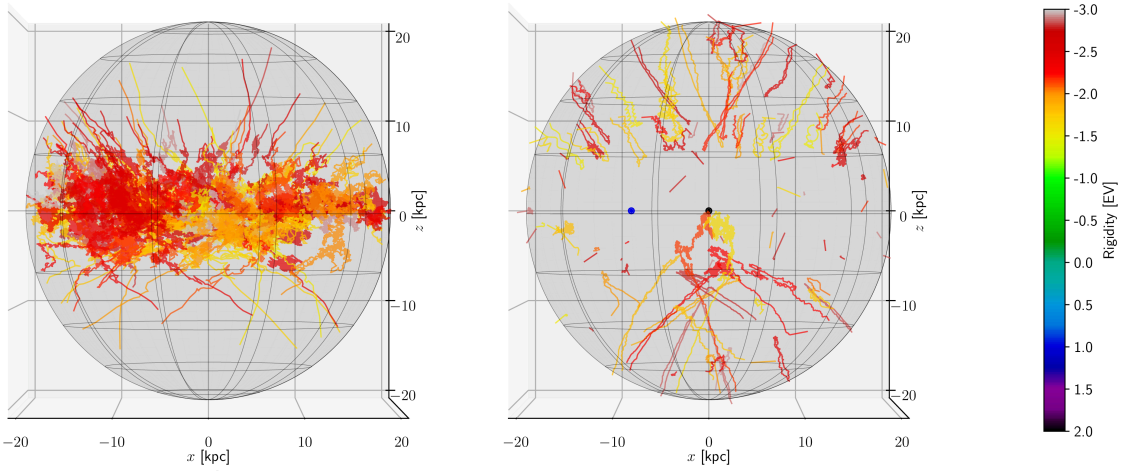

Figure 4.7: Galactic trajectories of 100 low-rigidity CRs ($I_{R,1} = \left[10^{15}\,\text{V}, 10^{16.5}\,\text{V}\right)$). The black dot indicates the GC and the blue dot the position of Earth in the Galaxy. Left: GCRs, right: EGCRs.

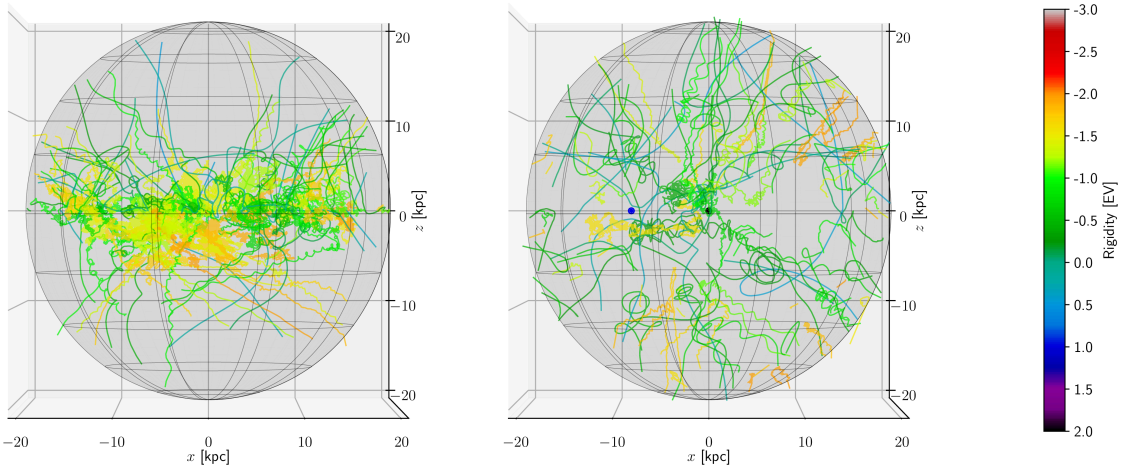

Figure 4.8: Galactic trajectories of 100 intermediate-rigidity CRs ($I_{R,2} = [10^{16}\,\mathrm{V}, 10^{18.5}\,\mathrm{V})$). The black dot indicates the GC and the blue dot the position of Earth in the Galaxy. Left: GCRs, right: EGCRs.

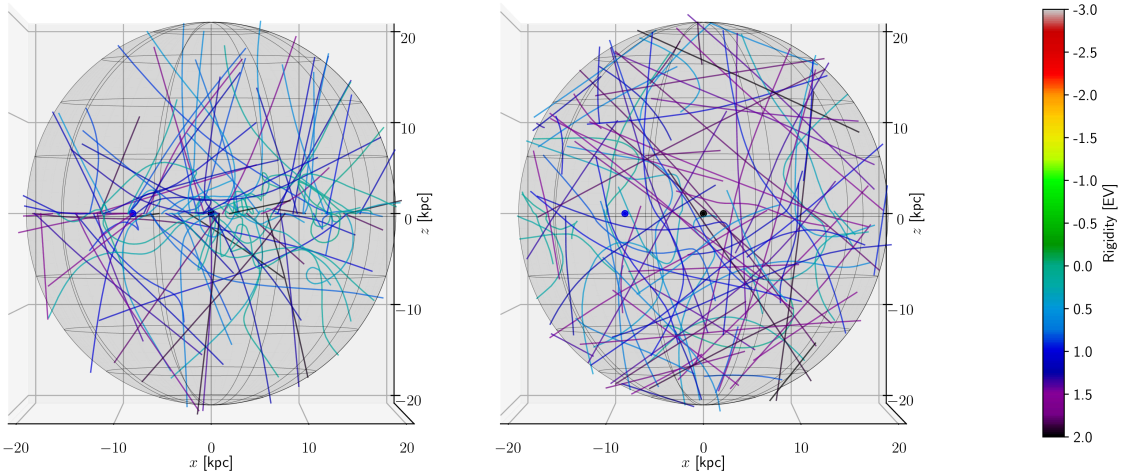

Figure 4.9: Galactic trajectories for 100 high-rigidity CRs ($I_{R,3} = [10^{18}\,\mathrm{V}, 10^{20}\,\mathrm{V})$). The black dot indicates the GC and the blue dot the position of Earth in the Galaxy. Left: GCRs, right: EGCRs.

4.3.2 Quantitative analysis

The 3D maps of Galactic trajectories presented in section 4.3.1 illustrate qualitatively that the GMF exhibits a range of large-scale effects on CRs of varying rigidity (i.e. shielding from and confinement in the GP for EGCRs, and confinement of GCRs) that can be understood via the change in propagation regimes that the particles occupy in different regions of the Galaxy at different rigidities. To demonstrate these effects quantitatively, the residence time in the GP of both GCRs and EGCRs (confinement/concentration effect), as well as the number of EGCRs reaching the GP (shielding), both as a function of rigidity, are studied. For our analysis, the GP is defined as in section 3.2 (including the varying radius in the case of EGCRs).

GCRs: Confinement in the GP

Due to their confinement, GCRs propagate a larger amount of time in the GP with respect to their total propagation time in the Galaxy. This can be quantified via the relative residence time within the GP $t_{\text{res.,in}}/t_{\text{res.,tot.}}$. The normalisation to the total time spent in the Galaxy takes into account the general expected increase in residence times as rigidity decreases. Its distribution is depicted in figure 4.10 in the form of a colour map, as well as its median value and median absolute deviation, as a function of rigidity.

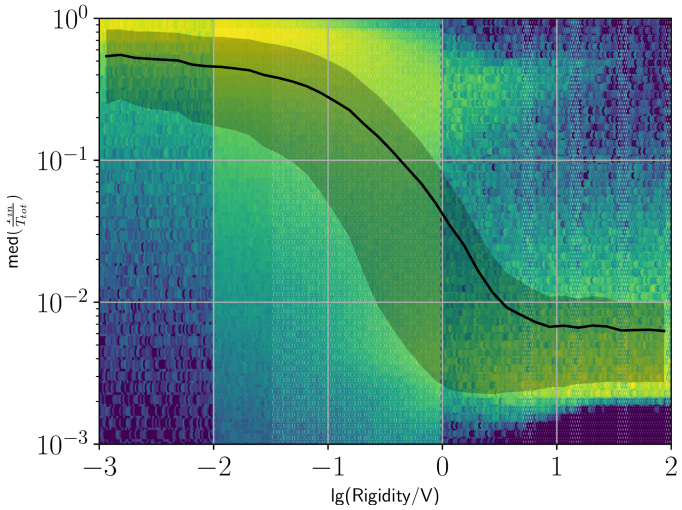

Figure 4.10: $t_{\text{res.,in}}/t_{\text{res.,tot.}}$ of GCRs as a function of rigidity, via its distribution (colour map), median value and median absolute deviation (black line and shaded area, respectively).

The relative residence time behaves similarly to the deflection angle in figure 4.2, with an inflection point at $\gtrsim 1\,\text{EV}$, where the median value increases and flattens at $\sim 50\,\%$ at the lowest rigidities. The colour map reveals an additional feature in the relative residence time in the rigidity range of roughly 10^{17}–$10^{19}\,\text{eV}$, where two regions of increased intensity appear in the distribution. This indicates that relative residence times are either very short ($< 1\,\%$) or very long ($> 10\,\%$). This feature is likely a consequence of the magnetic field topology, namely the existence of regions in the GP with very weak fields and regions with very strong fields, such as in spiral arms.

EGCRs: Shielding from and confinement in the GP

To quantify the shielding of EGCRs, the number of particles that reach the GP $N_{\text{GP,obs.}}$ is counted. The amount of shielding is calculated via the fraction $f_{\text{GP}} = N_{\text{GP,obs.}}/N_{\text{GP,0}}$, where $N_{\text{GP,0}}$ is the expected CR count in the field-free case which approximate via the number of CRs arriving at the highest rigidity bin. The GP is defined as in section 3.2, including the fiducial cut. f_{GP} as a function of rigidity is plotted for several cylinder radii in figure 4.11.

Per construction, the fraction of particles reaching the GP is constant at unity for highest rigidities, at an inflection rigidity of $\sim 1\,\text{EV}$, it drops rapidly for decreasing rigidity, with the trend slowly flattening at the lowest rigidities. This is the trend expected from the shielding effect. Moreover, the trend is consistent with the propagation features discussed in sections 4.1 and 4.2 with the inflection point roughly matching. Particularly, the assignment of the propagation regimes and the transition between them is reflected in the trend: In the flat region, the propagation is completely ballistic, beyond the inflection rigidity, the propagation transitions to diffusive, and beyond the second inflection point at about $10^{17}\,\text{V}$, where the curve flattens towards lower rigidities, the propagation becomes primarily diffusive.

When comparing the trend for different GP radii r_{GP}, two interesting features become visible, one at the largest and smallest depicted value, respectively. In both cases, the shielding is weaker compared to the other radii, their specific underlying cause is, however, different. The decreased shielding for the largest radius is a result of the discontinuous drop-off of the magnetic field at the edge of the Galaxy discussed in section 3.2, that constitutes the motivation for including a fiducial cut, and is thus a mere artefact of the setup. For the smallest radius, the reduced shielding stems from a further concentration effect towards the GC. In addition, for the smallest value of r_{GP}, the flat region at high rigidities also extends further down in rigidity, compared to larger sphere radii. This indicates either that higher-rigidity particles which reach the GP cylinder for the smallest radius propagate ballistically down to lower rigidities than for larger radii, or that the shielding is counteracted by this concentration effect. Given that the cumulative magnetic

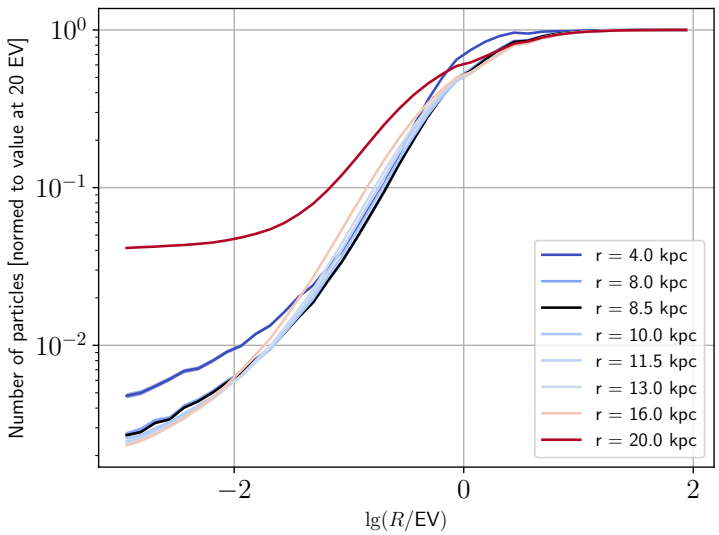

Figure 4.11: f_{GP} as a function of rigidity for several GP cylinder radii signified in legend. The GP radius equalling th distance of Earth to the GC is highlighted in black.

field stengths that have to be traversed to reach the inner region of the GP are higher than for the outer regions, the latter alternative seems more plausible.

As for GCRs, the confinement of EGCRs is quantified via the relative residence time within the GP ${}^{t_{\mathrm{res.,in}}}/_{t_{\mathrm{res.,tot.}}}$. A further consideration that has to be made is the fact that the absolute residence time in the GP varies with the GP radius, as the volume within which to reside varies. Instead of scaling each cylinder by its size, the residence time is calculated within concentric ring sections of equal area[3] to study the effects of the radius of the GP cylinder. In figure 4.12, the median value of ${}^{t_{\mathrm{res.,in}}}/_{t_{\mathrm{res.,tot.}}}$ is plotted for various (inner and outer) ring radii, indicated via colour-coding, as a function of rigidity.

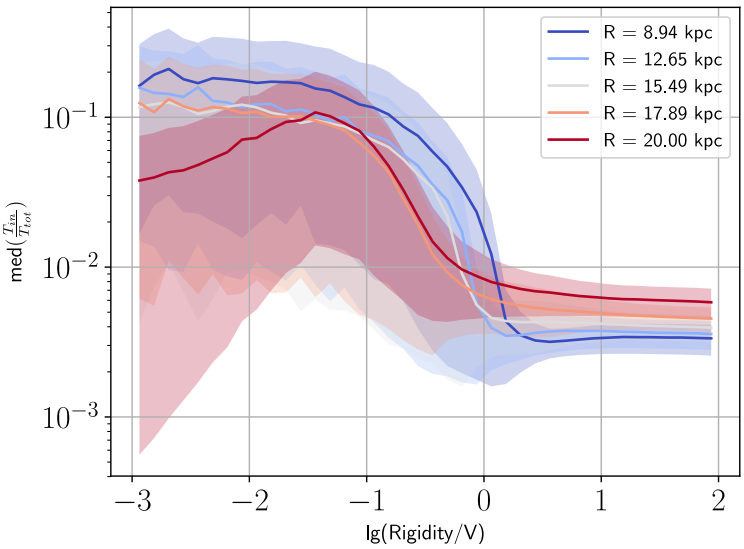

Figure 4.12: ${}^{t_{\mathrm{res.,in}}}/_{t_{\mathrm{res.,tot.}}}$ of EGCRs as a function of rigidity, via its median value and median absolute deviation (line and shaded area, respectively) for different outer radii of ring sections, signified in the legend. The ring with the smallest value has an inner radius 0, i.e. it is a circle; for each subsequent value its preceding value signifies the inner radius.

At the highest rigidities, the proportion of time spent in the GP is very small (less than 1 %) and roughly flat with rigidity. Below around 1 EV, the relative residence time increases drastically by almost two orders of magnitude, and slowly flattens towards lowest rigidities, where particles spend up to 10–20 % in the plane[4]. The outermost ring defies this trend, with a turning point at round 50 PV, which can be

[3] The innermost ring has an inner radius of 0, making it a circle.

[4] This implies that GCRs spend a larger fraction of their residence time in the Galaxy within the GP compared

well understood considering the sharp drop-off of the magnetic field at the edge of the Galaxy, as discussed in section 3.2. More particles are directly reflected back to the edge of the Galaxy soon after injection (and don't penetrate further into the Galaxy than a 1 kpc; see also figure 3.2) as rigidity decreases.

Otherwise, the trend reflects the expectations from the propagation features observed in sections 4.1 and 4.2, and is consistent with the relative residence time of GCRs. The flat region at the highest rigidities signifies the ballistic regime and the region below the inflection rigidity reflects the transition to diffusive propagation with the trend flattening similarly to figure 4.10. In addition, the concentration effect towards the GC is also visible with the relative residence time reaching higher values at the lowest rigidities for the inner rings of the plane.

In an attempt to combine the residence time increase with the shielding for the case of EGCRs, or to identify the expected effect of the decreased confinement of GCRs with rigidity, a "steady-state" approach is employed. Its details and the result of the analysis is described in the following.

4.3.3 Steady-state approach

In the steady-state approach, N particles are tracked from their origin until they leave the Galaxy, measuring the propagation time, which we call the Galactic residence time $t_{\mathrm{res,gal}}$. Using this value for each particle, we count the number of particles that still reside in the Galaxy after time t. Via (logarithmic) rigidity binning, we obtain the time evolution of the number of particles $N_i(t;\, R_i)$ for each rigidity bin R_i. To mimic a continuous source output, we create a sum of n time evolutions for each rigidity bin R_i, each with an increasing time offset $j \cdot \Delta t$ (see equation 4.1).

$$N_{\mathrm{SS},\,i} = \sum_{j=0}^{n} N_i(t + j \cdot \Delta t;\, R_i) \cdot \Delta t \tag{4.1}$$

In the limit of $\Delta t \to 0$ and $t \to \infty$, a steady-state regime is reached, where $N_{\mathrm{SS},i}$ is constant. We implicitly assume that the age of the Galaxy is large compared to the residence times of the particles $t_{\mathrm{res},i}$, and that the offset Δt is small compared to the width of the time evolution $N_i(t; R_i)$ for all rigidity bins R_i. $N_i(t; R_i)$ is re-injected n times, with n, such that $t_{\mathrm{max}} = n \cdot \Delta t$, where $N_i(t > t_{\mathrm{max}}; R_i) = 0$. The number of particles in the steady-state is proportional to the time integral of $N(t)$.

$$\lim_{t \longrightarrow \infty} \left(\lim_{\Delta t \longrightarrow 0} N_{\mathrm{SS},\,i} \right) = \lim_{t \longrightarrow \infty} \left(\lim_{\Delta t \longrightarrow 0} \sum_{j=0}^{n} N_i(t + j \cdot \Delta t;\, R_i) \cdot \Delta t \right) \tag{4.2}$$

$$= \lim_{t \longrightarrow \infty} \int_0^t N_i(t;\, R_i)\, dt \tag{4.3}$$

$$= \int_0^{\infty} N_i(t;\, R_i)\, dt. \tag{4.4}$$

Rigidity bins with wider time evolutions reach a steady-state later in time, and $N_{\mathrm{SS},i}$ reaches a large value (assuming equal initial particle numbers $N_i(t = 0;\, R_i)$ for all rigidity bins). Due to the fact that low-rigidity particles have vastly longer residence times than higher-rigidity ones, the simulation and analysis is performed separately for the three rigidity bands described in section 3.2. An added benefit of segmenting the analysis in such a way is that this enables the simulation of more higher-rigidity particles (that consume less computation time), and thereby increases statistics for these rigidities, which is particularly useful for GCRs, for which the flux of higher-rigidity particles is expected to be suppressed.

The choice of the observer is the GP as defined in section 3.2, meaning that only particles that reach the GP are tracked. The injection spectrum is R^{-1}, and the source distributions are the GP with an isotropic injection direction distribution in the case of GCRs, and the edge of the Galaxy with a Lambertian injection direction distribution in the case of EGCRs.

GCRs

The number of simulated particles for each range is $N_{R,1} = 10^6$ and $N_{R,2} = N_{R,3} = 10^7$, respectively. Figure 4.13a shows the time evolution of particles across the entire rigidity range (they were also combined by re-scaling the individual time evolutions at the overlapping region). It is clearly visible that the residence time in the Galaxy decreases with rigidity, as the confinement due to the magnetic field becomes weaker. The plot reveals realistic residence times of a few 10 Myr. This is slightly higher but in the same order as leaky-box estimations and inferences from measurements of secondaries (see e.g. [119, 120]).

In figure 4.13b, the steady-state count for each rigidity bin after re-injection is plotted. The count drops off rapidly with increasing rigidity as CRs more easily escape the Galaxy, becoming steeper until

to EGCRs, which is plausible given that GCRs are created therein.

around 1 EV, after which it flattens out, as the confinement by the GMF becomes increasingly negligible. It seems to exhibit a "knee"-like feature naturally as a consequence of the CR transport in the GMF, much in line with [121] and [122]. This has implications for required source flux features, mainly along the lines of the required spectrum at the highest energies of Galactic sources and their positions (i.e. not inside the GP), if the GCR flux is expected to add a significant contribution to the overall CR flux towards higher energies.

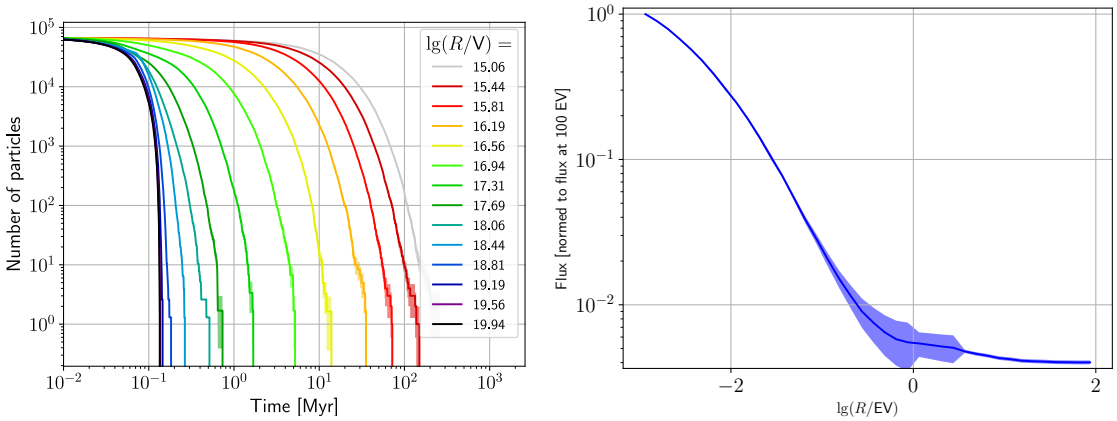

(a) Time evolution of GCR protons injected from the GP (with $r_{GP} = 20\,\text{kpc}$) in the Galactic volume.

(b) Steady-state count of GCR protons acquired from the time evolutions.

Figure 4.13: Steady-state analysis for GCRs.

EGCRs

The EGCRs propagation effects include their increased shielding from and confinement in the GP with decreasing rigidity. These features are sought to be combined in the steady-state analysis. To this end, of the $N = 2 \cdot 10^7$ injected EGCR protons, only those reaching the GP will be considered in the analysis to include the shielding effect. While the entire GP (i.e. with the largest radius of the disk), as well as all injected particles were used in the analysis in the case of GCRs, the disk radius will affect the results of the analysis in the case of EGCRs, as already seen in figure 3.2. To investigate the effect of different disk radii, maximum and miminum disk radii of varying magnitude will be chosen, and only particles which fall within the desired radius range will be selected for analysis. We count all particles that reach the GP at some radius r or lower. The time evolution for a disk radius of 8.5 kpc, and the steady-state count for all disk radii are plotted in figures 4.14a and 4.14b. The shielding effect is visible in the decreasing initial counts $N_i(t = 0; R_i)$ for lower-rigidity bins, and the confinement manifests in the form of an increased residence time. The change of both the shielding and the confinement appear to be small at the highest and lowest rigidities, much in line with figures 4.11 and 4.12. For intermediate rigidities, shielding appears to dominate, as discernible in decrease of the steady-state count at these rigidities in figure 4.14b. At the lowest rigidities, confinement appears to dominate such that the steady-state count increases again with decreasing rigidity. These results illustrate three main large-scale effects of the propagation of EGCRs, them being shielding from the GP, confinement in the GP and a possible pull towards the GC. These results give an ambiguous picture of the actual interplay between particularly shielding and confinement of EGCRs as a function of rigidity[5], substantiating the need of explicitly measuring the flux of EGCRs arriving at Earth via forward tracking. Conversely, the change propagation effects of GCRs, i.e. confinement, with rigidity, do lead to clear expectations for the flux of GCRs, namely a flux suppression towards higher rigidities.

[5] The apparent concentration effect towards the GC is not expected to have as important an effect as the shielding and confinement for observers sufficiently far away from the GC, such as Earth.

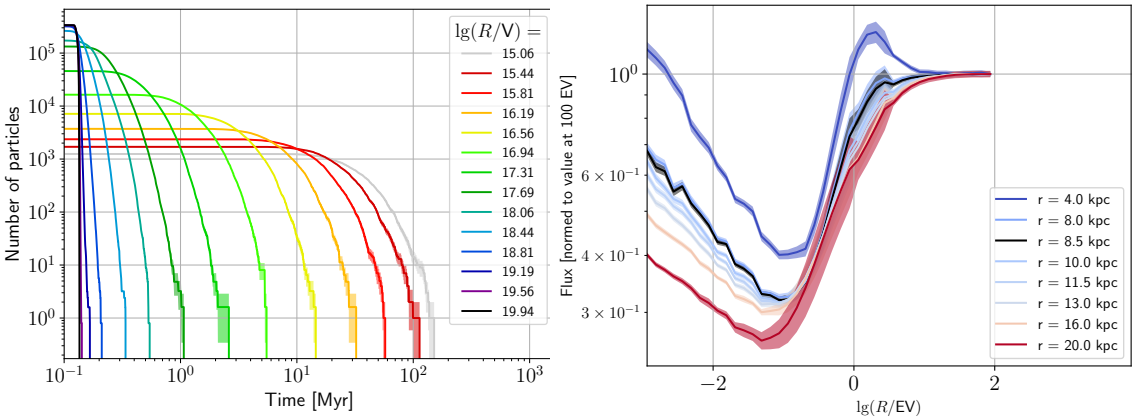

(a) Time evolution of EGCR protons that reach the GP (with $r_{\mathrm{GP}} = 8.5\,\mathrm{kpc}$) in the Galaxy volume.

(b) Steady-state count of EGCR protons acquired from the time evolutions.

Figure 4.14: Steady-state analysis for EGCRs.

Before turning to the effects on observables, however, it is important to discuss the validity of Liouville's theorem, as this further dictates the necessity of studying the propagation effects of EGCRs via forward tracking. This is done via the analysis of the first adiabatic invariant, defined in section 2.4.2.

4.4 Testing Liouville – First adiabatic invariant

As described in section 2.4.2, the conservation of the phase space density central to Liouville's theorem implies the conservation of other quantities, one of them being the first adiabatic invariant, often represented via the classical magnetic moment $\mu = {}^{e}/_{2\,m\pi\,c} \cdot I$. To test the change of this quantity during a particle's propagation, its mean and standard deviation $\langle\mu\rangle$ and σ_μ are calculated. If Liouville's theorem holds, the ratio $r_\mu = {}^{\sigma_\mu}/_{\langle\mu\rangle}$ is expected to be small (i.e. < 1). This ratio was calculated as a function of rigidity for $N_{R,2} = 239$ and $N_{R,3} = 3,300$ particles that reach the GP for the two overlapping rigidity bins in the rigidity range of $\left[10^{16}\,\mathrm{V}, 10^{20}\,\mathrm{V}\right)$ (defined in section 3.2) with an R^{-1} spectrum. The resulting histogram of the distribution of r_μ for each rigidity bin, as well as its median are plotted as a function of rigidity in figure 4.15 for a cylinder radius of 11.5 kpc[6]. The same two plots for a cylinder radius of 19 kpc, the largest radius that corrects for which the systematic bias due to the discontinuous drop-off of the magnetic field strength at the edge of the Galaxy, is depicted in figure A2

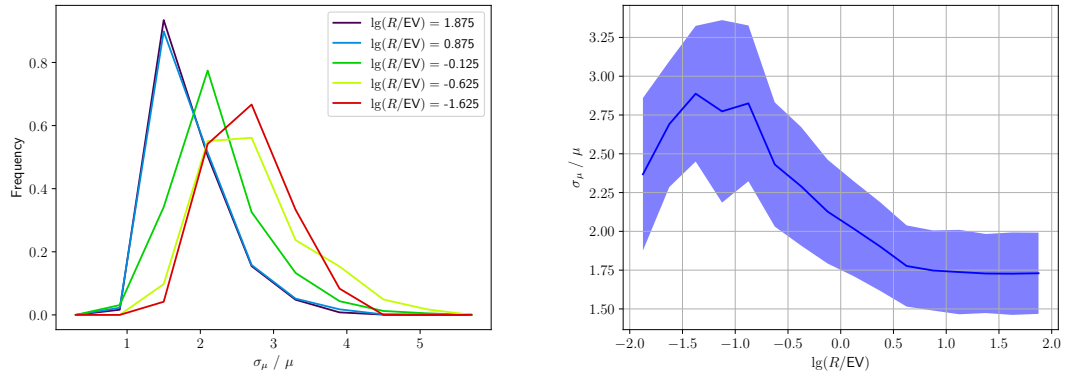

(a) r_μ distribution for different rigidities signified in the legend.

(b) Median of r_μ as a function of rigidity with the spread quantified via the median absolute difference.

Figure 4.15: Dependence of r_μ on rigidity for a cylinder radius of 11.5 kpc.

As for figure 4.3, we have an inflection point at $\gtrsim 1\,\mathrm{EV}$, where r_μ increases as rigidity decreases until $\gtrsim 0.1\,\mathrm{EV}$, beyond which it flattens. At the lowest rigidities, r_μ possibly even decreases as rigidity

[6] This is the smallest radius for which the statistics is high enough (i.e. the of CR count reaching the GP is large enough to acquire continuous distributions of r_μ with the the chosen binning of 0.6) for all rigidities.

decreases, although only marginally. This dependence of r_μ on rigidity indicates that collisions may very likely occur in the course of a particle's propagation towards lower rigidities. Though $r_\mu > 1$ for all rigidities, indicating that the change of μ is large even at the highest rigidities, the fact that r_μ is constant down to the inflection point suggests that the value of r_μ at the highest rigidities represents the change of μ in the case of collisionless propagation. This inference is further substantiated when considering that the trajectory length distributions of EGCRs is also flat down to the same inflection rigidity (see figure 4.5).

Figure 4.3 shows that deflections below $\sim 1\,\mathrm{EV}$ are substantial. Figure 4.15 indicates that, at the lowest rigidities, these can be so large that they would effectively resemble a collision. When comparing with the distributions for a cylinder radius of 19 kpc (see figure A2), we see that the increase in r_μ stems primarily from CRs that reach far into the Galaxy approaching the GC. Whether they make up a significant fraction of the flux arriving at Earth, which is situated further from the GC, is questionable. Making inferences on the validity of Liouville's theorem based on these results is not easily possible. The lack of conservation of the magnetic moment as defined in equation 2.30 is expected to occur at high turbulence levels [123], which seem to be present for the JF12 field; the ratio of the strength of the turbulent field b with respect to the strength of the coherent field B is ${}^{b}/_{B} \sim 1$ for many regions in the Galaxy [100]. In addition, the definition in equation 2.30 does not take into account any drift motion that may occur [124]. The applicability of Liouville's theorem needs to be explicitly tested via forward tracking of CRs to Earth, adding an extra reason to perform such studies, before the computationally cheaper backward-tracking approach may be employed.

Chapter 5

Identifying propagation effects in cosmic ray observables

As shown in section 4.3, the deflections of GCRs and EGCRs in the GMF lead to a range of effects. Low-rigidity GCRs are confined in the GP, whereas low-rigidity EGCRs are shielded from the GP while those that do reach the GP are confined therein. These effects all gradually cease as rigidity increases. In this chapter, we investigate how these effects modify the flux, composition and arrival direction distribution of both GCRs and EGCRs. Before tackling each observable, a small motivation to the manner in which the propagation effects observed in chapter 4 may modify them is helpful.

First, the decreasing confinement of GCRs in the GP is expected to lead to a flux suppression with increasing GCR rigidity, as seen in section 4.3.3. For EGCRs, the expected modification is less clear. On the one hand, the shielding effect of EGCRs may lead to a flux suppression of lower-rigidity EGCRs. On the other, the shielding may be counteracted by the confinement of those CRs reaching the GP, or more precisely, the increased covered volume fraction that they cover with decreasing rigidity (as shown in section 4.2). Flux modification would imply a modification of mixed initial CR compositions — that are expected throughout the entire energy range of interest [1]. This is because differently charged particles of equal energy have different rigidities (scaling with their electric charge $Z\,e$). Lastly, the measured arrival direction distribution may also exhibit features stemming from the propagation in the GMF. The deflection of particles with rigidities just below the ballistic regime may cause regions of suppression or enhancement for certain arrival directions at the observer (particularly EGCRs, whose shielding commences at these rigidities — provided that Liouville's theorem does not hold). The random motion of diffusively propagating CRs smears out existing anisotropies in the injected flux. In addition, regions of the sky of increased and decreased Galactic transparency arise from the existence of the GMF, which shift with rigidity. An anisotropic injection of EGCRs may therefore give rise to flux modifications.

5.1 On flux modification — Observer sphere method

The approach of choice to study the propagation effects of the GMF on the flux (and consequently, the composition) is the "observer sphere" method, where the flux is estimated via the number of CRs that cross the shell of a sphere centered at the observer position (i.e. Earth). While this approach is computationally expensive, it can further be used to study the effects on the arrival direction distribution.

5.1.1 Method details

An implicit assumption made in the observer sphere method is that the propagation time of CRs in the Galaxy is significantly shorter than the lifetime of the source (i.e. no transient sources), as longer track lengths on the way to the observer are not accounted for. In addition, there may be sources of systematic bias if the sphere radius r_{obs} is not sufficiently small. As for the choice of the optimal minimal step size of the simulation (see section 3.2), a suitable measure is the particle's gyro radius r_{g}. This quantity should be of similar scale as r_{obs}. This condition is not easily achievable, as the already computationally expensive forward-tracking approach loses statistics in the order of the radius squared. Using equation 3.3, a PV-rigidity particle would have a gyro radius of the order of a one to a few parsec, resulting in a geometric fraction of $\sim 10^{-8}$. Simulating more than 10^{10} particles is not feasible with available resources, especially with the inclusion of particle rigidities down to the PV scale, which require a large CPU time per particle to simulate (see also figure 3.4c). This restricts the minimal sphere size to around 10 pc, for an expected statistics of $\lesssim 10^4$ particles. To check how the sphere size affects the resulting flux, several spheres of

decreasing radii were chosen: $R = 1\,\mathrm{kpc},\ 500\,\mathrm{pc},\ 100\,\mathrm{pc},\ 50\,\mathrm{pc},\ 20\,\mathrm{pc},\ 10\,\mathrm{pc},\ 5\,\mathrm{pc}$[1]. All observer spheres can be included in the same simulation, so the choice of the minimal radius does not come at the cost of computation time. N protons are forward tracked and their rigidity and arrival direction are registered if they cross the surface of the observer sphere of radius r_{obs}[2]. With these quantities, the arrival direction distribution and the spectrum[3] are determined.

5.1.2 GCRs

For the Galactic flux, $N = 5 \cdot 10^8$ protons are injected with a homogeneous distribution in the GP, save the region with distance 0.5 kpc from Earth's position, and an R^{-1} rigidity distribution in the range of $10^{16}\,\mathrm{V}$ to $10^{20}\,\mathrm{V}$. In addition and in anticipation of the flux suppression for higher rigidities, $N = 5 \cdot 10^9$ protons in the rigidity range $10^{17}\,\mathrm{V}$ to $10^{20}\,\mathrm{V}$ and $N = 10^{10}$ protons in the rigidity range $10^{17.5}\,\mathrm{V}$ to $10^{20}\,\mathrm{V}$ are further injected. In overlapping rigidity bins, the weighted mean flux from all three rigidity ranges is calculated to quantify the total flux at these rigidities. The resulting rigidity spectrum, i.e. the number of CRs registered normalised to the geometric fraction as a function of rigidity, is depicted for all sphere sizes (see figure 5.1).

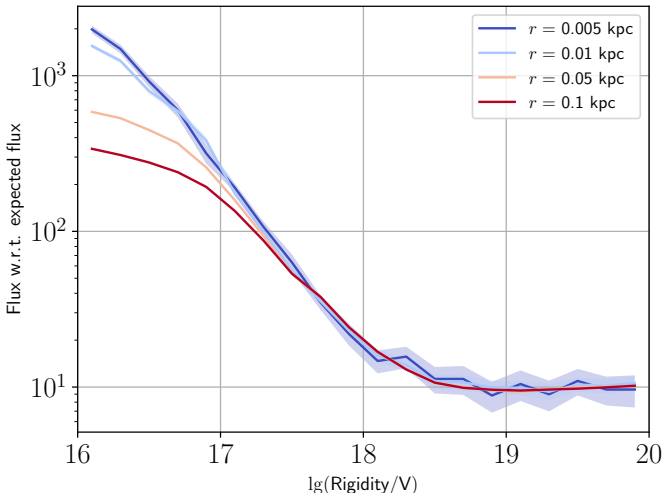

Figure 5.1: Simulated rigidity spectrum of GCRs from the observer sphere method for various observer sphere radii signified in the legend.

As expected, there is a flux suppression towards higher rigidities. More precisely, the flux is enhanced towards lower rigidities given that the flux at lower rigidities is higher with respect to the expected flux. There appears to be two breaks in the spectrum at inflection rigidities $\approx 10^{17}\,\mathrm{V}$ and $\approx 10^{18}\,\mathrm{V}$, the first onsetting a spectral softening and the second a spectral hardening (see also figure A3). The degree of enhancement, particularly at lowest rigidities, increases with decreasing observer sphere size. To quantify this increase and to identify a possible convergence of this trend with which to estimate the flux for a point source, we fitted three lines to the data in log-log representation. At the highest energies, the line signifies the flat region with a slope of zero, and the other two signify the enhancement regions with a non-zero slope. The slopes indicate the spectral index minus one. From the lines, we can infer the relative enhancement at 1 PV, and the intersection rigidity of the three lines where the enhancement begins, and flattens, respectively. The enhancement regions are numbered from left to right in rigidity (i.e. 1: less steep region, 2: steepest regions, 3: flat region). The change of the degree of enhancement and the corresponding spectral index of the suppression regions with observer sphere radius are depicted in figure 5.2.

The right two plots indicate that the increase of the enhancement with decreasing sphere size is primarily caused by the steepening of the first enhancement region; the increase of the slope magnitude in this

[1] For GCRs, the largest observer sphere radius is set to 100 pc. The reason for this is that we exclude source locations that are closer than 500 pc from Earth (see section 3.2), because we want to eliminate sources located inside the observer sphere as well as to avoid artefacts arising from nearby sources. At the same time, we want to limit the fraction that area of forbidden source locations take up of the entire GP. We found the minimum source distance to Earth of 500 pc to be a suitable compromise.

[2] Multiple crossings of the sphere surface are not considered.

[3] The units of the flux are dimensionless by scaling the number of hits with the expected hit rate from the geometric fraction and number of equidistant rigidity bins; that way, any flux modifications are visible as deviations of the flux from 1.

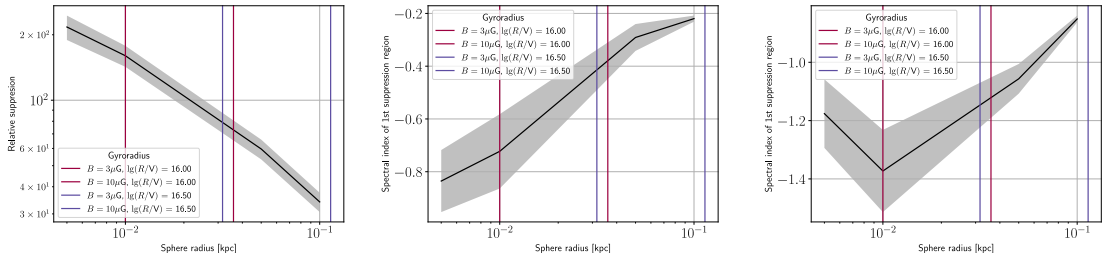

(a) Enhancement at 1 PV. **(b)** Slope of first region. **(c)** Slope of second region.

Figure 5.2: Change of enhancement at 1 PV (left) and non-zero spectral slopes of the GCR rigidity spectrum with observer sphere radiu (centre and right). The vertical lines indicate the gyro radii of particles of various rigidities and field strengths as signified in the respective legends.

region continues all the way to smallest observer sphere sizes, while this trend appears to cease at around 10 pc for the second region. This also visually discernible in figures 5.1 and A3. The left plots shows no clear end to the enhancement as the observer approaches a point source, but given that the maximal gyro radius at the lowest rigidity, 10^{16} V, for a field strength of $B = 10\,\mu$G is larger than the sphere radius with 11 pc (see equation 3.3), propagation within even smaller spheres is virtually ballistic, and the trend is not expected to continue significantly further.

5.1.3 EGCRs

For the isotropic extragalactic flux, $N = 5 \cdot 10^9$ protons are injected with a Lambertian injection direction distribution and an R^{-1} rigidity distribution in the range of 10^{16} V to 10^{20} V. The resulting rigidity spectrum, i.e. the number of CRs registered normalised to the geometric fraction as a function of the logarithm of rigidity, is depicted for all sphere sizes (see figure 5.3). For larger sphere sizes, there appears to be a flux suppression for rigidities below $\approx 10^{18}$ V, which disappears as the sphere approaches a point. With the same argument about the gyro radius and the size of sphere as in section 5.1.2, we can confidently infer that the trend towards a flat spectrum continues for even smaller sphere sizes. The change of the flux suppression with observer sphere radius was also quantified as in section 5.1.2 via lines to the data in log-log represention, but only with one signifying the suppression region. Its slope indicates the spectral index minus one. Again, the relative suppression at 1 PV, and the intersection rigidity of the two lines where the suppression begins were calculated. The change of the relative suppression and of the spectral index of the suppression region with observer sphere radius are depicted in figure 5.4. They both approach zero for smallest sphere radii, further establishing confidence in the lack of flux suppression for a point observer.

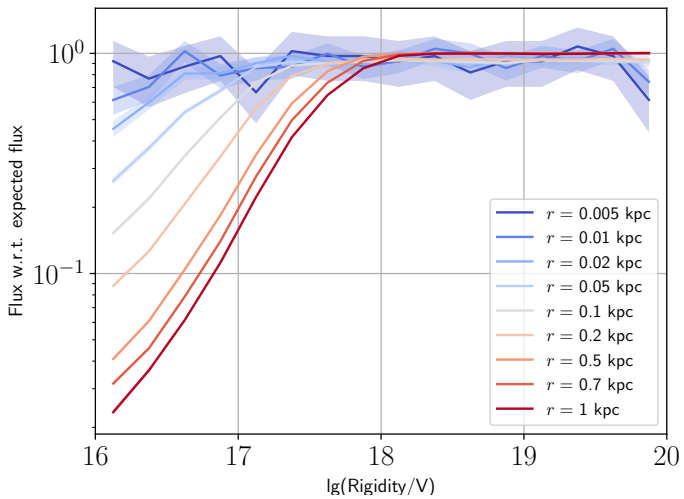

Figure 5.3: Simulated rigidity spectrum of EGCRs from the observer sphere method for various observer sphere radii signified in the legend.

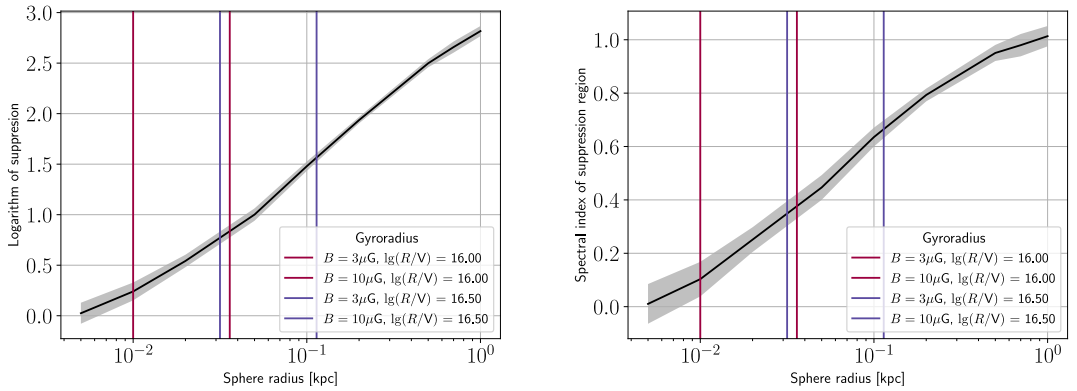

(a) Suppression at 1 PV.

(b) Slope of suppression region.

Figure 5.4: Suppression (left) and spectral slope (right) of the EGCR rigidity spectrum as a function of observer sphere radius. The vertical lines indicate the gyro radii of particles of various rigidities and field strengths as signified in the respective legends.

The lack of flux suppression for the smallest sphere sizes, and probably down to a point observer, implies that shielding and the confinement exactly cancel. In addition, this result confirms one central prediction of Liouville's theorem, namely flux conservation. This is striking in light of the findings in section 4.4. The most likely explanation for the discrepancy is that the conservation of the first adiabatic invariant as defined in equation 2.30 during propagation does not hold for strong turbulence levels [123], despite the conservation of phase space density still holding.

5.2 On composition modification

The differing effects of the GMF on the flux of GCRs and EGCRs, respectively, found in section 5.1, also has implications for the composition of CRs in the transition region. The flux, and hence composition, of EGCRs is unaffected by the GMF. The suppression of the GCR flux towards higher rigidities, however, is expected to lead to an increasing mean mass at low and intermediate energies of the transition region. This increases ceases and reverses at highest energies, as the flux of the highest-rigidity nucleus, hydrogen, flattens. Therefore, this section focuses solely on the composition modification of GCRs.

To retrieve the modified composition of GCRs, a sensible injected composition needs to be chosen. As is common in CR composition analyses at these energies where indirect methods are used to infer the mass, we opt for a four-component composition consisting of protons (or hydrogen), helium, an intermediate mass range nucleus represented by oxygen and a high-mass nucleus represented by iron. In [23], nuclear abundances were retrieved via fitting of lines with equal spectral index to AMS02, CREAM, TRACER and ATIC-2 data, with [p, He, O, Fe] = [45.0 %, 35.75 %, 9.625 %, 9.625 %][4]. Given their assumption of the equal spectral indices of the source spectrum for all nuclear species, the resulting abundances are suitable for our purposes as well, and are adopted in the following. To calculate the composition as a function of energy, the rigidity spectrum (i.e. the spectrum depicted in figure 5.1) is shifted such that the energy equals the rigidity multiplied by its charge number Z for each nucleus. The spectra for all nuclei are then scaled with their relative abundance and superimposed on one another. The resulting total energy spectrum and mean logarithmic mass number $\langle \ln A \rangle$ are plotted in figure 5.5.

The expected trend, that the mean mass increases up to intermediate energies and subsequently decreases at hightest energies, is reproduced. Due to the high charge of iron, the window of overlapping energies for all nuclei begins at rather high energies: $[10^{16} \cdot Z_{\text{iron}}\,\text{eV}, 10^{20} \cdot Z_{\text{proton}}\,\text{eV}] = [10^{17.4}\,\text{eV}, 10^{20}\,\text{eV}]$. At this energy, the composition is already heavy, with iron making up the bulk of the share of nuclei, followed by oxygen, helium and then hydrogen. In addition, the GCR flux is expected to sub-dominant at these energies, limiting the usefulness of these results. Given this, we fitted a sigmoid function ($f(x) = A/(1+\exp((x-C)/B)) + D$, where A, B, C and D are free parameters[5]) to the rigidity spectrum in figure 5.1, to extend the energy range arbitrarily downward. The choice of a sigmoid function as a fit which flattens towards $x \to -\infty$ stems from expectation that the increase of confinement of CRs in the GP flattens out towards lowest rigidities, as the extent of the plane and halo regions is significantly larger

[4] Actually, they additionally had silicon in their CR mix, whose flux we simply combined with the iron flux.

[5] The parameter A gives the initial flux before the confinement begins to decrease. B and C define the steepness and the shift (along the x-axis) of the fitting function; they were introduced to retrieve the same steepness of the rigidity spectrum beyond $\approx 10^{17.5}$ V for all shell sizes, that was observed. D gives the final flux in the field-free case.

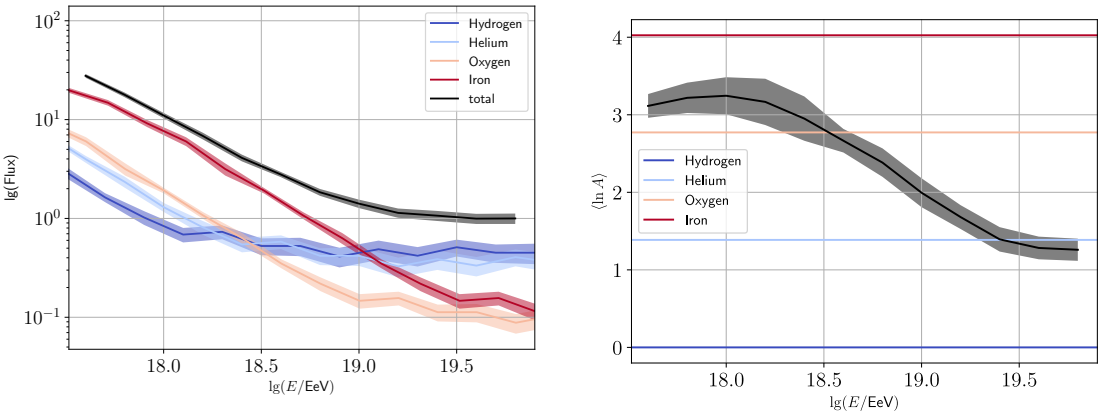

(a) Total energy spectrum in overlapping region.

(b) Mean logarithmic mass number $\langle \ln A \rangle$.

Figure 5.5: Composition modification of GCRs.

than the gyro radius of the CR particle ($h_{\mathrm{GP/halo}} >> r_{\mathrm{g}}$, or ${}^{r_{\mathrm{g}}}/_{h_{\mathrm{GP/halo}}} \to 0$). Indeed, the sigmoid fit works very well (see figure A3). The resulting rigidity spectra, and total energy spectrum and mean logarithmic mass number $\langle \ln A \rangle$ are plotted in figures 5.6.

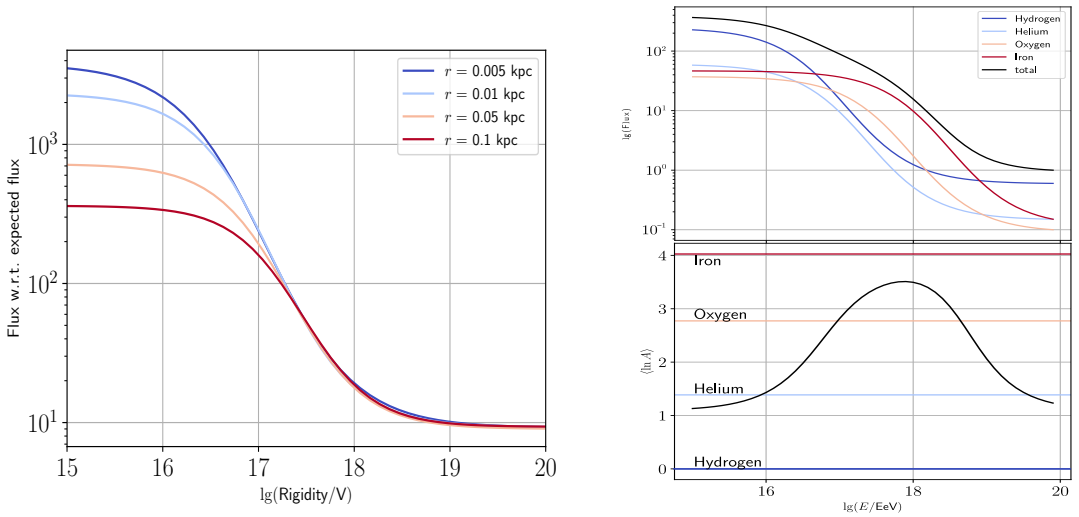

Figure 5.6: Left: Sigmoid fit of the rigidity spectrum of GCRs for various observer sphere radii signified in the legend. Top right: Total energy spectrum in overlapping region, bottom right: mean logarithmic mass number $\langle \ln A \rangle$ (both for sigmoid fit).

In this extended energy range, we see the expected increase in the mean logarithmic mass number towards higher energies up to the ankle. In other words, propagation in the GMF modifies the GCR composition in the "shin" region towards a larger mean mass.

5.3 Arrival direction distribution

The arrival direction distribution is a further observable that contains information about the origin of CRs. Most relevant for the investigation of propagation effects by the GMF are large-scale anisotropies as they are the most robust with respect to variations in the source properties and distribution, as well as to the topology of extragalactic magnetic fields. Due to the deflection in the GMF, any anisotropies in the injection direction distribution into the Galaxy are shifted or smeared out during propagation and when subsequently measured at Earth. Of particular interest are two extreme cases: One being the "anisotropisation" (i.e. the existence of preferred arrival directions intrinsic to the magnetic field topology) of isotropic injections, as well as the "isotropisation" (i.e. the degree to which injection directions are smeared out by the magnetic field) of anisotropic injections. If isotropisation is strong at specific rigidities, information on the source direction may be lost. Thus, anisotropisation must be sufficiently strong or

isotropisation sufficiently weak in order to gain insight into the relative contributions of the GCR and EGCR components in the transition region. How (an-)isotropisation manifests for GCRs and EGCRs differs will be discussed in the following. All distributions will be shown for an observer sphere radius of 10 pc; while the flux changes for both GCRs and EGCRs as the sphere size is further reduced (see figures 5.1, 5.6 and 5.3), this is the smallest sphere size that provides sufficient statistics to discern patterns and draw quantitative conclusions. In addition, the features found in the arrival direction distribution for this sphere size are expected to be robust as sphere size is further reduced, as significant deflections are not expected to occur at parsec-level length scales in this rigidity range (see equation 3.3).

5.3.1 GCRs

Given the source distribution of GCRs, the arrival direction distribution is highly anisotropic if CRs moved undeflected from source to observer. Therefore, it is of particular interest to which extent the GMF isotropises the anisotropic flux. To investigate this, the arrival direction distribution is plotted on a sky map for various rigidity bins in range of 10^{16}–10^{20} V. As for the spectrum analysis via the observer sphere method (see section 5.1), $N = 5 \cdot 10^8$ protons are injected with a homogeneous distribution in the GP and an R^{-1} rigidity distribution in the range of 10^{16} V to 10^{20} V. The additional $N = 5 \cdot 10^9$ protons in the rigidity range 10^{17} V to 10^{20} V and $N = 10^{10}$ protons in the rigidity range $10^{17.5}$ V to 10^{20} V are also included with the weighed sum from all three rigidity ranges used to produce the total sky map. The sky maps for four equidistant rigidity bins from 10^{16}–10^{20} V are depicted in figure 5.7.

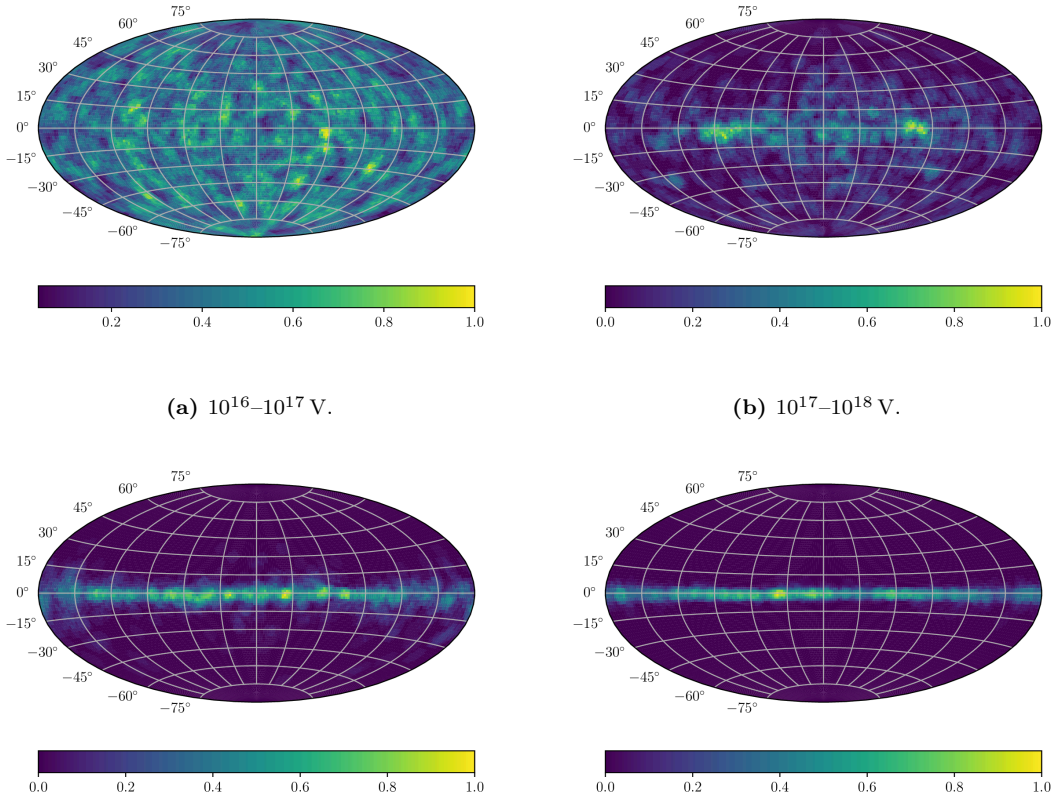

(a) 10^{16}–10^{17} V.

(b) 10^{17}–10^{18} V.

(c) 10^{18}–10^{19} V.

(d) 10^{19}–10^{20} V.

Figure 5.7: Arrival direction distributions of GCRs for various rigidity ranges.

As expected, the smearing of the arrival direction distribution is largest for the smallest rigidity bin, and points most undistortedly in the direction of the sources for highest rigidities. In the two intermediate-rigidity sky maps, the arrival direction distribution still points predominantly in the direction of the GP. The degree of isotropisation in the lowest rigidity bin is so high, that the arrival direction distribution appears consistent with isotropy. To assess this quantitatively, the normed longitude and latitude[6] distributions of the arrival directions are checked individually for consistency with isotropy via fitting of a

[6] More precisely, the cosine of the latitude is analysed, as this value is expected to have a flat distribution in the case of isotropy.

linear function to the data, and comparing the reduced χ^2 values for both the fit and the flat distribution expected for the case of isotropy. The distributions, as well as their respective fit results, are plotted in figure 5.8. Both distributions are consistent with isotropy, both visible in the values of the reduced $\chi^2_r(\mu)$ for the isotropic expectation, as well as in comparison with the reduced χ^2_r values of the linear fits.

These results can have consequences on the expected signal of the measured arrival direction distribution in case of a significant contribution of GCRs (or more precisely, CRs originating from the GP) to the flux for energies up to the "ankle". With the expected increase in the mean mass up to these energies (see section 5.2, in particular figure 5.5), the particle rigidities are as low as $10^{(18.5-\lg 26)}\,\mathrm{V} = 10^{17.1}\,\mathrm{V}$ in the case of iron, which is the rigidity when a correlation in the arrival direction with direction of the GP starts to become discernible (see figure 5.7). At lower energies, we therefore expect a fairly isotropic arrival direction distribution. However, the contribution from high-rigidity particles at energies up to the "ankle" would point distinctly in the direction of the GP, such that any measurable anisotropy should exhibit a directional correlation with the GP if the Galactic contribution is significant.

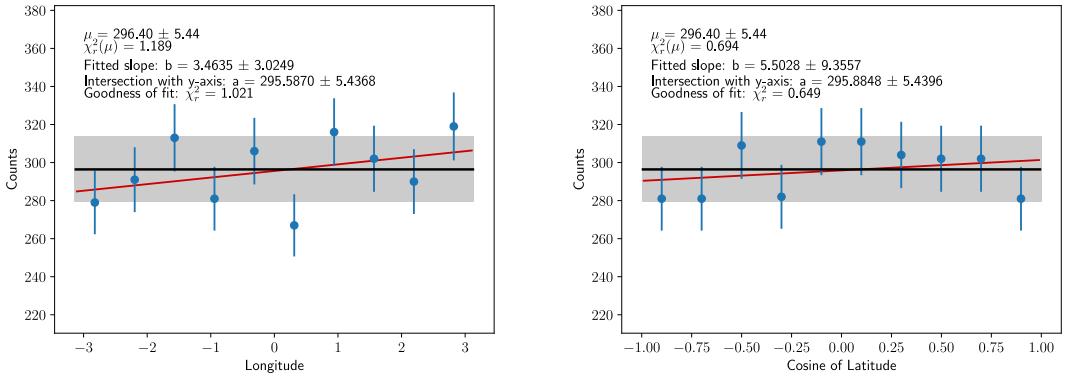

(a) Longitude distribution.

(b) Latitude distribution.

Figure 5.8: Longitude (left) and latitude (right) distributions in the arrival direction of GCRs in the rigidity range 10^{16}–10^{17} V; the black horizontal line signifies the expected number of events μ (indicated in the legend) for isotropy, and the red line the best linear fit; the reduced χ^2 for both isotropy and the linear fit are indicated in the legend ($\chi^2_r(\mu)$ and χ^2_r next to goodness-of-fit, respectively).

5.3.2 EGCRs

In the case of an isotropic injection of EGCRs we expect an isotropic arrival direction distribution at Earth in the field-free case. Thus, the study of the extragalactic flux provides a measure of the anisotropisation by the GMF. As for the spectrum analysis via the observer sphere method (see section 5.1), $N = 5 \cdot 10^9$ protons are injected with an R^{-1} rigidity distribution in the range of 10^{16} V to 10^{20} V. As for the case of GCRs, the sky maps for four equidistant rigidity bins from 10^{16}–10^{20} V are produced and are depicted in figure 5.9. Across all rigidities, the arrival direction distribution sky maps appear consistent with isotropy. The corresponding longitude and latitude distributions, analysed in the same way as for the GCR arrival directions, show the same result (see figure 5.10 for the entire rigidity range, and A4 for the rigidity ranges depicted in figure 5.9). This result has a straightforward consequence for the expected signal in the case of a dominant extragalactic contribution at certain energies: If the injected flux into the Galaxy is isotropic, so is the observed flux at Earth. The GMF does not have any inherent anisotropisation.

With this, the effect of the GMF on an anisotropic injection of EGCRs is still of interest, as we hereby test the degree of isotropisation of EGCRs. The objective is to test two main types of anisotropy. The first is a dipole, which is the largest-scale anisotropy that may be measured. The second is that from a point source, the strongest type of anisotropy that may be injected. This way, we test both whether any anisotropies survive and what their nature is.

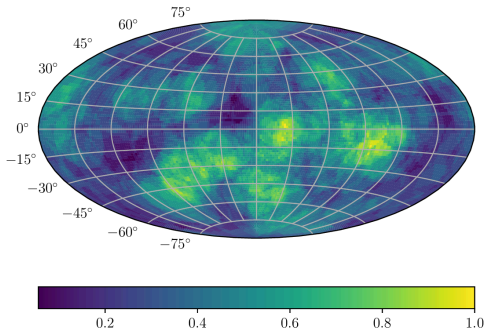

(a) $R = 10^{16}$–10^{17} V.

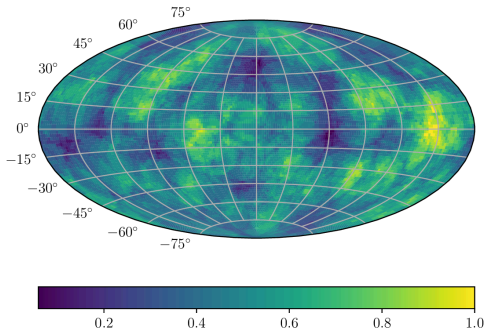

(b) $R = 10^{17}$–10^{18} V.

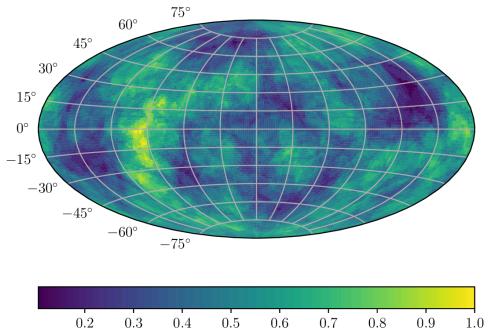

(c) $R = 10^{18}$–10^{19} V.

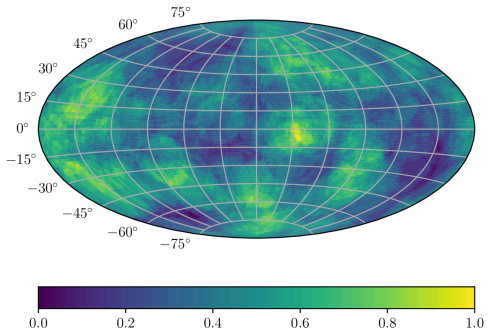

(d) $R = 10^{19}$–10^{20} V.

Figure 5.9: Arrival direction distributions of EGCRs for various rigidity ranges.

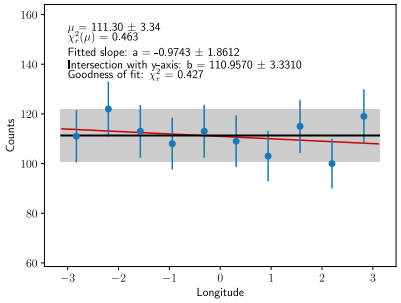

(a) Longitude distribution.

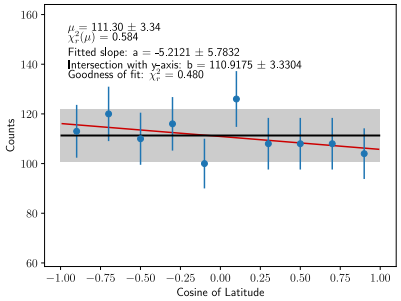

(b) Latitude distribution.

Figure 5.10: Longitude (left) and latitude (right) distributions of EGCRs for entire rigidity range; the black horizontal line signifies the expected number of events μ (indicated in the legend) for isotropy, and the red line the best linear fit; the reduced χ^2 for both isotropy and the linear fit are indicated in the legend ($\chi^2_r(\mu)$ and χ^2_r next to goodness-of-fit, respectively).

Several distributions are to be tested. For this we run into problems with our hitherto favoured forward-tracking approach, as simulating all distributions individually would require excessive simulation times. An alternative approach is to make use of the so-called Galactic lensing scheme [118], where the GMF is treated as a lens, transforming an injection to an arrival direction distribution via matrix multiplication (see equation 5.1).

$$\vec{A} = \vec{I} \cdot \mathcal{L}, \tag{5.1}$$

where $\vec{A}$ parametrises the arrival direction distribution, $\vec{I}$ the injection direction distribution and $\mathcal{L}$ signifies the Galactic lens.

This method rests on the assumption that the extragalactic sources are located at distances far exceeding the size of the Galaxy, such that the Galaxy can be viewed as a point. Therefore, positions at the edge of the Galactic sphere through which EGCRs enter the Galaxy can be ignored, and we get a coupling of injection and arrival directions. To calculate the lens $\mathcal{L}$, the matrix $\tilde{\mathcal{L}}$ assigning the injection and arrival directions to one another, is calculated via the injection directions into the Galaxy and arrival directions at Earth of a sufficiently large number of particles. The injection and arrival directions are discretised into HEALPix pixels[7], corresponding to the row (injection direction) and column (arrival direction) of the matrix $\tilde{\mathcal{L}}$. Finally, the lens $\mathcal{L}$ is retrieved by scaling the matrix via its 1-norm to conserve the flux[8] ($\mathcal{L} = \tilde{\mathcal{L}}/|\tilde{\mathcal{L}}|_1$). Another way to express the functionality of the lensing technique is that the injection distribution of an isotropic arrival direction (the lens) is scaled with an injection distribution of choice, such that the arrival direction is modified. With the lens, the arrival direction distribution of any injection direction distribution can be calculated without the need of re-simulation.

While the Galactic lens scheme is already implemented in CRPropa, inherited from PARSEC [118], it is not suitable for our purposes as it only covers the rigidity range 10^{18}–10^{20} V. Thus, the creation of custom lenses for the entire range of interest (i.e. $\leq 10^{16}$–10^{20} eV) is necessary.

In principle, the injection and arrival direction data gathered in the scope of our foward-tracking analysis of the modification of CR observables due to propgation in the GMF (see chapter 5) could be used to create our custom lens. However, with only ≈ 300 particles crossing the smallest observer shell centered at Earth, statistics is not large enough to test any smaller-scale anisotropies, such as point sources. Further simulations are computationally not feasible particularly for smallest rigidities, and increasing statistics via further choosing larger observer sphere gives rise to artefacts in the flux (see figure 5.3).

If time-reversibility can be assumed, the lens could be created via backward tracking of anti-protons that are isotropically injected into the Galaxy from Earth. These are backward tracked to the edge of the Galaxy and the injection direction from Earth and the arrival direction at the edge of the Galactic shell are measured for each anti-particle. This way, we only have trajectories that connect the edge of the Galaxy with Earth. Assuming time-reversibility of the particle trajectories, the inverted directions correspond to the injection direction into the Galactic shell, and the corresponding arrival direction at Earth. We arrive at the injection direction distribution into the Galaxy that leads to an isotropic arrival direction distribution at Earth. While the flux and isotropy are conserved, as expected for isotropic injection, this assumption may still not be valid. To test its validity, and sufficiently confirming Liouville's theorem, we compared the distribution of injection directions forward tracked protons that reach Earth with the reversed arrival directions at the edge of the Galaxy of backward tracked anti-protons. The resulting sky maps for the entire rigidity range 10^{16}–10^{20} V are depicted in figure 5.11 (in Appendix A5 the same skymaps subidivided into four equidistant rigidity ranges are depicted to check for consistency across rigidity). Indeed, the skymaps appear very similar, consistent with time-reversibility. The backward-tracking approach for lens creation for be applied with reasonable confidence.

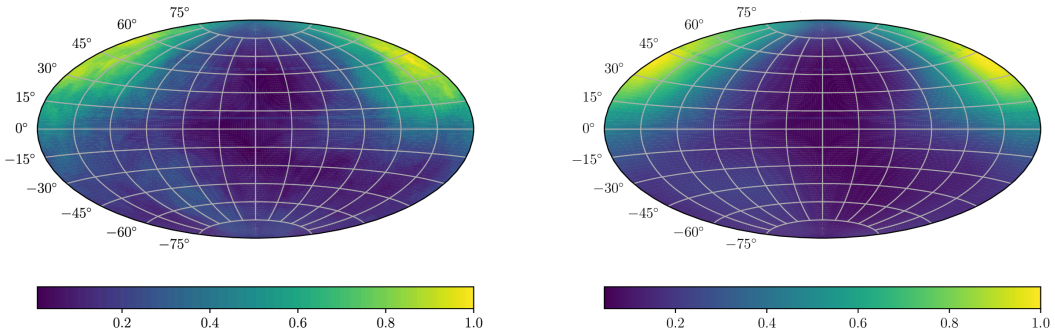

Figure 5.11: Left: Injection direction distribution of forward-tracked protons injected at the edge of the Galaxy with a Lambertian distribution that arrive at Earth. Right: Reversed arrival direction distribution of backward-tracked anti-protons injected from Earth istropically arriving at the edge of the Galaxy for the rigidity range 10^{16}–10^{20} V.

To create the lens, $5 \cdot 10^7$ anti-protons in the rigidity range 10^{16}–10^{20} V injected from Earth isotropically

[7] HEALPix (acronym for **H**ierarchical **E**qual **A**rea iso**L**atitude **Pix**elisation) pixelisation is a way of discretising a 2D-sphere into equal area solid angle regions. A commonly used projection in cosmology and astrophysics is to map the sphere onto twelve diamond-shaped facets, i.e. the sphere is parametrised via a rhombic dodecahedron. The granularity is achieved by subdividing these facets into smaller segments by powers of two, signified by the quantity $n_{\text{side}} = 2, 4, 8, 16, ...$ The resulting number of pixels equals $n_{\text{pix}} = 12 \cdot n_{\text{side}}^2$ [125].

[8] For rigidity-dependent lenses, the maximum 1-norm of all individual lenses is chosen as the scaling factor.

with a R^{-1} spectrum were backtracked to the edge of the Galaxy. As for the Galactic lenses implemented in CRPropa, the number of sides for HEALPix pixelisation is set to $n_{\text{side}} = 64$, corresponding to a total of $n_{\text{pix}} = 12 \cdot 64^2 = 49152$ pixels. The CRPropa lens further discretises the rigidity, to acquire rigidity-dependent lenses. These are also employed for our lenses with a logarithmic rigidity bin width set to $\lg(E/\text{V}) = 0.2$. Using these parameters, we get an expected number of particles per rigidity bin per pixel of $5 \cdot 10^7 / 49152 \cdot 20 \approx 51$ with a relative error of $1/\sqrt{(51)} \approx 14\,\%$ if isotropy is assumed. This value will function as the uncertainty of the lens.

To test the performance of the custom lens, an isotropic injection direction distribution of 10^6 protons in the rigidity range 10^{16}–10^{20} V with a R^{-1} is lensed. The resulting arrival direction distribution and rigidity spectrum is plotted in figure 5.12.

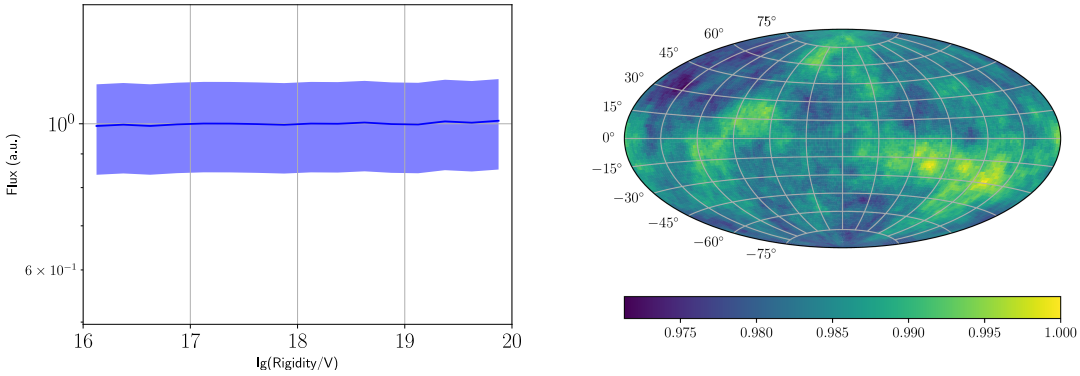

Figure 5.12: Spectrum (left) and arrival direction distribution (right) of 10^6 isotropically injected protons in the rigidity range 10^{16}–10^{20} V with a R^{-1} to test the custom Galactic lensed.

The resulting flat spectrum and isotropic arrival direction distributions are consistent with our expectations, verifying the efficacy of the lens. Not only can this lens calculate the arrival direction distribution for any injected distribution, but as a collection of rigidity-dependent sublenses, it also allows us to investigate possible flux modifications of anisotropic fluxes.

With reasonable confidence that the created lens performs as expected, we can apply it to anisotropic injection direction distributions. For the dipole scenario, we chose two injection direction distributions with respect to Galactic longitude l. One is centered around $l = 180° = \pi$, where the Galaxy is most transparent, and the other is rotated by 180 °, i.e. $l = 0$. This way, we have an estimate of the uncertainty of the strength of the isotropisation by the GMF. For the single point-source scenario, we test four distributions. One is from the direction of maximal and of minimal Galactic transparency each (see figure 5.11), one from the anti-centre, and one from the direction of Centaurus A, which is roughly the direction where previous source identification analyses of arrival direction distributions by the Auger Collaboration have found the highest flux weights [60]. While the point-sources are expected to yield the highest anisotropy after lensing, they suffer from higher statistical uncertainty, as the number of entries per pixel is quite small, especially from directions where the Galaxy is most opaque. To remedy this to some degree, we smear the injection distribution via Gaussian smearing with a smearing angle of 5 °. The injected spectrum for each distribution is R^{-1} in the rigidity range 10^{16}–10^{20} V. The corresponding injection direction distributions and the resulting arrival direction distributions for the dipoles are depicted in figure 5.13, and for the point sources in figure 5.14.

The amplitude distributions of the arrival direction distributions in multipole moments of both distributions are presented in figures 5.15 and 5.16, respectively. The 99 %-confidence interval is calculated as the 2.576-fold of the median amplitude amplitude of moments $l >= 10$. This choice is based on the expectation that highest-order moments are zero for all distributions, allowing us to treat non-zero values as statistical fluctuations[9].

We find that the dipole moment is drastically reduced after lensing. For the injected dipoles, the amplitude drops to $(3.0 \pm 0.1)\,\%$ for $l = 0$ and $(1.1 \pm 0.1)\,\%$ for $l = \pi$. In the single-point source scenario, we find that only the remaining anisotropy after lensing is that of a dipole. The dipole amplitudes generally have higher values compared to the dipole scenario with $(10.9 \pm 0.1)\,\%$ for Centaurus A, $(2.4 \pm 0.1)\,\%$ for the direction of highest Galactic transparency, $(15.2 \pm 0.1)\,\%$ for the Galactic centre, and $(2.1 \pm 0.1)\,\%$ for the Galactic anti-centre. We see that the GMF largely isotropises the dipole.

[9] We justify this assumption on the observation that the amplitude for moments $l > 1$ of the injection direction distribution, which would yield zero amplitude as a pure dipole, is in the order of a few per mille and up to a per cent, which must therefore be considered consistent with zero.

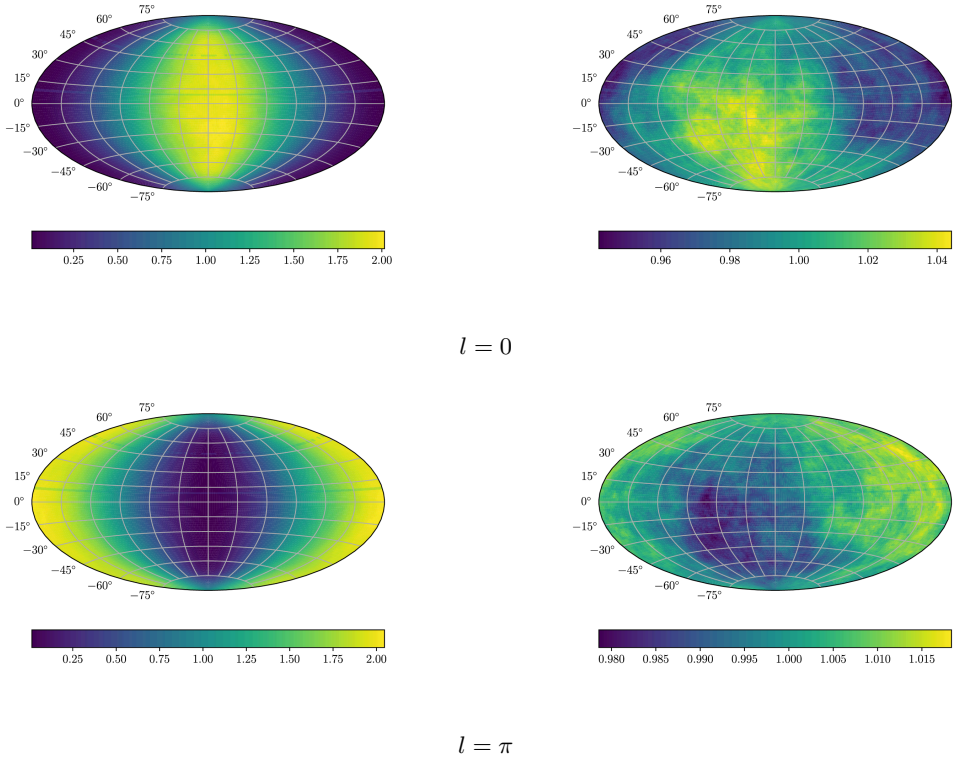

Figure 5.13: Injection direction (left) and arrival direction (right) distributions of protons injected with a dipole distribution with an R^{-1} spectrum in the rigidity range 10^{16}–10^{20} V.

To parse the degree of this isotropisation with respect to rigidity, the lensed distributions in arrival direction and multipole moments are shown for four rigidity bands of varying width in Appendix A6 to A11. We find that the entire remaining dipole amplitude stems from the highest-rigidity rigidity window(s), above at least $10^{18.5}$. For the lower-rigidity particles, the amplitude after lensing is $\lesssim 1\,\%$, consistent with isotropy with the precision of our lenses. The dipole is essentially fully isotropised for rigidities below at least 1 EV. In other words, any directional information of a particle is lost during propagation in the GMF below this rigidity.

Given the shift in the position of highest Galactic opacity (or transparency) with rigidity (see figure A5), the GMF may impose spectral modifications on anisotropically injected EGCRs. The spectra for both dipoles of the lensed distribution across the entire rigidity range are shown in figure 5.17, and for the single point-source distriubtions in figure 5.18. For injected dipoles, we see a flux modification that appears to have a power law dependence. The magnitude and sign of the corresponding slope depends on the direction of the dipole. The slope of the injection spectrum is modified by $R^{-0.033\pm0.001}$ for $\varphi_0 = 0$, and $R^{0.013\pm0.001}$ for $\varphi_0 = \pi$; this a extremely slight spectral modification, yet significant. For the single point-source scenarios, we found a more complicated flux modification with inflection points at EV-level. Injections from Centaurus A and the Galactic centre show a similar trend with rigidity for low rigidities, as the dipole centered at $l = \pi$, whereas injections from the other two sources correspond to the trend for $l = \pi$. For the former two, the inflection corresponds to a hardening of the spectrum, as is the "ankle" feature of the CR energy spectrum, indicating that deflections in the GMF of anisotropic injections might help explain the features we see in the spectrum up to highest energies.

A further question which arises is, whether such a modification can be measured, and if so, how strong the injected anisotropy would have to be. This question depends on the statistics of the experiment measuring the flux, which is tied to the expected spectrum. Current resolution of spectral features in the energy spectrum measured by the Pierre Auger Observatory is in the order of $\Delta\gamma_{\mathrm{stat}} \approx 0.03$ statistical uncertainty and $\Delta\gamma_{\mathrm{sys}} \approx 0.07$ systematic uncertainty [2], larger than the spectral modification of the lensed dipoles, but smaller than for point sources. The degree of spectral modification depends on the degree of anisotropy in the injected flux. It therefore remains unclear as to the extent to which flux modifications would measurably manifest in data. The visibility of modifications of anisotropies due to propgation in the GMF in data is explored in [126]. Also using the Galactic lensing scheme, but for post-"ankle" energies, and the JF12 model as the their GMF model, they investigate visibility of modifications imposed by the GMF in the dipole and quadrupole anisotropy considering data from the Pierre Auger Collaboration.

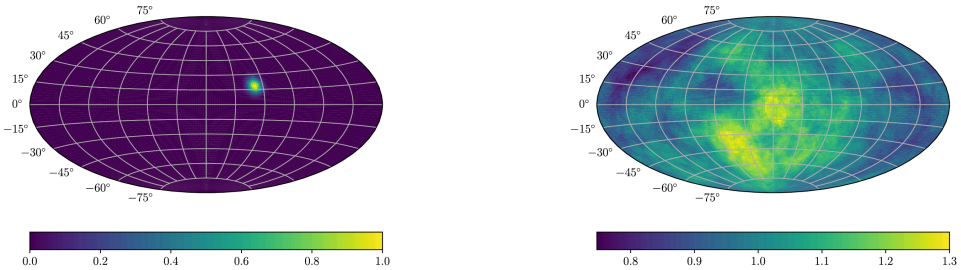

Centaurus A

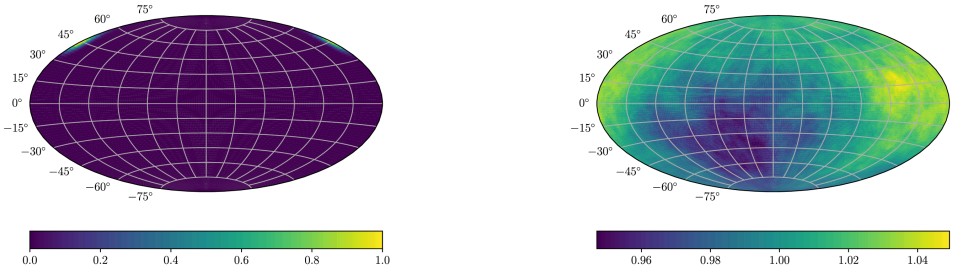

Maximum Galactic transparency

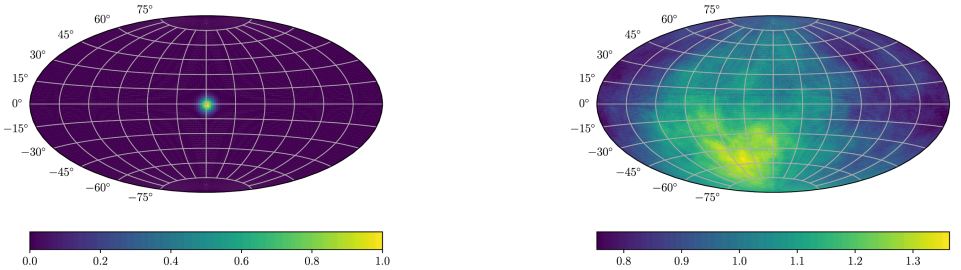

Maximum Galactic opactiy/Galactic centre

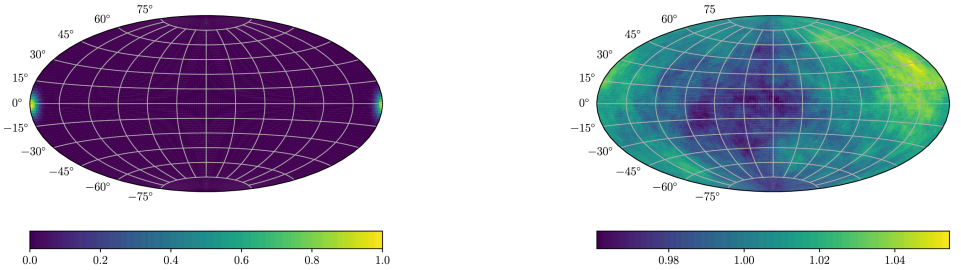

Galactic anti-centre

Figure 5.14: Injection direction (left) and arrival direction (right) distributions of protons injected from point sources with an R^{-1} spectrum in the rigidity range 10^{16}–10^{20} V.

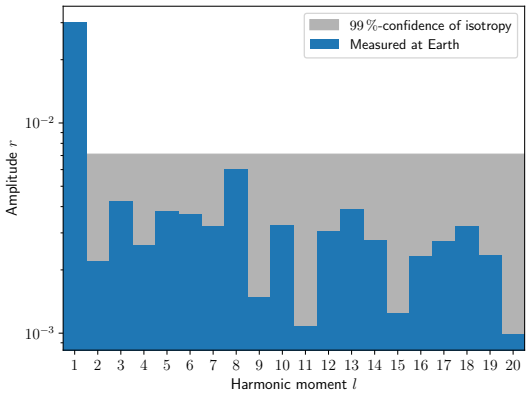

(a) $l = 0$

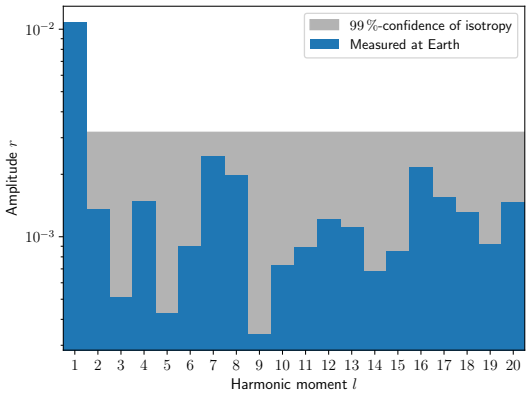

(b) $l = \pi$

Figure 5.15: Amplitude of each multipole moment for injected dipole distribution of protons injected with an R^{-1} spectrum in the rigidity range 10^{16}–10^{20} V.

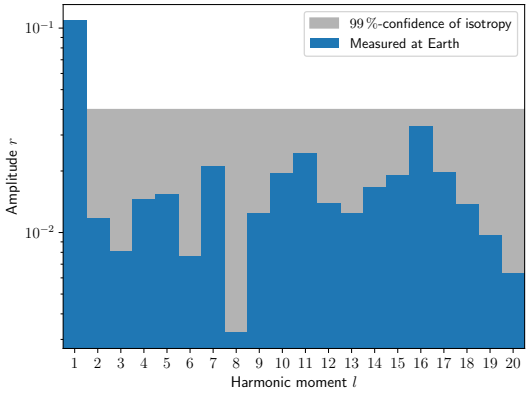

(a) Centaurus A

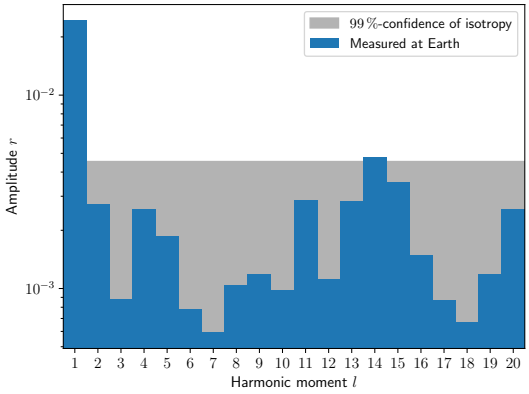

(b) Maximum Galactic transparency

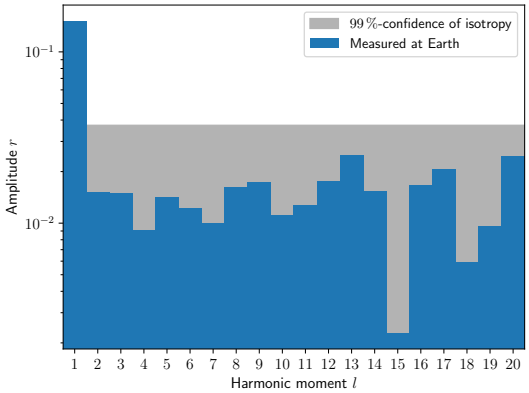

(c) Maximum Galactic opactiy/Galactic centre

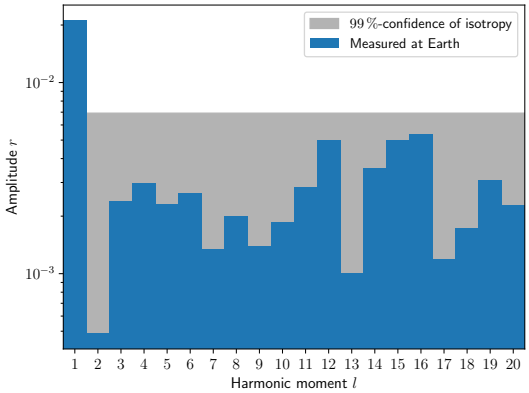

(d) Galactic anti-centre

Figure 5.16: Amplitude of each multipole moment for various injected single point-source distributions of protons injected with an R^{-1} spectrum in the rigidity range 10^{16}–10^{20} V.

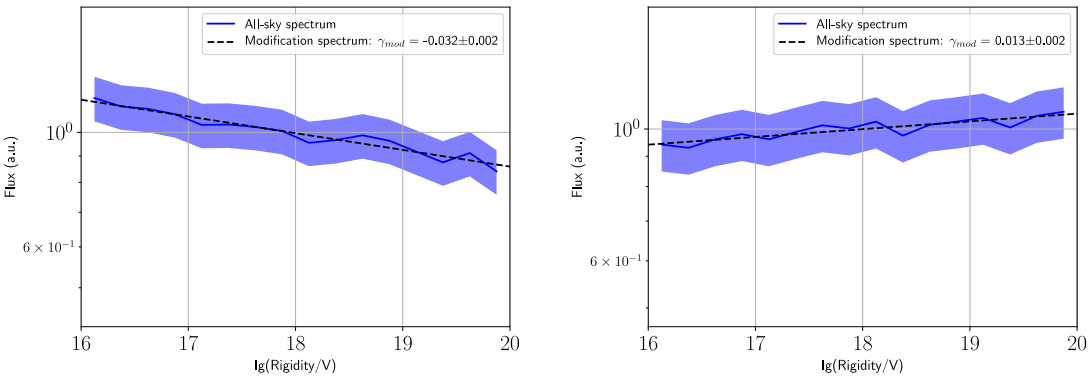

(a) $\varphi_0 = 0$ **(b)** $\varphi_0 = \pi$

Figure 5.17: Lensed spectrum for an injected dipole distribution of protons injected with an R^{-1} spectrum in the rigidity range 10^{16}–10^{20} V.

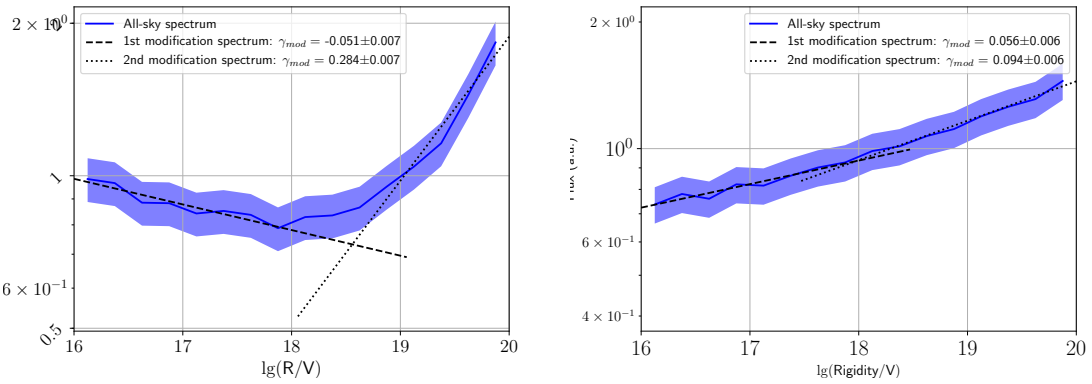

(a) Centaurus A **(b)** Maximum Galactic transparency

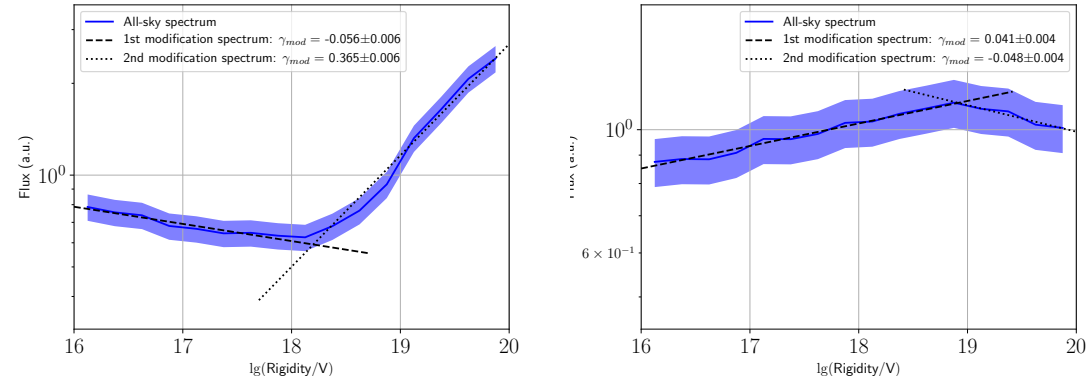

(c) Maximum Galactic opactiy/Galactic centre **(d)** Galactic anti-centre

Figure 5.18: Lensed spectrum for various injected single point-source distributions of protons injected with an R^{-1} spectrum in the rigidity range 10^{16}–10^{20} V.

Chapter 6

The influence of the propagation on the transition from Galactic to extragalactic cosmic rays

In chapter 5, we presented the observable effects that the GMF imposes CRs of both Galactic and extragalactic origin. These have certain implications on the transition from GCRs to EGCRs that will be discussed in the following. We start by discussing both contributions separately and finally use the insights to discuss the combined contribution.

6.1 GCRs

The most prominent propagation effect of GCRs is the flux suppression with increasing rigidity resulting from the decreasing confinement of GCRs in the GP. Such a "knee"-like feature in turn leads to a modification of the composition in the form of an increased mean mass all the way up to "ankle" energies. Both of these features, place constraints on the contribution of GCRs injecting into the GP (henceforth referred to as GP-GCRs) up to energies significantly above the "knee" as they are in conflict with measured data. The additional increasing correlation in the arrival direction distribution with the source locations (i.e. the direction of the GP) further disfavours such a contribution. Alternative Galactic contributions are favoured where GCRs do not originate directly from the GP but are re-accelerated outside the GP and re-enter the GP afterwards on their voyage to Earth. One such example is re-acceleration in Galactic wind termination shocks (GWTSs). For such CRs, the propagation effects that the GMF imposes resemble more those of EGCRs.

Although the flux suppression arising due to propagation alone already qualitatively resembles the "knee", we still expect a cut-off in the source spectrum. Independent studies of DSA at SNRs predict maximum rigidities at energies around the "knee". In fact, based on these results, the onset of the flux suppression due to propagation is at higher energies than the "knee". This implies that, if the "knee" predominantly arises from propagation effects in the GMF, the JF12 model underestimates that strength of the GMF. This is not likely. On the one hand, we found that the JF12 appears to produce slightly higher values for residence times of GCRs in the Galaxy (see figure 4.13a). On the other hand, other studies have even concluded that the JF12 overestimate the random component [127]. If propagation effects of GP-GCRs are to play a significant role, an additional accelerator in the GP must be invoked that could accelerate GCRs efficiently to energies beyond the "knee", such as Wolf-Rayet stars. What can be claimed with reasonable confidence is that propagation effects in the GMF lead to a further suppression of the source spectrum and a modification of the composition towards heavier nuclei. The degree of the shift depends on the details of the source properties, such as the maximum acceleration rigidity.

6.2 EGCRs

Propagation effects in the GMF only arise for EGCRs if they are injected anisotropically into the Galaxy. In addition, the nature of the anisotropy plays a key role in the expected effects on the flux. A large-scale anisotropy, such as a dipole, modifies the flux via a change in the spectral slope, whereas small-scale anisotropies, such as point sources, can lead to spectral breaks in the rigidity range of a few EV. Especially noteworthy is that the injection from the direction of Centaurus A leads to a hardening of the spectrum, very similar in location and shape to that of the "ankle" for light nuclei. This may partly tie the occurrence of the "ankle" to propagation effects in the GMF that arise from the change in propagation regimes with

rigidity. The strong isotropisation for rigidities smaller $\approx 1\,\mathrm{EV}$ to beyond the percent-level are consistent with large-scale anisotropy data at energies below the "ankle" (see figure 2.5).

The degree to which EGCR observables are modified depends on the strength of the injected anisotropy. The results presented are a consequence of *pure* anisotropies, i.e. no isotropic component to the injected flux. For more realistic fluxes with both an isotropic and anisotropic component, the measured anisotropy and flux modifications due to propagation in the GMF are weaker than found here. To this end, gauging the degree anisotropy of the injected flux is essential to estimating the contribution of propagation effects.

An important point to raise in the context of EGCRs pertaining to our findings for GCRs is that the flux suppression of GCRs towards higher rigidities can also be translated into an increased leakage out of the Galaxy. The amount of leakage from their host galaxies contributes to the expected low-energy flux of EGCRs originating from certain galaxy classes, such as SBGs or AGN. Such a leakage would manifest in the form of a flux suppression towards lower rigidities, as confinement in the host galaxies increases in said direction. The EGCR flux from galaxy clusters may not follow such a trend, as they have no host galaxy to escape from. An additional aspect from the study of GCR sources that is relevant for EGCRs is GWTSs. Provided they can efficiently accelerate GCRs to post-"knee" energies, they can potientially also be a source of lower-energy EGCRs. The difference is that GCRs from GWTSs diffuse back to the Galaxy after re-acceleration, whereas EGCRs from GWTSs are the ones that leak out of their host galaxies after re-acceleration.

6.3 Combined flux

While it is useful to understand the propagation effects of the GMF individually for GCRs and EGCRs in order to intuit the constraints and requirements this sets on the injection flux and spectrum of each component, only the sum of both contributions with realistic injected fluxes may elucidate the total modifications we expect. The modification the GMF imposes specifically on GCRs depends primarily on the maximum rigidity of the sources and their location (mainly whether they are situated in the GP or outside). The larger the maximum rigidity, the larger the influence of propagation in the GMF to GCR observables. The source locations determine which type of modification is expected. The degree and nature of the injected anisotropy of EGCRs determines their expected modification that the GMF imposes on them.

Chapter 7

Summary and conclusions

In this thesis, we explored the propagation effects that the GMF imposes on CRs in the rigidity range matching the energy of the transition region from GCRs to EGCRs of protons. Our main objective was to study how they modify observables in CR detection, namely the spectrum, composition and arrival direction. We found that this rigidity range also signifies a change in propagation regimes from diffusive to ballistic propagation (see figure 4.1). Ballistic propagation (i.e. propagation with large rigidities, or in the weaker fields outside of the GP) is characterised by largely unperturbed trajectories, whereas for diffusive propagation, CRs are deflected to such a degree that they not only follow random trajectories, but potentially also undergo collision-like processes during propagation. Using several parameters to illustrate and quantify the propagation effects, namely the deflection angle, the trajectory length, and volume fraction coverage, we found that a plausible picture emerges tying observed propagation features to the structure or topology of the GMF (see chapter 4). The GP, where the magnetic field is strongest and deflections are largest, plays a significant role in this picture, as diffusive propagation sets in earliest as particle rigidity decreases in this region of the Galaxy. As the rigidity falls below an inflection point, where the corresponding gyro radius (remember $r_g \propto {}^{R}/_{B}$) becomes shorter than characteristic length scales of the Galaxy, namely the radius and width of the GP of a few to tens of kpc (recall figure 4.1), particles propagate a significant fraction of the total propagation time in the GP, leading to a break in the rigidity dependence of the aforementioned parameters as observed (see figures 4.3 to 4.6, in particular).

These propagation features additionally result in large-scale effects. EGCRs experience a shielding effect from the GP for decreasing rigidities, where they are reflected by the strong GMF therein. At the same time, those that penetrate into the GP are concentrated more strongly therein due to their increasingly diffusive propagation. GCRs originating in the GP, or GP-GCRs, experience a confinement effect for small rigidities due to their diffusive propagation, which weakens as rigidity increases. In an attempt to combine these large-scale effects in one analysis scheme, we performed a steady-state analysis of the particle count in the GP for both GCRs and EGCRs (see section 4.3.3). We found a clear decrease in counts with rigidity for GCRs stemming from the decreased confinement in the GP. The EGCR count, that exhibits a dip at intermediate rigidities, yielded an inconclusive picture with respect to the expected effect of the GMF on the EGCR flux.

To study the effects on CR observables, we performed computationally intensive forward-tracking simulations to observer spheres of various sizes around the position of Earth in the Galaxy and recorded the number, rigidity and arrival directions of particles crossing the sphere shells (see chapter 5). As expected from the steady-state analysis, the GCR flux showed an unambiguous flux suppression with rigidity. However, the degree of suppression was not conclusively determined, but expected to be in the same order of magnitude of the smallest sphere sizes given their size with respect to the particle's local gyro radius. For the case of EGCRs, we found a conservation of both flux and isotropy at the observer in case of isotropic injection. Along with an explicit validation of the time-reversibility of CR trajectories, we could confirm the applicability of Liouville's theorem, despite hints calling this into question. This also showed that shielding and confinement exactly cancel.

In addition to the flux modification, the observer sphere method enabled the investigation of composition changes by applying the flux modification to an injected composition of different particle species with differing charges $Z\,e$. This was done by superimposing the spectra of various nuclei retrieved from the rigidity spectrum (i.e. a scaling via an initial flux and an energy shift, such that $E = Z\,e \cdot R$). As no flux modification was found for EGCRs, the composition analysis was only performed for GCRs, where an increasing contribution of intermediate-mass to heavy nuclei was found up to EeV energies.

We further investigated the effects of the GMF on the arrival direction distribution of CRs (see section 5.3). Using the observer sphere method, we found that the arrival direction distribution for GCRs showed a measurable anisotropy correlated with the direction of the GP for rigidities above 0.1 EV. For EGCRs, we studied the effects that the GMF imposes on anisotropically injected EGCRs via the Galactic lensing

technique. Here, we found that injected dipoles are isotropised to below the 1 %-level below $10^{18.5}$ V. This rigidity is in the same order of magnitude as the inflection rigidities discussed above, where breaks in the rigidity dependence occur for the parameters used to quantify the propagation effects.

This work strongly suggests that the effects of CR propagation in the GMF on the spectrum, composition and arrival directions needs to be taken into account in the energy range signifying the transition from GCRs to EGCRs. We showed that this can be tied to the fact that the transition in propagation regimes from diffusive to ballistic also occurs in this energy range. While for GCRs, the main process that takes effect is the decreased confinement, EGCRs are affected more subtly via the directional shift in the GMF transparency.

Our work can be expanded upon most concretely by making more realistic assumptions about the source distribution and spectra. Particularly the effect of a discrete GCR source distribution may lead to additional or entirely new effects. Gauging the degree of expected anisotropy of EGCRs injected into the Galaxy is of special importance for understanding the effect that propagation in the GMF may have on CRs. Additionally, this work employs the ballistic propagation scheme of CRPropa where the equation of motion is solved. A complementary analysis using diffusive propagation solving the transport equation is particularly crucial to check the validity of our findings at low energies, but also to estimate at which energy diffusive and ballistic propagation must be assumed, respectively. Lastly, the effect of interactions, especially nuclear interactions during propagation, must be accounted for to get a full picture of the propagation effects in the Galaxy. These would mainly be of importance at lowest rigidities, possibly below the minimum rigidity employed for this work.

Appendix: Additional figures

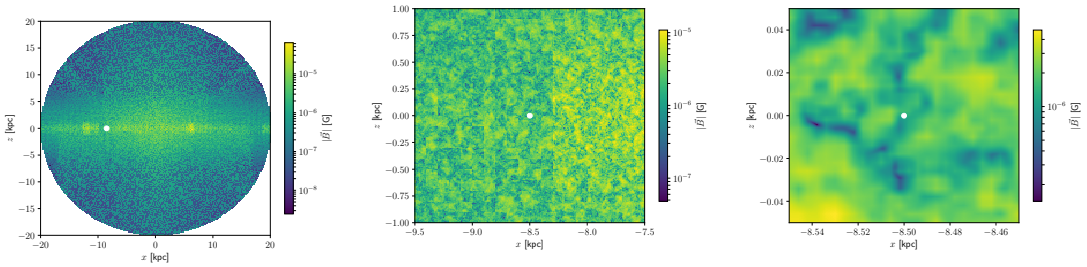

(a) Entire Galactic extent of x and z. **(b)** ± 1 kpc section in x and z around Earth. **(c)** ± 50 pc section in x and z around Earth.

Figure A1: Sections of the x-z cross section at $y = 0$ in Galactic coordinates of the magnitude of the GMF (white dot signifies location of Earth).

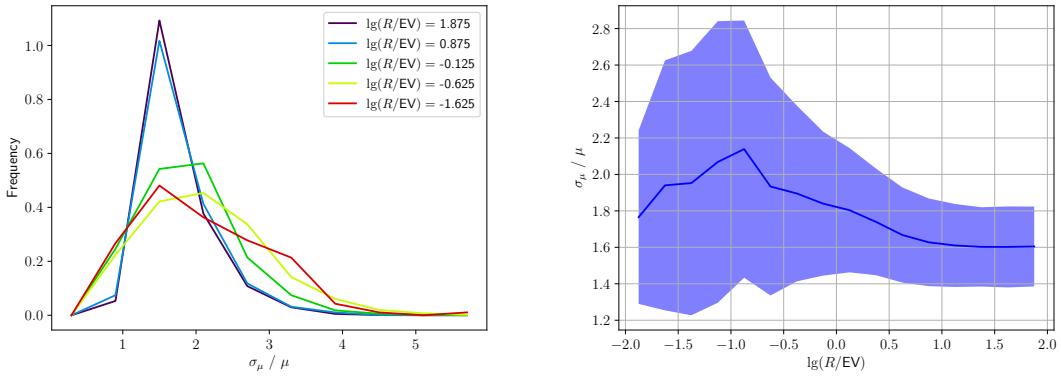

(a) r_μ distribution for different rigidities signified in the legend. **(b)** Median of r_μ as a function of rigidity. The spread is quantified via the median absolute difference.

Figure A2: Dependence of r_μ on rigidity for a cylinder radius of 19 kpc.

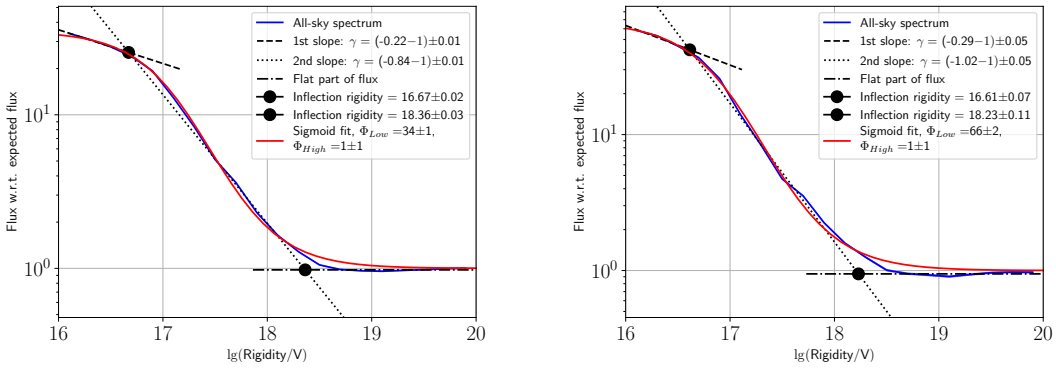

(a) $R_{\text{obs}} = 0.1\,\text{kpc}$.

(b) $R_{\text{obs}} = 0.05\,\text{kpc}$.

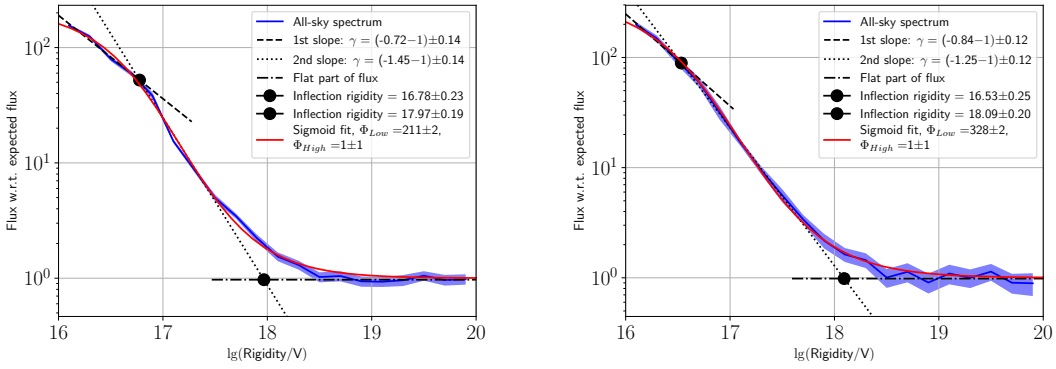

(c) $R_{\text{obs}} = 0.01\,\text{kpc}$.

(d) $R_{\text{obs}} = 0.005\,\text{kpc}$.

Figure A3: Linear and sigmoid fits ($f(x) = A/(1 + \exp((x - C)/B)) + D$) to the rigidity spectra of GCRs (in log-log).

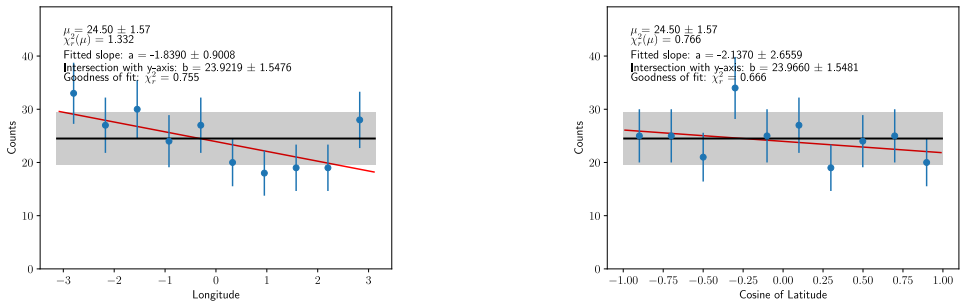

$R = 10^{16}$–10^{17} V.

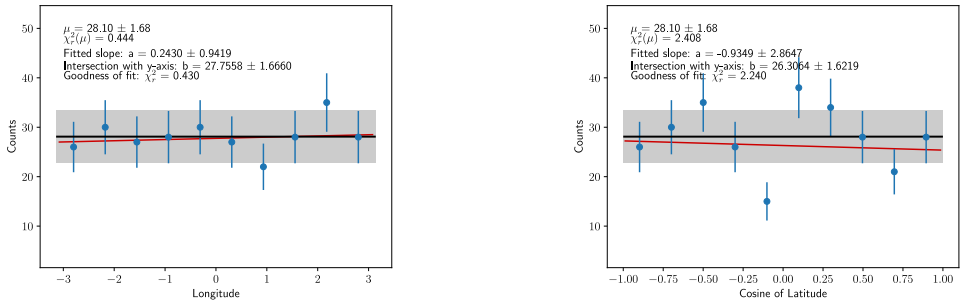

$R = 10^{17}$–10^{18} V.

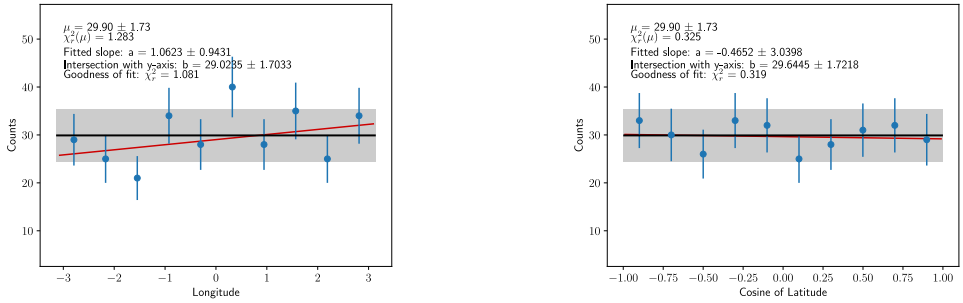

$R = 10^{18}$–10^{19} V.

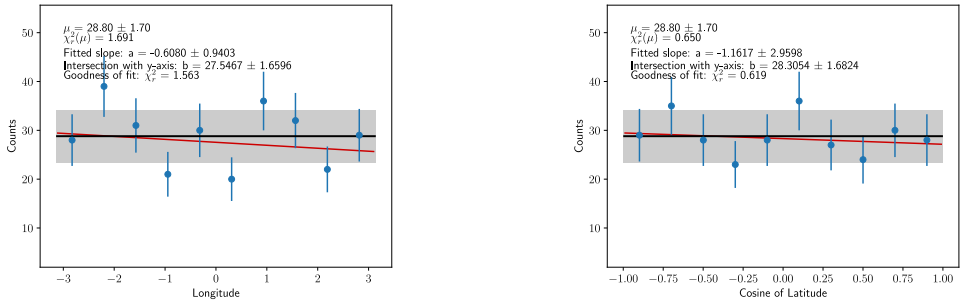

$R = 10^{19}$–10^{20} V.

Figure A4: Longitude (left) and latitude (right) distributions for various rigidity ranges (see subfigure titles); the black horizontal line signifies the expected number of events μ (indicated in the legend) for isotropy, and the red line the best linear fit; the reduced χ^2 for both isotropy and the linear fit are indicated in the legend ($\chi^2_r(\mu)$ and χ^2_r next to goodness-of-fit, respectively).

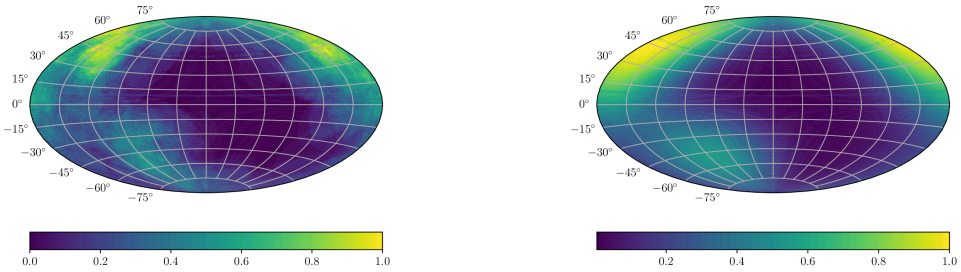

10^{16}–10^{17} V.

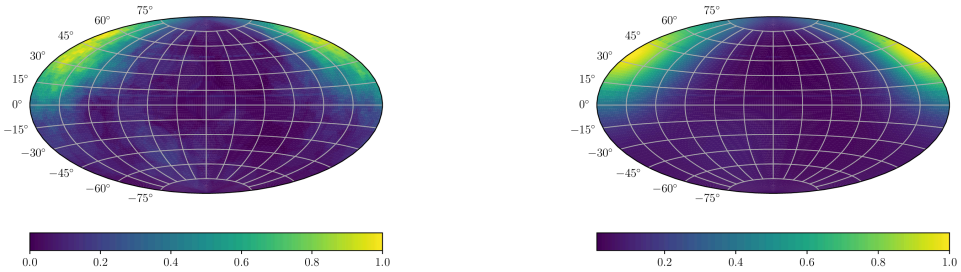

10^{17}–10^{18} V.

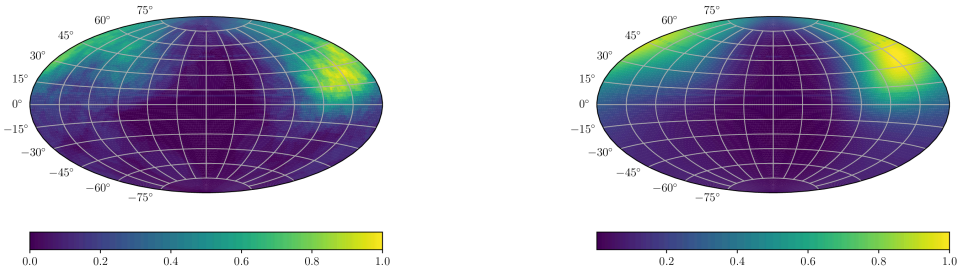

10^{18}–10^{19} V.

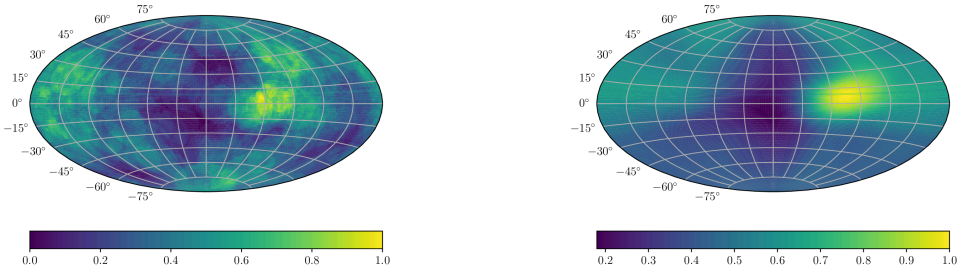

10^{19}–10^{20} V.

Figure A5: Left: Injection direction distribution of the protons injected at the edge of the Galaxy with a Lambertian distribution that arrive at Earth. Right: Reversed arrival direction distribution anti-protons injected from Earth istropically arriving at the edge of the Galaxy for the four equidistant rigidity bands in the range 10^{16}–10^{20} V.

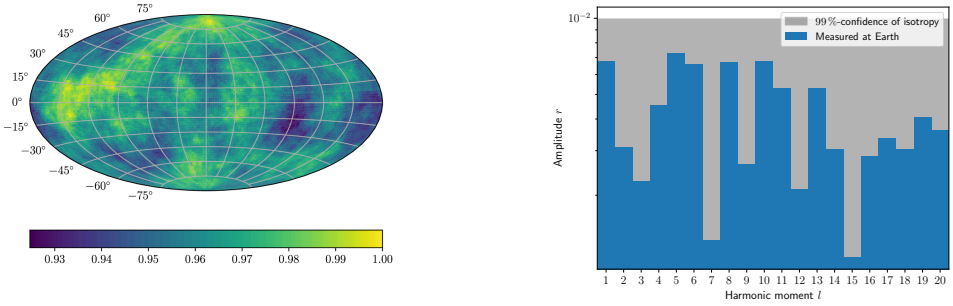

$10^{16} - 10^{18}$ V.

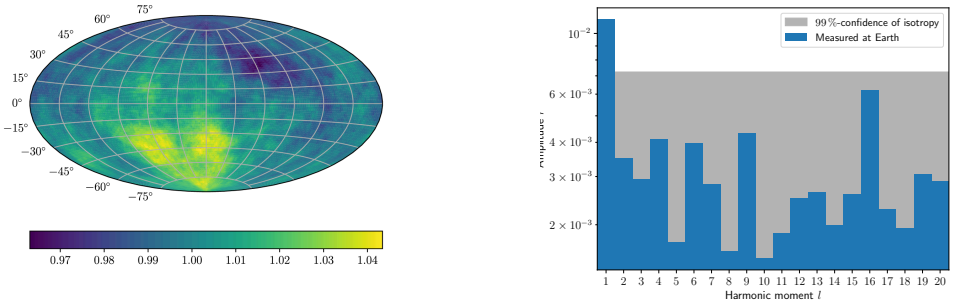

$10^{18} - 10^{18.5}$ V.

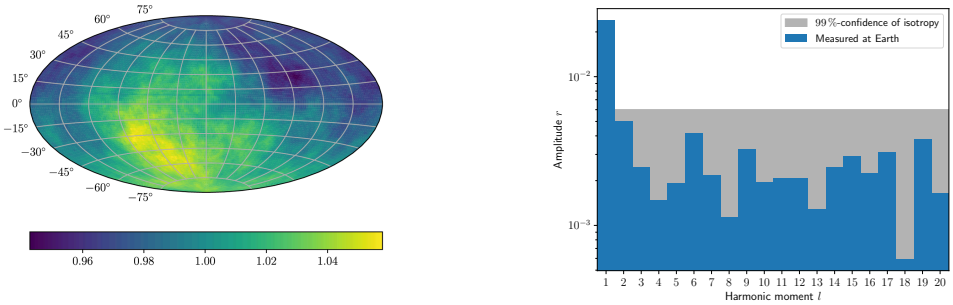

$10^{18.5} - 10^{19}$ V.

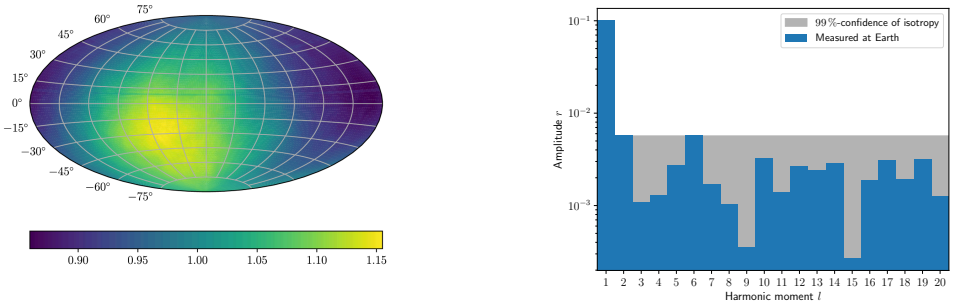

$10^{19} - 10^{20}$ V.

Figure A6: Arrival direction (left) and multipole amplitude (right) distributions of protons injected with a dipole w.r.t $\varphi_0 = 0$ with an R^{-1} spectrum in four rigidity windows indicated in each sub-figure.

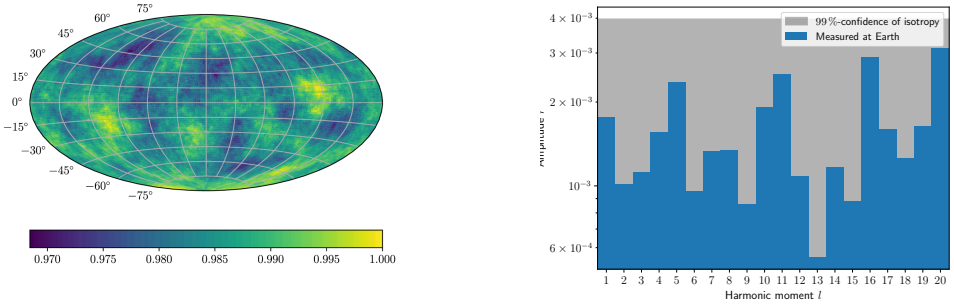

$10^{16} - 10^{18}$ V.

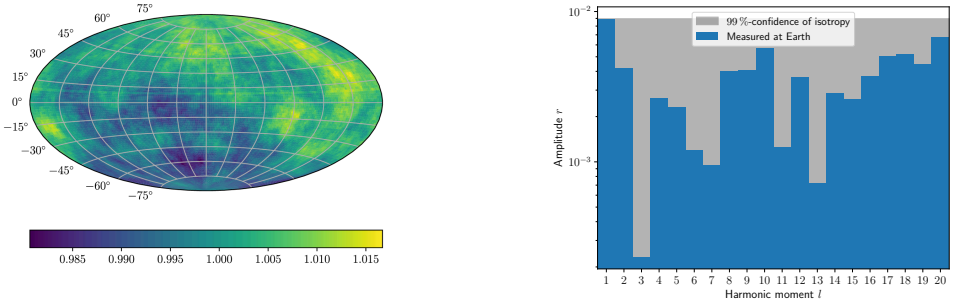

$10^{18} - 10^{18.5}$ V.

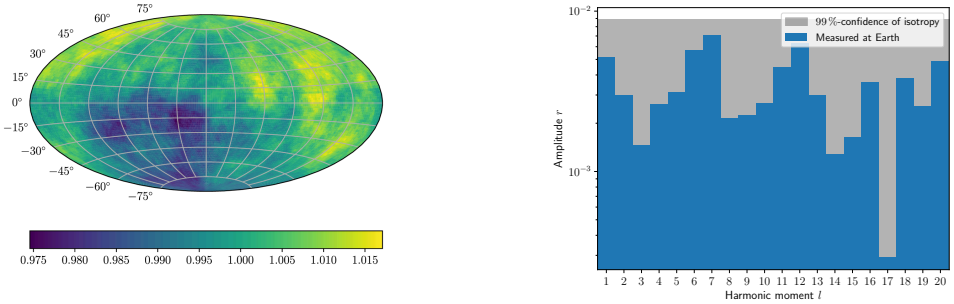

$10^{18.5} - 10^{19}$ V.

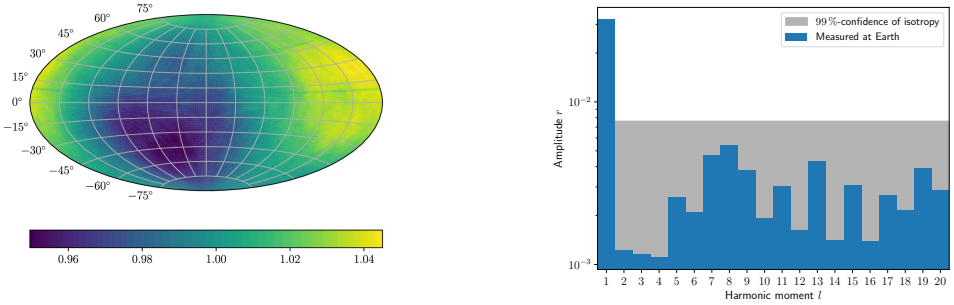

$10^{19} - 10^{20}$ V.

Figure A7: Arrival direction (left) and multipole amplitude (right) distributions of protons injected with a dipole w.r.t $\varphi_0 = \pi$ with an R^{-1} spectrum in four rigidity windows indicated in each sub-figure.

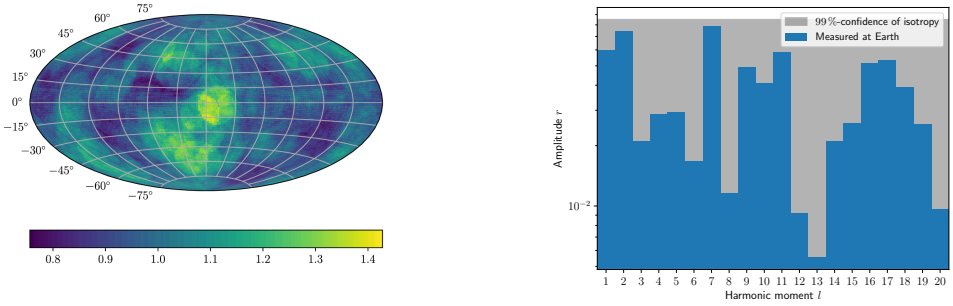

$10^{16} - 10^{18}$ V.

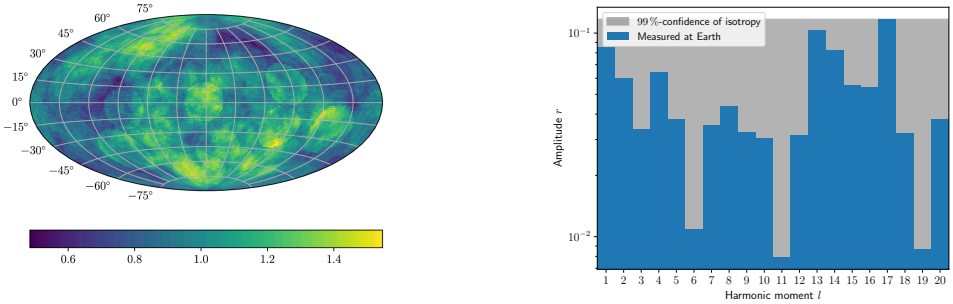

$10^{18} - 10^{18.5}$ V.

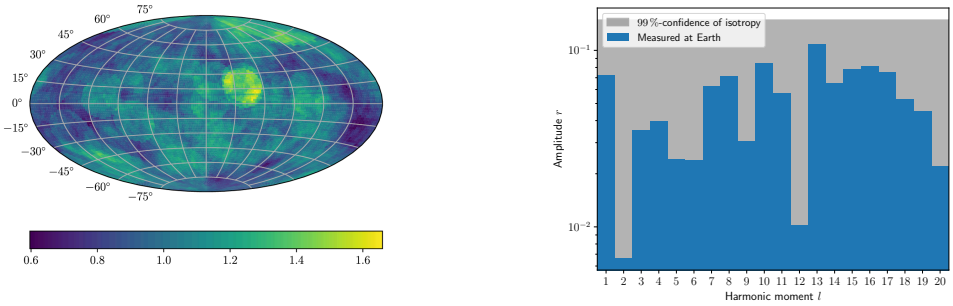

$10^{18.5} - 10^{19}$ V.

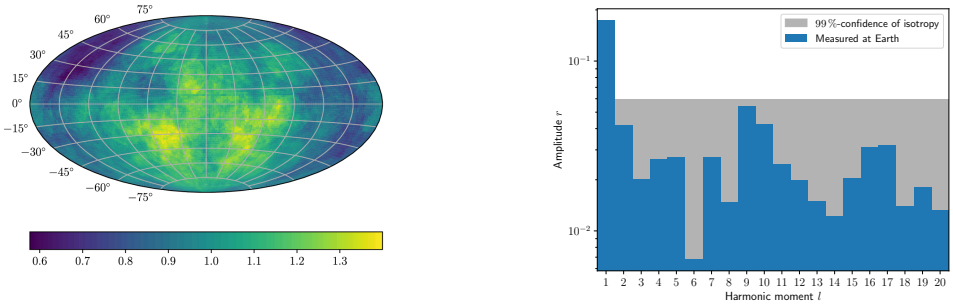

$10^{19} - 10^{20}$ V.

Figure A8: Arrival direction (left) and multipole amplitude (right) distributions of protons injected from a point-source in the direction of Centaurus A with a 5 ° Gaussian smearing and an R^{-1} spectrum in four rigidity windows indicated in each sub-figure.

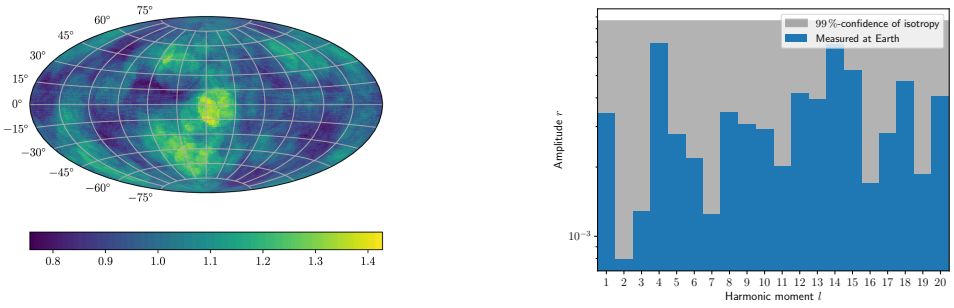

$10^{16} - 10^{18}$ V.

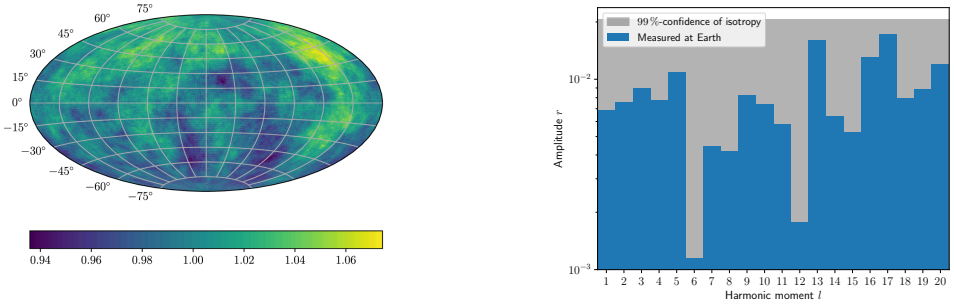

$10^{18} - 10^{18.5}$ V.

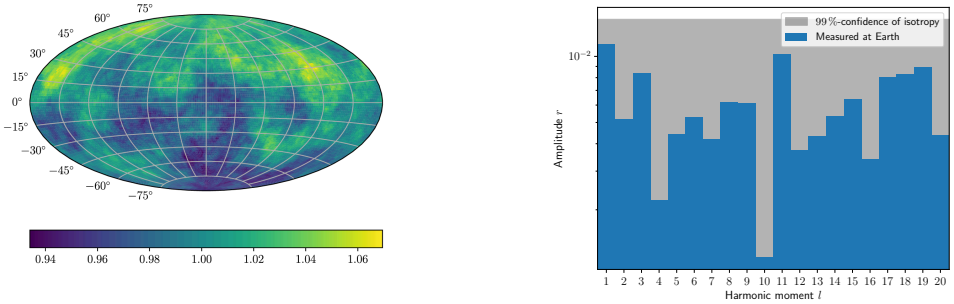

$10^{18.5} - 10^{19}$ V.

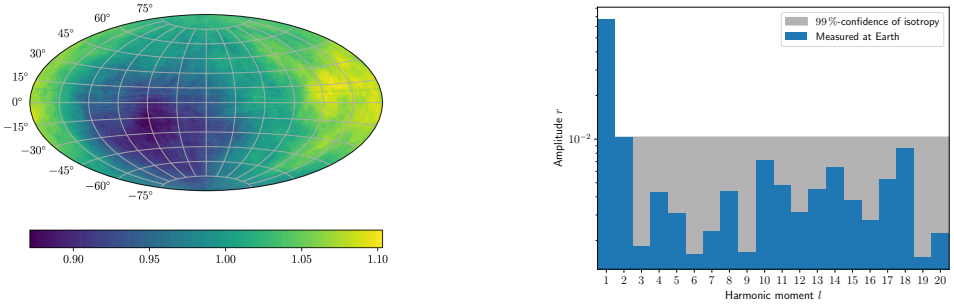

$10^{19} - 10^{20}$ V.

Figure A9: Arrival direction (left) and multipole amplitude (right) distributions of protons injected from a point-source in the direction of maximal Galactic transparency for the rigidity range $10^{16} - 10^{20}$ V (see also figure 5.11) with a 5 ° Gaussian smearing and an R^{-1} spectrum in four rigidity windows indicated in each sub-figure.

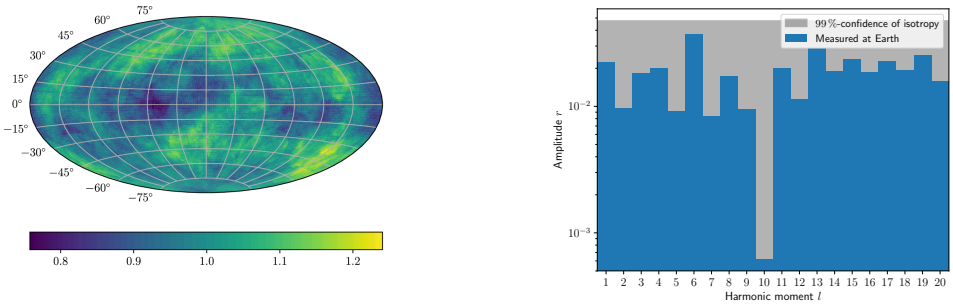

$10^{16} - 10^{18}$ V.

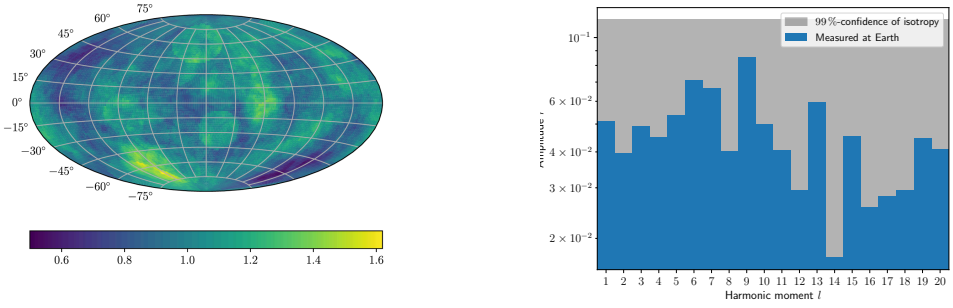

$10^{18} - 10^{18.5}$ V.

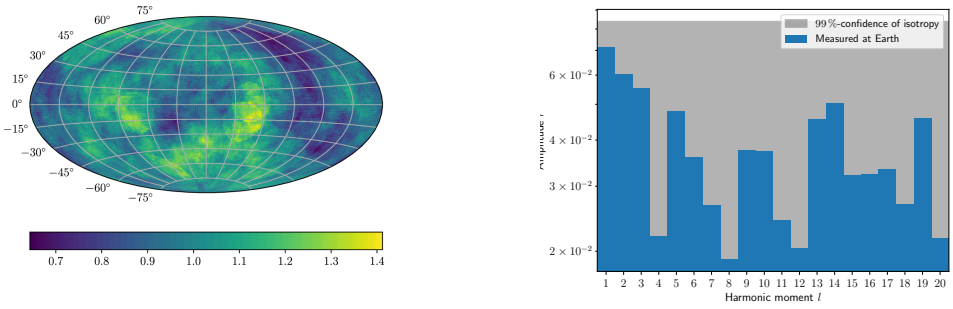

$10^{18.5} - 10^{19}$ V.

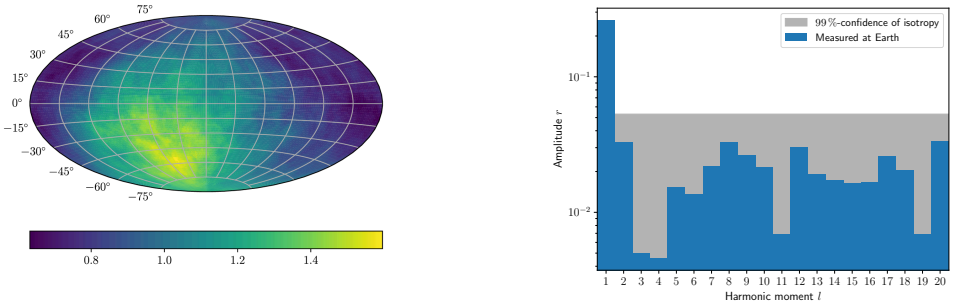

$10^{19} - 10^{20}$ V.

Figure A10: Arrival direction (left) and multipole amplitude (right) distributions of protons injected from a point-source in the direction of the Galactic centre, the direction of minimal Galactic transparency for the rigidity range $10^{16} - 10^{20}$ V (see also figure 5.11), with a 5 ° Gaussian smearing and an R^{-1} spectrum in four rigidity windows indicated in each sub-figure.

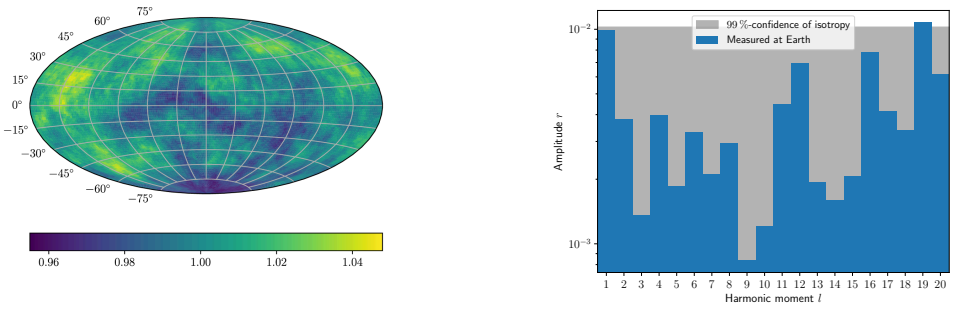

$10^{16} - 10^{18}$ V.

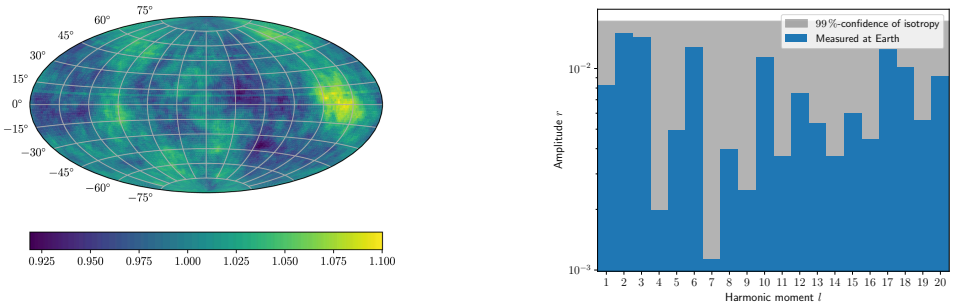

$10^{18} - 10^{18.5}$ V.

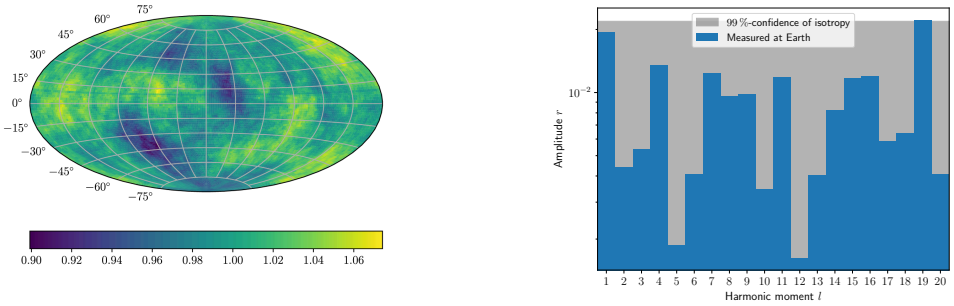

$10^{18.5} - 10^{19}$ V.

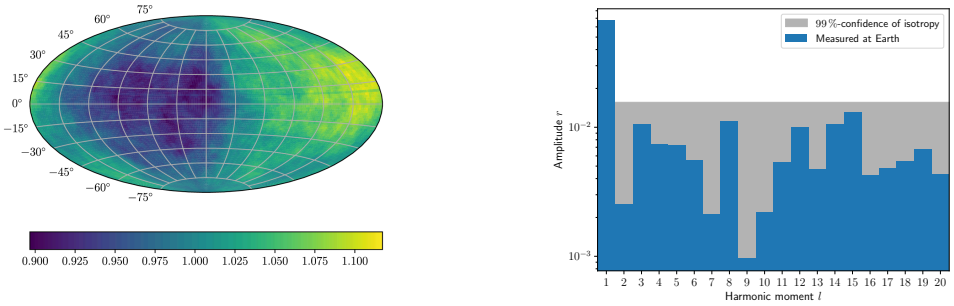

$10^{19} - 10^{20}$ V.

Figure A11: Arrival direction (left) and multipole amplitude (right) distributions of protons injected from a point-source in the direction of the Galactic anti-centre, with a 5 ° Gaussian smearing and an R^{-1} spectrum in four rigidity windows indicated in each sub-figure.

Bibliography

[1] S. Thoudam et al. "Cosmic-ray energy spectrum and composition up to the ankle: the case for a second Galactic component". In: 595, A33 (Oct. 2016), A33. DOI: 10.1051/0004-6361/201628894. arXiv: 1605.03111 [astro-ph.HE].

[2] A. Aab et al. "Features of the Energy Spectrum of Cosmic Rays above 2.5×10^{18} eV Using the Pierre Auger Observatory". In: *Phys. Rev. Lett.* 125.12 (2020), p. 121106. DOI: 10.1103/PhysRevLett.125.121106. arXiv: 2008.06488 [astro-ph.HE].

[3] L. Merten et al. "The Propagation of Cosmic Rays from the Galactic Wind Termination Shock: Back to the Galaxy?" In: *Astrophys. J.* 859.1 (2018), p. 63. DOI: 10.3847/1538-4357/aabfdd. arXiv: 1803.08376 [astro-ph.HE].

[4] J. Becker Tjus and L. Merten. "Closing in on the origin of Galactic cosmic rays using multimessenger information". In: *Phys. Rept.* 872 (2020), pp. 1–98. DOI: 10.1016/j.physrep.2020.05.002. arXiv: 2002.00964 [astro-ph.HE].

[5] S. Van Den Bergh. "Supernova Rates". In: *International Astronomical Union Colloquium* 145 (1996), pp. 1–9. DOI: 10.1017/S0252921100007855.

[6] R. Diehl et al. "Radioactive Al-26 and massive stars in the galaxy". In: *Nature* 439 (2006), pp. 45–47. DOI: 10.1038/nature04364. arXiv: astro-ph/0601015.

[7] E. Fermi. "On the Origin of the Cosmic Radiation". In: *Phys. Rev.* 75 (8 Apr. 1949), pp. 1169–1174. DOI: 10.1103/PhysRev.75.1169. URL: https://link.aps.org/doi/10.1103/PhysRev.75.1169.

[8] W. I. Axford. "The Origins of High-Energy Cosmic Rays". In: 90 (Feb. 1994), p. 937. DOI: 10.1086/191928.

[9] R. Alves Batista et al. "Open Questions in Cosmic-Ray Research at Ultrahigh Energies". In: *Front. Astron. Space Sci.* 6 (2019), p. 23. DOI: 10.3389/fspas.2019.00023. arXiv: 1903.06714 [astro-ph.HE].

[10] K. Greisen. "End to the Cosmic-Ray Spectrum?" In: *Phys. Rev. Lett.* 16 (17 Apr. 1966), pp. 748–750. DOI: 10.1103/PhysRevLett.16.748. URL: https://link.aps.org/doi/10.1103/PhysRevLett.16.748.

[11] G. T. Zatsepin and V. A. Kuzmin. "Upper Limit of the Spectrum of Cosmic Rays". In: *Soviet Journal of Experimental and Theoretical Physics Letters* 4 (Aug. 1966), p. 78.

[12] A. Aab et al. "Combined fit of spectrum and composition data as measured by the Pierre Auger Observatory". In: *JCAP* 04 (2017). [Erratum: JCAP 03, E02 (2018)], p. 038. DOI: 10.1088/1475-7516/2017/04/038. arXiv: 1612.07155 [astro-ph.HE].

[13] A. Aab et al. "The Pierre Auger Observatory and its Upgrade". In: *Science Reviews - from the end of the world* 2020.1 (2020), pp. 8–33. URL: http://scirevfew.net/index.php/sciencereviews/issue/view/4/5.

[14] O. Deligny. "The energy spectrum of ultra-high energy cosmic rays measured at the Pierre Auger Observatory and at the Telescope Array". In: *PoS* ICRC2019 (2020), p. 234. DOI: 10.22323/1.358.0234. arXiv: 2001.08811 [astro-ph.HE].

[15] M. G. Aartsen et al. "Cosmic ray spectrum from 250 TeV to 10 PeV using IceTop". In: *Phys. Rev. D* 102 (2020), p. 122001. DOI: 10.1103/PhysRevD.102.122001. arXiv: 2006.05215 [astro-ph.HE].

[16] K. Andeen and M. Plum. "Latest Cosmic Ray Results from IceTop and IceCube". In: *EPJ Web Conf.* 210 (2019). Ed. by I. Lhenry-Yvon et al., p. 03005. DOI: 10.1051/epjconf/201921003005.

[17] W. D. Apel et al. "The KASCADE-Grande energy spectrum of cosmic rays and the role of hadronic interaction models". In: *Adv. Space Res.* 53 (2014). Ed. by E.-S. Seo and I. V. Moskalenko, pp. 1456–1469. DOI: 10.1016/j.asr.2013.05.008.

[18] R. U. Abbasi et al. "The Cosmic Ray Energy Spectrum between 2 PeV and 2 EeV Observed with the TALE Detector in Monocular Mode". In: *The Astrophysical Journal* 865.1 (Sept. 2018), p. 74. DOI: 10.3847/1538-4357/aada05. URL: https://doi.org/10.3847/1538-4357/aada05.

[19] M. Amenomori et al. "The All-particle spectrum of primary cosmic rays in the wide energy range from 10^{14} eV to 10^{17} eV observed with the Tibet-III air-shower array". In: *Astrophys. J.* 678 (2008), pp. 1165–1179. DOI: 10.1086/529514. arXiv: 0801.1803 [hep-ex].

[20] N. M. Budnev et al. "The primary cosmic-ray energy spectrum measured with the Tunka-133 array". In: *Astropart. Phys.* 117 (2020), p. 102406. DOI: 10.1016/j.astropartphys.2019.102406. arXiv: 2104.03599 [astro-ph.HE].

[21] R. U. Abbasi et al. "First observation of the Greisen-Zatsepin-Kuzmin suppression". In: *Phys. Rev. Lett.* 100 (2008), p. 101101. DOI: 10.1103/PhysRevLett.100.101101. arXiv: astro-ph/0703099.

[22] P. L. Biermann et al. "Supernova explosions of massive stars and cosmic rays". In: *Adv. Space Res.* 62 (2018), pp. 2773–2816. DOI: 10.1016/j.asr.2018.03.028. arXiv: 1803.10752 [astro-ph.HE].

[23] N. Globus, D. Allard, and E. Parizot. "A complete model of the cosmic ray spectrum and composition across the Galactic to extragalactic transition". In: *Phys. Rev. D* 92.2 (2015), p. 021302. DOI: 10.1103/PhysRevD.92.021302. arXiv: 1505.01377 [astro-ph.HE].

[24] M. Unger, G. R. Farrar, and L. A. Anchordoqui. "Origin of the ankle in the ultrahigh energy cosmic ray spectrum, and of the extragalactic protons below it". In: *Phys. Rev. D* 92.12 (2015), p. 123001. DOI: 10.1103/PhysRevD.92.123001. arXiv: 1505.02153 [astro-ph.HE].

[25] S. D'Agostino. "Hertz's Researches on Electromagnetic Waves". In: *Historical Studies in the Physical Sciences* 6 (1975), pp. 261–323. ISSN: 00732672. URL: http://www.jstor.org/stable/27757343.

[26] G. Farmelo. "The Discovery of X-rays". In: *Scientific American* 273.5 (1995), pp. 86–91. ISSN: 00368733, 19467087. URL: http://www.jstor.org/stable/24982088.

[27] P. Radvanyi and J. Villain. "The discovery of radioactivity". In: *Comptes Rendus Physique* 18.9-10 (2017), pp. 544–550. DOI: 10.1016/j.crhy.2017.10.008.

[28] D. Pacini. "Penetrating Radiation at the Surface of and in Water". In: *Nuovo Cim.* 8 (1912), pp. 93–100. DOI: 10.1007/BF02957440. arXiv: 1002.1810 [physics.hist-ph].

[29] V. Hess. "On the Observations of the Penetrating Radiation during Seven Balloon Flights". In: *Physikalische Zeitschrift* 13 (2012), pp. 1084–1091. arXiv: 1808.02927 [physics.hist-ph].

[30] Q. Xu and L. M. Brown. "The early history of cosmic ray research". In: *American Journal of Physics* 55.1 (1987), pp. 23–33. DOI: 10.1119/1.14967. eprint: https://doi.org/10.1119/1.14967. URL: https://doi.org/10.1119/1.14967.

[31] J. Sassi. *Fordham Celebrates Victor Hess, Nobel Laureate*. Accessed: 2021-11-15. Apr. 2011. URL: https://news.fordham.edu/inside-fordham/fordham-celebrates-victor-hess-nobel-laureate/.

[32] R. A. Millikan. "High frequency rays of cosmic origin". In: *Science* 62.1612 (1925), pp. 445–448. ISSN: 0036-8075. DOI: 10.1126/science.62.1612.445. eprint: https://science.sciencemag.org/content/62/1612/445.full.pdf. URL: https://science.sciencemag.org/content/62/1612/445.

[33] R. A. Millikan and G. H. Cameron. "The Origin of the Cosmic Rays". In: *Phys. Rev.* 32 (4 Oct. 1928), pp. 533–557. DOI: 10.1103/PhysRev.32.533. URL: https://link.aps.org/doi/10.1103/PhysRev.32.533.

[34] D. Skobelzyn. "Über eine neue Art sehr schneller β-Strahlen". In: *Zeitschrift für Physik* 54 (9 1929), pp. 686–702. DOI: 10.1007/BF01341600.

[35] W. Bothe and W. Kolhörster. "Das Wesen der Höhenstrahlung". In: *Zeitschrift für Physik* 56 (11-12 1929), pp. 751–777. DOI: 10.1007/BF01340137.

[36] B. Rossi. "Über den Ursprung der durchdringenden Korpuskularstrahlung der Atmosphäre". In: *Zeitschrift für Physik* 68 (1 1931), pp. 64–84. DOI: 10.1007/BF01392728.

[37] M. Walter and A. W. Wolfendale. "Early history of cosmic particle physics". In: *Eur. Phys. J. H* 37 (2012), pp. 323–358. DOI: 10.1140/epjh/e2012-30020-1.

[38] K.-H. Kampert, A. A. Watson, and A. A. Watson. "Extensive Air Showers and Ultra High-Energy Cosmic Rays: A Historical Review". In: *Eur. Phys. J. H* 37 (2012), pp. 359–412. DOI: 10.1140/epjh/e2012-30013-x. arXiv: 1207.4827 [physics.hist-ph].

[39] M. Schein, W. P. Jesse, and E. O. Wollan. "The Nature of the Primary Cosmic Radiation and the Origin of the Mesotron". In: *Phys. Rev.* 59 (7 Apr. 1941), pp. 615–615. DOI: 10.1103/PhysRev.59.615. URL: https://link.aps.org/doi/10.1103/PhysRev.59.615.

[40] S. H. Neddermeyer and C. D. Anderson. "Note on the Nature of Cosmic-Ray Particles". In: *Phys. Rev.* 51 (10 May 1937), pp. 884–886. DOI: 10.1103/PhysRev.51.884. URL: https://link.aps.org/doi/10.1103/PhysRev.51.884.

[41] C. D. Anderson. "The Positive Electron". In: *Phys. Rev.* 43 (6 Mar. 1933), pp. 491–494. DOI: 10.1103/PhysRev.43.491. URL: https://link.aps.org/doi/10.1103/PhysRev.43.491.

[42] P. M. S. Blackett. "The Positive Electron". In: *Nature* 132 (3346 1933), pp. 917–919. DOI: 10.1038/132917a0.

[43] H. Bethe and W. Heitler. "On the Stopping of fast particles and on the creation of positive electrons". In: *Proc. Roy. Soc. Lond. A* 146 (1934), pp. 83–112. DOI: 10.1098/rspa.1934.0140.

[44] H. J. Bhabha, W. Heitler, and N. F. Mott. "The passage of fast electrons and the theory of cosmic showers". In: *Proceedings of the Royal Society of London. Series A - Mathematical and Physical Sciences* 159.898 (1937), pp. 432–458. DOI: 10.1098/rspa.1937.0082. URL: https://royalsocietypublishing.org/doi/abs/10.1098/rspa.1937.0082.

[45] J. F. Carlson and J. R. Oppenheimer. "On Multiplicative Showers". In: *Phys. Rev.* 51 (1937), pp. 220–231. DOI: 10.1103/PhysRev.51.220.

[46] G. Kulikov and G. Khristiansen. "On the size spectrum of extensive air showers". In: *Soviet Phyics JETP* 8 (3 1959), pp. 441–444.

[47] Y. A. Fomin and G. B. Khristiansen. "Size distribution of extensive air showers". In: *Soviet Phyics JETP* 17 (2 1962), pp. 451–231.

[48] A. A. Penzias and R. W. Wilson. "A Measurement of excess antenna temperature at 4080-Mc/s". In: *Astrophys. J.* 142 (1965), pp. 419–421. DOI: 10.1086/148307.

[49] J. Linsley. "Evidence for a primary cosmic-ray particle with energy 10**20-eV". In: *Phys. Rev. Lett.* 10 (1963), pp. 146–148. DOI: 10.1103/PhysRevLett.10.146.

[50] D. M. Edge et al. "The cosmic ray spectrum at energies above 10^{17} eV". In: 6.10 (Oct. 1973), pp. 1612–1634. DOI: 10.1088/0305-4470/6/10/019. URL: https://doi.org/10.1088/0305-4470/6/10/019.

[51] J. Linsley. "Primary cosmic rays of energy 10^{17} to 10^{20} eV, the energy spectrum and arrival directions". In: *International Cosmic Ray Conference*. Vol. 4. International Cosmic Ray Conference. Jan. 1963, p. 77.

[52] M. A. Lawrence, R. J. O. Reid, and A. A. Watson. "The cosmic ray energy spectrum above $4*10^17$ eV as measured by the Haverah Park array". In: *Journal of Physics G: Nuclear and Particle Physics* 17.5 (May 1991), pp. 733–757. DOI: 10.1088/0954-3899/17/5/019. URL: https://doi.org/10.1088/0954-3899/17/5/019.

[53] D. J. Bird et al. "Evidence for correlated changes in the spectrum and composition of cosmic rays at extremely high energies". In: *Phys. Rev. Lett.* 71 (21 Nov. 1993), pp. 3401–3404. DOI: 10.1103/PhysRevLett.71.3401. URL: https://link.aps.org/doi/10.1103/PhysRevLett.71.3401.

[54] N. Hayashida et al. "Observation of a Very Energetic Cosmic Ray Well Beyond the Predicted 2.7 K Cutoff in the Primary Energy Spectrum". In: *Phys. Rev. Lett.* 73 (26 Dec. 1994), pp. 3491–3494. DOI: 10.1103/PhysRevLett.73.3491. URL: https://link.aps.org/doi/10.1103/PhysRevLett.73.3491.

[55] P. M. Mantsch. "The Pierre Auger project". In: *AIP Conference Proceedings* 359.1 (1996), pp. 370–382. DOI: 10.1063/1.49731. eprint: https://aip.scitation.org/doi/pdf/10.1063/1.49731. URL: https://aip.scitation.org/doi/abs/10.1063/1.49731.

[56] K.-H. Kampert. "At the Doorway to UHE Cosmic Ray Astronomy — Recent Results from the Pierre Auger Observatory". In: *AIP Conference Proceedings* 1085.1 (2008), pp. 30–37. DOI: 10.1063/1.3076668. eprint: https://aip.scitation.org/doi/pdf/10.1063/1.3076668. URL: https://aip.scitation.org/doi/abs/10.1063/1.3076668.

[57] T. K. Gaisser, R. Engel, and E. Resconi. *Cosmic Rays and Particle Physics*. 2nd ed. Cambridge University Press, 2016. DOI: 10.1017/CBO9781139192194.

[58] J. Becker Tjus et al. "Gamma-ray emitting supernova remnants as the origin of Galactic cosmic rays?" In: *Astropart. Phys.* 81 (2016), pp. 1–11. DOI: 10.1016/j.astropartphys.2016.03.008. arXiv: 1510.07801 [astro-ph.HE].

[59] A. Aab et al. "Large-scale Cosmic-Ray Anisotropies above 4 EeV Measured by the Pierre Auger Observatory". In: *The Astrophysical Journal* 868.1 (Nov. 2018), p. 4. DOI: 10.3847/1538-4357/aae689. URL: https://doi.org/10.3847%2F1538-4357%2Faae689.

[60] A. Aab et al. "An Indication of Anisotropy in Arrival Directions of Ultra-high-energy Cosmic Rays through Comparison to the Flux Pattern of Extragalactic Gamma-Ray Sources". In: *The Astrophysical Journal* 853.2 (Feb. 2018), p. L29. DOI: 10.3847/2041-8213/aaa66d. URL: https://doi.org/10.3847/2041-8213/aaa66d.

[61] A. Aab et al. "Combined fit of spectrum and composition data as measured by the Pierre Auger Observatory". In: *JCAP* 04 (2017). [Erratum: JCAP 03, E02 (2018)], p. 038. DOI: 10.1088/1475-7516/2017/04/038. arXiv: 1612.07155 [astro-ph.HE].

[62] O. Adriani et al. "PAMELA Measurements of Cosmic-ray Proton and Helium Spectra". In: *Science* 332 (2011), pp. 69–72. DOI: 10.1126/science.1199172. arXiv: 1103.4055 [astro-ph.HE].

[63] O. Adriani et al. "Measurement of Boron and Carbon Fluxes in Cosmic Rays with the PAMELA Experiment". In: *The Astrophysical Journal* 791.2 (July 2014), p. 93. DOI: 10.1088/0004-637x/791/2/93. URL: https://doi.org/10.1088/0004-637x/791/2/93.

[64] M. Aguilar et al. "Precision Measurement of the Helium Flux in Primary Cosmic Rays of Rigidities 1.9 GV to 3 TV with the Alpha Magnetic Spectrometer on the International Space Station". In: *Phys. Rev. Lett.* 115 (21 Nov. 2015), p. 211101. DOI: 10.1103/PhysRevLett.115.211101. URL: https://link.aps.org/doi/10.1103/PhysRevLett.115.211101.

[65] M. Aguilar et al. "Precision Measurement of the Proton Flux in Primary Cosmic Rays from Rigidity 1 GV to 1.8 TV with the Alpha Magnetic Spectrometer on the International Space Station". In: *Phys. Rev. Lett.* 114 (17 Apr. 2015), p. 171103. DOI: 10.1103/PhysRevLett.114.171103. URL: https://link.aps.org/doi/10.1103/PhysRevLett.114.171103.

[66] M. Aguilar et al. "Observation of the Identical Rigidity Dependence of He, C, and O Cosmic Rays at High Rigidities by the Alpha Magnetic Spectrometer on the International Space Station". In: *Phys. Rev. Lett.* 119 (25 Dec. 2017), p. 251101. DOI: 10.1103/PhysRevLett.119.251101. URL: https://link.aps.org/doi/10.1103/PhysRevLett.119.251101.

[67] M. Aguilar et al. "Observation of New Properties of Secondary Cosmic Rays Lithium, Beryllium, and Boron by the Alpha Magnetic Spectrometer on the International Space Station". In: *Phys. Rev. Lett.* 120 (2 Jan. 2018), p. 021101. DOI: 10.1103/PhysRevLett.120.021101. URL: https://link.aps.org/doi/10.1103/PhysRevLett.120.021101.

[68] V. V. Prosin et al. "Results from Tunka-133 (5 years observation) and from the Tunka-HiSCORE prototype". In: *EPJ Web Conf.* 121 (2016). Ed. by P. Piattelli et al., p. 03004. DOI: 10.1051/epjconf/201612103004.

[69] J. C. Arteaga-Velázquez et al. "The KASCADE-Grande observatory and the composition of very high-energy cosmic rays". In: *Journal of Physics: Conference Series* 651 (Nov. 2015), p. 012001. DOI: 10.1088/1742-6596/651/1/012001. URL: https://doi.org/10.1088/1742-6596/651/1/012001.

[70] W. D. Apel et al. "KASCADE-Grande measurements of energy spectra for elemental groups of cosmic rays". In: *Astropart. Phys.* 47 (2013), pp. 54–66. DOI: 10.1016/j.astropartphys.2013.06.004. arXiv: 1306.6283 [astro-ph.HE].

[71] T. Abu-Zayyad et al. "Measurement of the Cosmic-Ray Energy Spectrum and Composition from 10^{17} to $10^{18.3}$ eV Using a Hybrid Technique". In: *The Astrophysical Journal* 557 (Aug. 2001), p. 686. DOI: 10.1086/322240.

[72] S. Knurenko, Z. Petrov, and I. Petrov. "Second Knee on the Spectrum of Cosmic Ray at Energies 10^{17} eV by Long-Term Observations of Small Cherenkov EAS Array". In: *Physics of Atomic Nuclei* 82 (Nov. 2019), pp. 732–738. DOI: 10.1134/S106377881966027X.

[73] A. Aab et al. "Inferences on mass composition and tests of hadronic interactions from 0.3 to 100 EeV using the water-Cherenkov detectors of the Pierre Auger Observatory". In: *Phys. Rev. D* 96 (12 Dec. 2017), p. 122003. DOI: 10.1103/PhysRevD.96.122003. URL: https://link.aps.org/doi/10.1103/PhysRevD.96.122003.

[74] A. Yushkov. "Mass Composition of Cosmic Rays with Energies above $10^{17.2}$ eV from the Hybrid Data of the Pierre Auger Observatory". In: *PoS* ICRC2019 (2020), p. 482. DOI: 10.22323/1.358.0482.

[75] M. Ahlers and P. Mertsch. "Origin of Small-Scale Anisotropies in Galactic Cosmic Rays". In: *Prog. Part. Nucl. Phys.* 94 (2017), pp. 184–216. DOI: 10.1016/j.ppnp.2017.01.004. arXiv: 1612.01873 [astro-ph.HE].

[76] Z. Feng. "Northern sky Galactic Cosmic Ray anisotropy between 10-1000 TeV with the Tibet Air Shower Array". In: *PoS* ICRC2015 (2016), p. 355. DOI: 10.22323/1.236.0355.

[77] R. Abbasi et al. "Observation of an Anisotropy in the Galactic Cosmic Ray arrival direction at 400 TeV with IceCube". In: *Astrophys. J.* 746 (2012), p. 33. DOI: 10.1088/0004-637X/746/1/33. arXiv: 1109.1017 [hep-ex].

[78] M. G. Aartsen et al. "Anisotropy in Cosmic-ray Arrival Directions in the Southern Hemisphere Based on six Years of Data From the Icecube Detector". In: *Astrophys. J.* 826.2 (2016), p. 220. DOI: 10.3847/0004-637X/826/2/220. arXiv: 1603.01227 [astro-ph.HE].

[79] A. Chiavassa et al. "A study of the first harmonic of the large scale anisotropies with the KASCADE-Grande experiment". In: *PoS* ICRC2015 (2016), p. 281. DOI: 10.22323/1.236.0281.

[80] A. Aab et al. "Cosmic-ray anisotropies in right ascension measured by the Pierre Auger Observatory". In: *Astrophys. J.* 891 (2020), p. 142. DOI: 10.3847/1538-4357/ab7236. arXiv: 2002.06172 [astro-ph.HE].

[81] G. Zimbardo et al. "Superdiffusive transport in laboratory and astrophysical plasmas". In: *Journal of Plasma Physics* 81 (Dec. 2015). DOI: 10.1017/S0022377815001117.

[82] P. K. F. Grieder. *Extensive Air Showers. High Energy Phenomena and Astrophysical Aspects - A Tutorial, Reference Manual and Data Book*. 1st ed. Springer-Verlag Berlin Heidelberg, 2010.

[83] R. Engel, D. Heck, and T. Pierog. "Extensive air showers and hadronic interactions at high energy". In: *Ann. Rev. Nucl. Part. Sci.* 61 (2011), pp. 467–489. DOI: 10.1146/annurev.nucl.012809.104544.

[84] P. A. Collaboration. *History*. Accessed: 2021-11-15. 2021. URL: https://www.auger.org/index.php/about-us/history.

[85] R. M. Tennent. "The Haverah Park extensive air shower array". In: *Proceedings of the Physical Society* 92.3 (Nov. 1967), pp. 622–631. DOI: 10.1088/0370-1328/92/3/315. URL: https://doi.org/10.1088/0370-1328/92/3/315.

[86] C. C. H. Jui and the High Resolution Fly's Eye (HiRe Collaboration). "Results from the HiRes Experiment". In: *Journal of Physics: Conference Series* 47 (Oct. 2006), pp. 59–67. DOI: 10.1088/1742-6596/47/1/007. URL: https://doi.org/10.1088/1742-6596/47/1/007.

[87] H. Kawai et al. "Telescope array experiment". In: *Nucl. Phys. B Proc. Suppl.* 175-176 (2008). Ed. by K. S. Cheng et al., pp. 221–226. DOI: 10.1016/j.nuclphysbps.2007.11.002.

[88] T. Gaisser. *Cosmic-Ray Showers Reveal Muon Mystery.* Accessed: 2021-11-15. 2016. URL: https://physics.aps.org/articles/v9/125.

[89] T. P. A. Collaboration. *Pierre Auger Observatory (flickr).* Accessed: 2021-11-15. 2021. URL: https://www.flickr.com/photos/134252569@N07/.

[90] A. Aab et al. "Spectral Calibration of the Fluorescence Telescopes of the Pierre Auger Observatory". In: *Astropart. Phys.* 95 (2017), pp. 44–56. DOI: 10.1016/j.astropartphys.2017.09.001. arXiv: 1709.01537 [astro-ph.IM].

[91] R. U. Abbasi et al. "Study of Ultra-High Energy Cosmic Ray composition using Telescope Arrays Middle Drum detector and surface array in hybrid mode". In: *Astropart. Phys.* 64 (2015), pp. 49–62. DOI: 10.1016/j.astropartphys.2014.11.004. arXiv: 1408.1726 [astro-ph.HE].

[92] V. De Souza, Pierre Auger Collaboration, and Telescope Array Collaboration. "Testing the agreement between the $X_{\max}$ distributions measured by the Pierre Auger and Telescope Array Observatories". In: *35th International Cosmic Ray Conference (ICRC2017).* Vol. 301. International Cosmic Ray Conference. Jan. 2017, p. 522.

[93] M. Haverkorn. "Magnetic Fields in the Milky Way". In: *Magnetic Fields in Diffuse Media.* Ed. by d. G. Lazarian A., D. P. E., and M. C. Astrophysics and Space Science Library. Springer-Verlag Berlin Heidelberg, 2015. DOI: 10.1007/978-3-662-44625-6_17. arXiv: 1406.0283 [astro-ph.GA].

[94] T. R. Jaffe. "Practical Modeling of Large-Scale Galactic Magnetic Fields: Status and Prospects". In: *Galaxies* 7.2 (2019), p. 52. DOI: 10.3390/galaxies7020052. arXiv: 1904.12689 [astro-ph.GA].

[95] T. Steininger et al. "Inferring Galactic magnetic field model parameters using IMAGINE - An Interstellar MAGnetic field INference Engine". In: (Jan. 2018). arXiv: 1801.04341 [astro-ph.GA].

[96] F. Boulanger et al. "IMAGINE: A comprehensive view of the interstellar medium, Galactic magnetic fields and cosmic rays". In: *JCAP* 08 (2018), p. 049. DOI: 10.1088/1475-7516/2018/08/049. arXiv: 1805.02496 [astro-ph.GA].

[97] N. Oppermann et al. "An improved map of the Galactic Faraday sky". In: *Astron. Astrophys.* 542 (2012), A93. DOI: 10.1051/0004-6361/201118526. arXiv: 1111.6186 [astro-ph.GA].

[98] R. Adam et al. "Planck 2015 results. I. Overview of products and scientific results". In: *Astron. Astrophys.* 594 (2016), A1. DOI: 10.1051/0004-6361/201527101. arXiv: 1502.01582 [astro-ph.CO].

[99] X. H. Sun et al. "Radio observational constraints on Galactic 3D-emission models". In: *Astron. Astrophys.* 477 (2008), p. 573. DOI: 10.1051/0004-6361:20078671. arXiv: 0711.1572 [astro-ph].

[100] R. Jansson and G. R. Farrar. "The Galactic Magnetic Field". In: *The Astrophysical Journal* 761.1 (Nov. 2012), p. 11. DOI: 10.1088/2041-8205/761/1/l11. URL: https://doi.org/10.1088/2041-8205/761/1/l11.

[101] T. R. Jaffe et al. "Comparing Polarised Synchrotron and Thermal Dust Emission in the Galactic Plane". In: *Mon. Not. Roy. Astron. Soc.* 431 (2013), p. 683. DOI: 10.1093/mnras/stt200. arXiv: 1302.0143 [astro-ph.GA].

[102] R. Jansson and G. R. Farrar. "A New Model of the Galactic Magnetic Field". In: *The Astrophysical Journal* 757.1 (Aug. 2012), p. 14. DOI: 10.1088/0004-637x/757/1/14. URL: https://doi.org/10.1088/0004-637x/757/1/14.

[103] R. A. Batista et al. "CRPropa 3. a Public Astrophysical Simulation Framework for Propagating Extraterrestrial Ultra-High Energy Particles". In: *Journal of Cosmology and Astroparticle Physics* 05.038 (2016), 13pp. DOI: 10.1088/1475-7516/2016/05/038.

[104] I. Moskalenko et al. "GALPROP Code for Galactic Cosmic Ray Propagation and Associated Photon Emissions". In: *Proceedings of the 32nd International Cosmic Ray Conference, ICRC 2011* 6 (Jan. 2011). DOI: 10.7529/ICRC2011/V06/1194.

[105] M. Unger and G. R. Farrar. "Uncertainties in the Magnetic Field of the Milky Way". In: July 2017. arXiv: 1707.02339 [astro-ph.GA].

[106] K.-H. Kampert et al. "CRPropa 2.0 – a Public Framework for Propagating High Energy Nuclei, Secondary Gamma Rays and Neutrinos". In: *Astropart. Phys.* 42 (2013), pp. 41–51. DOI: 10.1016/j.astropartphys.2012.12.001. arXiv: 1206.3132 [astro-ph.IM].

[107] L. Merten et al. "CRPropa 3.1a low energy extension based on stochastic differential equations". In: *JCAP* 06 (2017), p. 046. DOI: 10.1088/1475-7516/2017/06/046. arXiv: 1704.07484 [astro-ph.IM].

[108] T. C. Developers. *Modules*. Accessed: 2021-11-15. 2020. URL: https://crpropa.github.io/CRPropa3/pages/Simulation-Modules.html#.

[109] T. C. Developers. *Introduction to Python Steering*. Accessed: 2021-11-15. 2020. URL: https://crpropa.github.io/CRPropa3/pages/example_notebooks/basics/basics.v4.html.

[110] D. De Marco, P. Blasi, and T. Stanev. "Numerical propagation of high energy cosmic rays in the Galaxy. I. Technical issues". In: *JCAP* 06 (2007), p. 027. DOI: 10.1088/1475-7516/2007/06/027. arXiv: 0705.1972 [astro-ph].

[111] C. Gardiner. *Stochastic Methods. A Handbook for the Natural and Social Sciences*. 4th ed. Springer-Verlag Berlin Heidelberg, 2009.

[112] M. S. Pshirkov et al. "Deriving the global structure of the Galactic magnetic field from Faraday rotation measures of extragalactic sources". In: *The Astrophysical Journal* 738.2 (Aug. 2011), p. 192. ISSN: 1538-4357. DOI: 10.1088/0004-637x/738/2/192. URL: http://dx.doi.org/10.1088/0004-637X/738/2/192.

[113] P. Terral and K. Ferrière. "Constraints from Faraday rotation on the magnetic field structure in the Galactic halo". In: *Astronomy Astrophysics* 600 (Mar. 2017), A29. ISSN: 1432-0746. DOI: 10.1051/0004-6361/201629572. URL: http://dx.doi.org/10.1051/0004-6361/201629572.

[114] J. R. Cash and A. H. Karp. "A Variable Order Runge-Kutta Method for Initial Value Problems with Rapidly Varying Right-Hand Sides". In: *ACM Trans. Math. Softw.* 16.3 (Sept. 1990), pp. 201–222. ISSN: 0098-3500. DOI: 10.1145/79505.79507. URL: https://doi.org/10.1145/79505.79507.

[115] R. Alves Batista et al. "CRPropa 3.2: a framework for high-energy astroparticle propagation". In: *PoS* ICRC2021 (2021), p. 978. DOI: 10.22323/1.395.0978. arXiv: 2107.01631 [astro-ph.HE].

[116] J. P. Boris and R. A. Shanny. "Relativistic plasma simulation-optimization of a hybrid code". In: *Proceeding of Fourth Conference on Numerical simulation of Plasmas*. Nov. 1970.

[117] T. C. Developers. *Comparison of Propagation Modules (BP - CK)*. Accessed: 2021-11-15. 2020. URL: https://crpropa.github.io/CRPropa3/pages/example_notebooks/propagation_comparison/Propagation_Comparison_CK_BP.html?highlight=cash%20karp#Conservation-of-Momentum.

[118] H.-P. Bretz et al. "PARSEC: A Parametrized Simulation Engine for Ultra-High Energy Cosmic Ray Protons". In: *Astropart. Phys.* 54 (2014), pp. 110–117. DOI: 10.1016/j.astropartphys.2013.12.002. arXiv: 1302.3761 [astro-ph.HE].

[119] N. E. Yanasak et al. "Measurement of the Secondary Radionuclides ^{10}Be, ^{26}Al, ^{36}Cl, ^{54}Mn, and ^{14}C and Implications for the Galactic Cosmic-Ray Age". In: *The Astrophysical Journal* 563.2 (Dec. 2001), pp. 768–792. DOI: 10.1086/323842. URL: https://doi.org/10.1086%2F323842.

[120] P. Lipari. "The lifetime of cosmic rays in the Milky Way". In: (July 2014). arXiv: 1407.5223 [astro-ph.HE].

[121] G. Giacinti, M. Kachelriess, and D. Semikoz. "Explaining the spectra of cosmic ray groups above the knee by escape from the Galaxy". In: *Physical Review D* 90.4 (Aug. 2014). DOI: 10.1103/physrevd.90.041302. URL: https://doi.org/10.1103%2Fphysrevd.90.041302.

[122] G. Giacinti, M. Kachelriess, and D. Semikoz. "Escape model for Galactic cosmic rays and an early extragalactic transition". In: *Physical Review D* 91.8 (Apr. 2015). DOI: 10.1103/physrevd.91.083009. URL: https://doi.org/10.1103%2Fphysrevd.91.083009.

[123] P. Reichherzer et al. “Turbulence-Level Dependence of Cosmic-Ray Parallel Diffusion”. In: *Mon. Not. Roy. Astron. Soc.* 498.4 (2020), pp. 5051–5064. DOI: 10.1093/mnras/staa2533. arXiv: 1910.07528 [astro-ph.HE].

[124] C. D. Stephens, R. W. Brzozowski, and F. Jenko. “On the limitations of gyrokinetics: Magnetic moment conservation”. In: *Physics of Plasmas* 24.10 (2017), p. 102517. DOI: 10.1063/1.4998968. eprint: https://doi.org/10.1063/1.4998968. URL: https://doi.org/10.1063/1.4998968.

[125] K. M. Górski et al. “HEALPix - A Framework for high resolution discretization, and fast analysis of data distributed on the sphere”. In: *Astrophys. J.* 622 (2005), pp. 759–771. DOI: 10.1086/427976. arXiv: astro-ph/0409513.

[126] B. Eichmann and T. Winchen. “Galactic Magnetic Field Bias on Inferences from UHECR Data”. In: *JCAP* 04 (2020), p. 047. DOI: 10.1088/1475-7516/2020/04/047. arXiv: 2001.01530 [astro-ph.HE].

[127] M. C. Beck et al. “New constraints on modelling the random magnetic field of the MW”. In: *JCAP* 05 (2016), p. 056. DOI: 10.1088/1475-7516/2016/05/056. arXiv: 1409.5120 [astro-ph.GA].